UNIVERSITÀ DEGLI STUDI DI FIRENZE

FACOLTÀ DI INGEGNERIA

Dottorato in Ingegneria Industriale e dell'Affidabilità

XXIII Ciclo

Settore Disciplinare (SSD): ING-IND 13

Sezione di *Meccanica Applicata alle Macchine*

TORSIONAL ELECTRO-MECHANICAL INTERACTION IN COMPRESSION TRAINS WITH A SYNCHRONOUS MOTOR FED BY A LOAD COMMUTATED INVERTER

Coordinatore del corso:

Prof. Ing. Mario Tucci

Relatori universitari:

Prof. Ing. Benedetto Allotta

Dott. Ing. Francesco Grasso

Relatori aziendali (GE - Nuovo Pignone):

Dott. Ing. Duccio Fioravanti

Sergio De Franciscis

Candidato:

Ing. Stefano Falomi

a Filippo

Contents

Chapter 1

Introduction

This Ph.D. dissertation describes the results of a research activity sponsored by GE-Nuovo Pignone. This work has been conducted in order to develop numerical models that can be useful both in the design and in the verification phase of compression trains including Variable Speed Drives (VSD), so to minimize risks of operability problems due to torsional vibrations.

Nowadays, in the Oil & Gas industry, VSDs are preferred to Constant Speed Drives because they can improve the efficiency and the range of operability of the process, avoiding the use of complex mechanisms (e.g. guide vanes) or plant recycling and throttling [1] [2] [3]. VSDs are mainly required by Oil & Gas industry for the following application fields: Liquefied Natural Gas Trains, Pipelines, Re-injection, Storage Recompression, Subsea and Process Gas Compression.

The use of VSDs, on the other hand, is not free of concerns, in particular for high shaft-power applications [4]. As a matter of fact it has been observed that VSDs can apply pulsating torques to the shaft line, leading to high amplitude torsional vibrations and shaft line stresses. Typical results of high amplitude torsional vibrations are coupling failures, broken shafts, worn gears, fractured gear teeth and thus undesired plant shutdowns and lacks in operability [5] [6]. Considering the costs related to the shutdown of these plants, several companies, involved in the design of compression trains including VSD, started to analyze the torsional behavior of these machines. However, considering that detailed analyses of this problem have been conducted only in the last 5 years, it is easy to understand that the bibliography is still quite poor: just few papers can been found and most of them are case studies presented by industries at conferences, in which really limited details are given about the modelization of this phenomenon [7] [8]. That is why, during this research activity, we had to decide not only which kind of modelization could be more appropriate for each part of the compression train, but also which aspects or phenomenon had to be included in the model in order to realize a predictive tool.

As a matter of fact, the excitation of torsional vibrations may come from many sources which may or may not be a function of running speed, e.g. aerodynamic excitations, misalignments effects, etc [10]. Moreover, systems including a VSD, unlike those using conventional constant speed electric equipment, show a pulsating torque ripple on the shaft line which is created by the switching nature of the VSD itself. Additionally, as it will be described later in this dissertation, the VSD can respond to already present torsional vibrations by giving pulsating torques that increase the amplitude of these vibrations, leading to an instability of the whole system.

Nowadays, different types of VSDs are used in the Oil & Gas industry. In addition, given the same architecture, different control logics can be implemented. Considering the level of detail that is needed in the modelization, it is not possible to develop a general model that can describe the behavior of all VSDs, but it is necessary to decide which kind of drive has to be addressed in detail for modelling.

During this activity, it has been decided to build a simulation model for a VSD composed by a synchronous machine fed by a load commutated inverter (LCI). The reason for this choice is that this kind of drive represents the standard for the highest power drives (power can be higher than 35 MW), because of its efficiency and reliability, tested on different kind of applications. However some torsional issues have been observed in compression trains that included this kind of drive. That is why this kind of drive has been chosen as the main object of this activity.

The structure of this dissertation reflects the steps followed during the research activity. Chapter 2 describes the development of a model for the description of torsional vibrations of turbomachinery. Chapter 3 includes the basic knowledge needed for the development of an electrical model of a VSD composed by a synchronous machine fed by a load commutated inverter. In chapter 4 details about the integrated electro-mechanical model are given. Chapter 5 describes the validation phase of the simulation tool, in which simulation results are compared to experimental measurements. In Chapter 6 the conclusions derived by the activity are discussed and future steps are described.

Chapter 2

Torsional Analysis of Turbomachinery

In this chapter, the steps that are needed to build a model for the torsional analysis of turbomachinery will be described. Then, the author will summarize the procedure that is usually adopted in industrial environment for the evaluation of the torsional behavior of a system composed by turbomachines and electrical motors. This procedure will be defined as *Open-Loop* approach, because in this procedure, the external forces due to electrical machines are applied to the mechanical system without any feedback to the electrical motor. Then, a brief description of the *Closed-Loop* approach will be given. The last section describes how the torque is measured in order to monitor torsional vibrations and validate the developed torsional models.

2.1 Torsional Vibrations

Torsional vibration is a relative angular motion around the rotating axis between different locations of the shaft line. The time varying twist in the shaft line produces pulsating torques acting both on the shafts of the machines and in the couplings that may be present to connect a machine rotor to another.

An important feature is that if no dedicated instruments are installed in the shaft line, it will be not possible to know if the machines are experiencing this kind of vibrations. As a matter of fact, the angular motion produces no lateral displacement of the shaft line, thus this kind of vibration is not detectable using instruments that measure the vibrations (or accelerations) of the casing of the machines (while this undirect measure is very useful to detect lateral vibrations of machinery). The only exception is given by geared trains: in the gear units, the pulsating torques transmitted by the teeth produce pulsating lateral forces that lead to lateral vibrations; however, also in this case, a dedicated instrumentation is needed in order to measure the amplitude of torsional vibrations, that has to be compared with the strength limits of shafts and couplings.

The absence of lateral motion due to this kind of vibrations affects also the damping acting on them: the fluid film that is present in bearings is not squeezed as in the lateral vibrations, so the only damping effect in bearings is given by the shear friction in the fluid film, leading to a very poor damping. In geared trains, the lateral displacements resulting from torsional vibrations produce a squeezing of the fluid film that gives a slightly higher damping. Bearings are not the only source of damping (other sources are described in the *Torsional Damping* section); however the total torsional damping is usually very low: that is why these vibrations, if undetected, can severely damage the elements of the train shaft line.

2.2 Torsional Analysis of a Compression Train

First of all, it is important to remark that when two or more machines are connected in order to transmit torque between them, the torsional analysis should be conducted with a model that includes all the machines in the shaft line.

This is strongly different from lateral analysis, in which for most cases each machine is analyzed separately from the other machines. The reason is that usually the couplings that connect the machines are *flexible couplings*, which means that they transmit limited axial forces and bending moments on connected shafts: this allows to consider the lateral dynamics of each machine uncoupled with the dynamics of the other machines. However, in particular applications, the machines can be connected by *rigid couplings*, that couple the lateral dynamics of machines' shafts, and that require a model that includes all shafts connected by this kind of coupling.

Considering the torsional vibrations, there is no difference in the modelling of shaft lines with flexible or rigid couplings, because both rigid and flexible couplings transmit pulsating torques resulting from torsional vibrations, resulting in the need to analyze the torsional vibrations of a shaft line as a whole. In the next subsections, all the step that are required to perform the torsional analysis of turbomachinery are summarized.

2.2.1 Lumped Parameters Model

A lumped parameters model is a discretized model in which the shaft line is described as the interconnection of three kind of elements that describe inertia, stiffness and damping of each rotor section.

In particular the model usually includes rigid inertias that are interconnected via massless springs and dampers. In this model dampers can connect subsequent inertias, describing the so-called *internal damping* that is related to the relative motion between rotor sections, or can connect an inertia to the ground, including *external damping* effects,

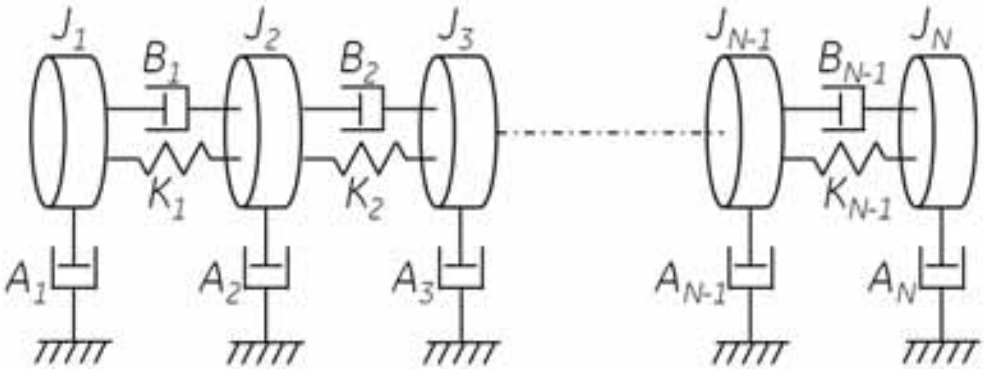

Figure 2.1: Lumped parameters model including damping.

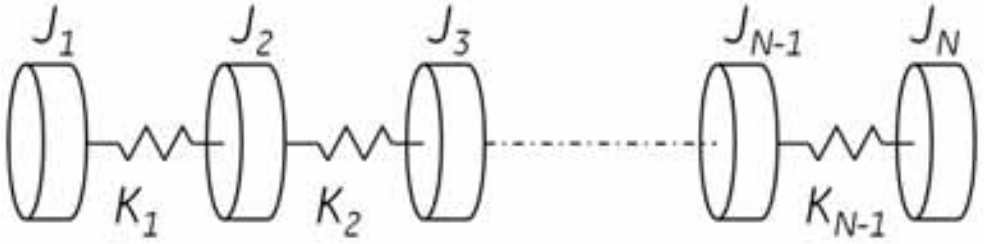

Figure 2.2: Lumped parameters model without damping.

related to the relative motion between the shaft and the casing. An example of a lumped parameter model that includes these elements is reported in Fig. 2.1; J_i is the inertia of the i^{th} disk, K_i is the stiffness of the i^{th} spring, A_i is the damping coefficient of the i^{th} external damper and B_i is the damping coefficient of the i^{th} internal damper.

As it will be further discussed in the *Torsional Damping* section, it is really difficult to describe the physical damping acting on each section: the really weak damping due to each damping effect is almost impossible to be measured, so it is really hard to include a reasonable value for the damping coefficients of each damper included in the model.

However, the really low total damping has a very weak effect on the torsional natural frequencies values and mode shapes, that are the most important features to describe the dynamic behavior of a compression string, as it will be discussed in the *Modal Analysis* section. That is why the model is usually built without including dampers, as in Fig. 2.2.

Standards such as API 684 [13] and API 617 [17] give recommendations about the definition of the lumped parameters model (number of degrees of freedom to be used, calculation of inertia and stiffness of the elements, description of couplings' stiffness, etc...). For the sake of brevity, only a little summary is reported in the present dissertation; the full recommendations can be found in the cited standards.

Figure 2.3 shows an example of discretization: the rotor is composed by 4 parts with a constant diameter. Each part becomes a spring with a torsional stiffness K_i, calculated according to the relation 2.1:

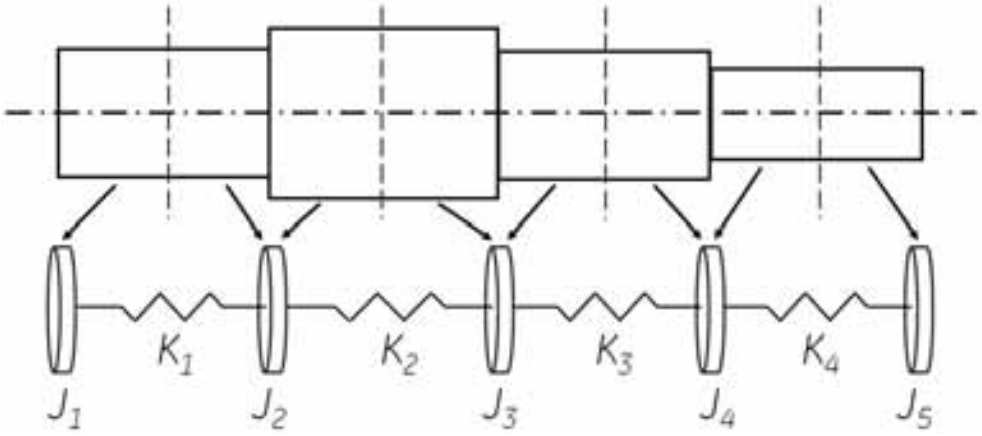

Figure 2.3: Example of a lumped parameters model for a single rotor.

$$K_i = \frac{G\pi(d_{i,ext}^4 - d_{i,int}^4)}{32 l_i} \tag{2.1}$$

where G is the Shear Modulus of the material, $d_{i,ext}$ is the external diameter of the section, $d_{i,int}$ is the internal diameter and l_i is the length of the section.

The four springs connect 5 nodes in which rigid inertias J_i are located; the vertical dashed lines show how the inertia is divided between the nodes. Each part of the shaft with a constant diameter is divided in 2 equal parts: half of the inertia is concentrated in the previous node and half in the subsequent node. The inertia $\hat{J}_i$ of a section with a length l_i is calculated as in 2.2:

$$\hat{J}_i = \frac{\rho\pi(d_{i,ext}^4 - d_{i,int}^4) l_i}{32} \tag{2.2}$$

where ρ is the density of the material. As it has been already specified, half of the calculated inertia is concentrated in the previous node and half in the subsequent node.

The model that has been built is undamped. The equations of motion, including an external torque T_i on each node, are:

$$\begin{aligned}
&J_1\ddot{\theta_1} + K_1(\theta_1 - \theta_2) = T_1 \\
&J_2\ddot{\theta_2} + K_1(\theta_2 - \theta_1) + K_2(\theta_2 - \theta_3) = T_2 \\
&\vdots \\
&J_i\ddot{\theta_i} + K_{i-1}(\theta_i - \theta_{i-1}) + K_i(\theta_i - \theta_{i+1}) = T_i \\
&\vdots \\
&J_N\ddot{\theta_N} + K_{N-1}(\theta_N - \theta_{N-1}) = T_N
\end{aligned} \tag{2.3}$$

where N is number of nodes of the model and θ_i is the angular position of the i^{th} node.

These equations can be grouped in matrix form as in 2.4:

$$[J]\ddot{\vec{\theta}} + [K]\vec{\theta} = \vec{T} \tag{2.4}$$

where $[J]$ is the $[N \times N]$ diagonal Inertia Matrix and $[K]$ is the $[N \times N]$ tridiagonal Stiffness Matrix; $\vec{T}$ is the $[N \times 1]$ vector of external torques and $\vec{\theta}$ contains the N degrees of freedom of the system, that are the rotations of each section about the shaft axis.

2.2.2 Undamped Modal Analysis: Natural Frequencies and Mode Shapes

The modal analysis is a mathematical process that allows to calculate the torsional natural frequencies (TNFs, that are the eigenvalues) and the mode shapes (eigenvectors), starting from the matrix form of the equations of motion as in Eq. 2.4. Firstly, the mathematical process is described; secondly the importance of the output quantities will be discussed.

2.2.2.1 Eigenanalysis

The modal analysis is conducted considering the equations of motions 2.4 without including external forces or torques. The equations of motions become, in matrix form:

$$[J]\ddot{\vec{\theta}} + [K]\vec{\theta} = \vec{0}. \tag{2.5}$$

The solutions of this system of differential equations can be written as:

$$\vec{\theta} = \vec{\theta_0} e^{\lambda t} \tag{2.6}$$

Considering the form of the Inertia and Stiffness matrices, that are both symmetrical and positive definite, it is possible to affirm that the solutions are imaginary pairs such as $\pm j\omega_i$, where j represents the imaginary unit. This means that the trial solution, and its derivatives, can be written in the form:

$$\begin{aligned} \vec{\theta} &= \vec{\theta_0} e^{j\omega t} \\ \dot{\vec{\theta}} &= j\omega \vec{\theta_0} e^{j\omega t} \\ \ddot{\vec{\theta}} &= -\omega^2 \vec{\theta_0} e^{j\omega t} \end{aligned} \tag{2.7}$$

By inserting the trial solution and its derivatives (Eq. 2.7) in 2.5, we obtain:

$$(-\omega^2[J] + [K])\vec{\theta_0} e^{j\omega t} = \vec{0} \tag{2.8}$$

It is possible to multiply both the sides of the equations for the inverse of the Inertia matrix J, thus obtaining:

$$[J]^{-1}(-\omega^2[J]+[K])\vec{\theta_0}e^{j\omega t} = [J]^{-1}\vec{0} \Longrightarrow (-\omega^2[I]+[J]^{-1}[K])\vec{\theta_0}e^{j\omega t} = \vec{0} \tag{2.9}$$

Considering that the exponential term $e^{j\omega t}$ is always non-zero, in order to obtain non-zero solutions for θ_0 for the Eq. 2.9 for θ_0 it is possible to write:

$$det(-\omega^2[I]+[J]^{-1}[K]) = 0 \tag{2.10}$$

The process of calculating a solution for the equations of motion (without including external forces) leads to a problem that corresponds to the calculation of the eigenvalues of the matrix $[J]^{-1}[K]$. As a matter of fact the eigenanalysis of a matrix A is conducted by solving the equation $det(-\lambda[I]+[A]) = 0$. So it is possible to note that the equation 2.10 corresponds to the eigenanalysis of the matrix $[J]^{-1}[K]$.

Physically, the rotor is underconstrained: the rotor can rotate freely because there is no constraint to connect the rotor to the ground. This is reflected in the eigenanalysis by obtaining a zero eigenvalue which is related to the rigid body motion of rotation. The square roots of the non-zero eigenvalues are the torsional natural pulsations ω_i, in rad/s. The torsional natural frequencies (TNFs) are obtained by dividing the pulsations by 2π . The eigenvector associated with each TNF represents the mode shape for the rotor corresponding to that TNF.

2.2.2.2 Torsional Natural Frequencies and Mode Shapes

The values of torsional natural frequencies (TNFs) strongly affect the response of a system to external forces. Figure 2.4 shows an example of a frequency response function in which the input is the frequency of a constant amplitude pulsating torque and the output is the amplitude of vibration. Considering that the amplitude is in logarithmic scale (Magnitude in dB = $20log_{10}$(Magnitude)) it is possible to argue that the response of the system is really sharp around the 4 natural frequencies, whose values are indicated by the dashed vertical lines. The mechanical system acts on the input pulsating torques as a filter: if the input frequency is far from a TNF, then the amplitude of resulting vibrations is usually not worrying, while if the input frequency is close to a TNF, the excitation will result in high amplitude vibrations, that can damage machines' elements.

That is why it is very important to calculate the TNFs: in order to avoid torsional vibration problems it is very important not to have, in operating conditions, pulsating torques which frequency corresponds to a TNF. As a matter of fact, in operating conditions, the excitation of torsional vibrations may come from many sources which may or may not be a function of running speed, e.g. aerodynamic excitations, misalignments

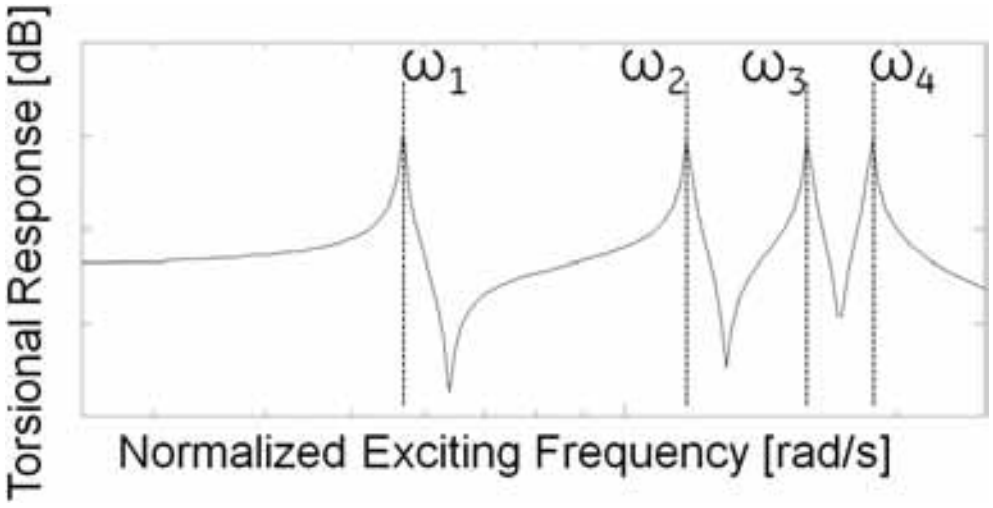

Figure 2.4: Example of Frequency Response Function

effects, etc [10]. It is very important to avoid that within the operating speed range there is a coincidence between an excitation and a torsional natural frequency; if this happens, and no viable countermeasure allows to avoid this coincidence, more investigation is needed to understand if the system can sustain this excitation without a reduction in reliability. These aspects will be detailed in the *Campbell Diagram* and in the *Forced Response* sections.

Figure 2.5 shows an example of a mode shape for a string composed by 5 machines (M1 to M5) connected by 4 couplings (C1 to C4). There is no scale in the amplitude of deformation, because only the deformed shape of the shaft line is important; the absolute amplitude of the deformations in the mode shape depends only on the normalization process adopted in the calculation.

When a compression string is excited by a pulsating torque which frequency equals a TNF, the shaft line assumes a deformed shape during the vibration that reflects the mode shape corresponding to the excited TNF. This vibration will be superimposed to the rigid rotation of the rotor.

The 4 crosses indicate where the mode shape amplitude is zero. These points are called the nodal points; the j^{th} modal shape (excluding the first rigid body mode) has always j nodal points. So we can conclude that Fig. 2.5 represents the 4^{th} flexible mode of the string. Nodal points are very important because, in these points, the amplitude of the mode shape is zero, while the derivative of the mode shape has a local extreme (maximum or minimum).

In torsional vibrations, the mode shape represents the twist angle for each section. This means that if the rotor is vibrating at a certain TNF, the twist angle for each section will oscillate according to the excited mode shape. So in nodal points, no oscillation is visible, and these points are fixed in a reference frame that follows the rigid rotation of the

rotor. However, in this kind of problem, the derivative of the deformed shaft line is related to the torque acting on that section: this can be deducted by comparing the expression of the derivative of the twist angle in Eq. 2.11 with the torque T_i acting on the i^{th} section in Eq. 2.12:

$$\frac{\mathrm{d}\theta}{\mathrm{d}z} \approx \frac{\theta_{i+1} - \theta_i}{l_i} \tag{2.11}$$

$$T_i = K_i(\theta_{i+1} - \theta_i) \tag{2.12}$$

where z is the abscissa along the shaft axis, l_i is the length of the section, K_i is the torsional stiffness of the section as in Eq. 2.1 and θ_i is the angular position of the i^{th} section.

Note that Eq. 2.12 is valid to describe the torque acting on a finite length shaft section if no inertia is present in the section; this corresponds to the lumped parameters model with massless springs, where inertia is concentrated only in nodes.

As we can see, the torque can be expressed as a multiple of the derivative of the twist angle by combining the Eqs. 2.11 and 2.12:

$$T_i = K_i l_i \frac{\mathrm{d}\theta}{\mathrm{d}z} \tag{2.13}$$

Defining the polar moment of inertia $J_{p,i} = \frac{\pi(d_{i,ext}^4 - d_{i,int}^4)}{32}$, and introducing in 2.13 the definition of K_i as in Eq. 2.1 it is possible to write:

$$T_i \approx G J_{p,i} \frac{\mathrm{d}\theta}{\mathrm{d}z} \tag{2.14}$$

This demonstrates that the torque acting on a certain section is a multiple of the derivative of the twist angle. This means that in nodal points, in which the absolute value of the derivative has a local maximum, there will be also a local maximum for the transmitted torque. Considering that the usual methods applied to measure the torsional vibrations are based on a measure of the transmitted torque (more details in the section *Torque Measurement*) it is possible to state that nodal points are the best points where to identify torsional vibrations. However, these are also critical points, because the high amplitude pulsating torques can create fatigue problems to the shaft; that is why the fatigue calculations usually involve these points.

The mode shape gives also an information about the excitability of a mode: if we consider the mode shape in Fig. 2.5 it is possible to observe that the amplitude of the deformed shape is almost zero in the first machine. If this machine starts to apply a pulsating torque at the corresponding TNF, it will not be able to excite the modal shape, thus resulting in very low amplitude vibrations. On the contrary, if the 4^{th} and 5^{th} machines

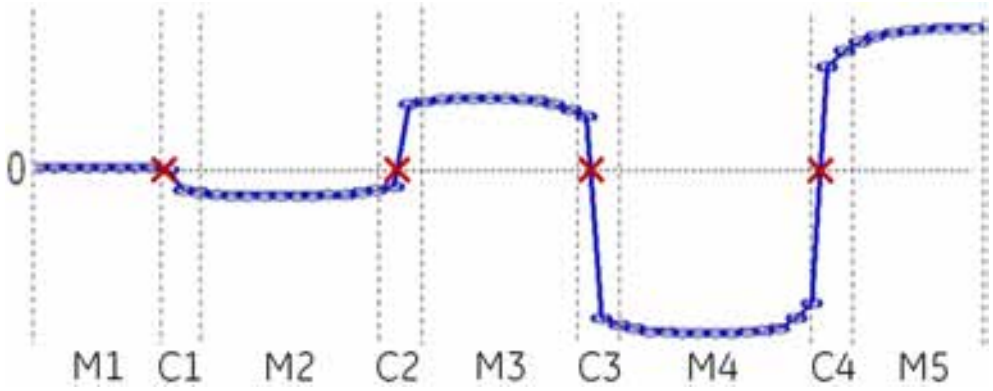

Figure 2.5: Example of Torsional Mode Shape

apply a pulsating torque at that TNF, they will lead to vibrations with a significantly higher amplitude, because the mode shape reveals that they are more likely to excite these modes.

That is why, when analyzing the pulsating torques that can be given by an electrical motor, those modes in which the amplitude in the electrical machine is almost zero are usually disregarded.

Mode shapes can also give information about the points in which a change in inertia or stiffness can be more effective. Sometimes it happens that the designer has to change the value of a TNF to avoid the excitation of the mode shape in operating conditions; for instance the value of a TNF can be raised by raising the stiffness in the system or by reducing the inertia. However the effectiveness of a change depends also on the mode shape: the TNF value is more sensitive to a change in stiffness where the derivative of the amplitude is higher (e.g. nodal points), while it is more sensitive to a change on the inertia where the amplitude of the mode is higher.

2.2.3 Campbell Diagram

The Campbell Diagram [16] is an useful tool to analyze to occurrence of coincidences between TNFs and excitation frequencies within the operating range.

Fig. 2.6 shows a sample diagram for a compression string with a VSD. Scales are omitted for intellectual property reasons. Only the frequency for the network that feeds the VSD is shown in the horizontal axis.

The operating range is drawn in Fig. 2.6 using vertical dashed lines. The acronyms MOS and MCS refer to the Minimum Operating Speed (MOS) and Maximum Continuous Speed (MCS); the internal range, between MOS and MCS, is the actual operating range of the train. API specifications state that TNFs of the full train should be at least 10% above or 10% below any possible excitation frequency within the specified operating speed

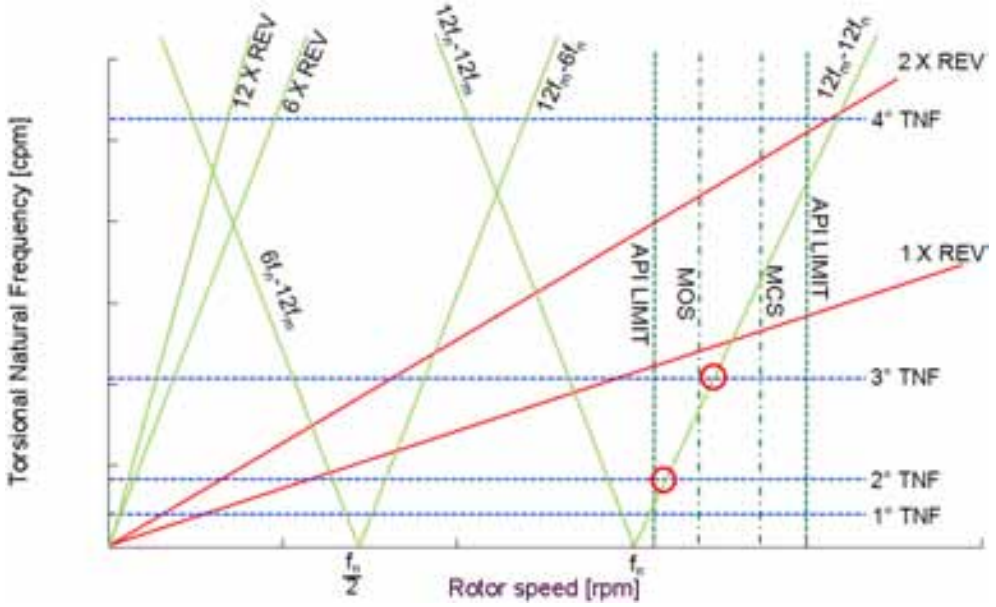

Figure 2.6: Example of Campbell Diagram

range.

Dashed horizontal lines represent the TNFs of the train. These are horizontal lines because TNFs do not depend on the rotor speed. This is due to the fact that neither stiffness nor inertia of any single element depend on rotor speed, so the eigenvalues of the matrix $[J]^{-1}[K]$ do not depend on rotor speed.

Then the lines that represent the excitations are drawn: first the excitations due to the process are represented: the 1 X REV line represents synchronous excitations usually related to unbalances in machines or couplings, while the 2 X REV line describes the excitations mainly related to the misalignments between machine shafts. Note that the 1 X REV line corresponds to a line in which the frequency is equal to the revolution speed of the shaft (that means that if the same unit would be used for the quantities for x and y axes, then this line would be the bisecting line of the first quadrant).

In addition, when an electrical machine is installed in the compression train, it is necessary to include the excitations sources related to the drive: the exciting frequencies usually depend on the architecture of the drive (network frequency, fixed or variable speed, architecture of the converter, etc.). In the sample figure, some of the excitations due to a variable speed frequency drive with a six-pulse LCI architecture are drawn (see [24] for further details).

These components are the so called harmonics (that are components which frequency is a multiple of the line frequency f_n or of the motor frequency f_m, such as the 6 X REV and 12 X REV components) and interharmonics (the components which frequency is a linear combination of both line frequency and motor frequency, such as $12f_m - 12f_n, 12f_n -$

$12f_m, 12f_m - 6f_n, 6f_n - 12f_m$). The presence of these components is due to the switching in thyristor bridges both in network side and motor side. Note that the coefficients in the inter-harmonics depend on the architecture of the Variable Speed Drive, so they are valid only for a particular architecture. In the next chapter, the reason for the presence of these components will be detailed.

Considering that the network frequency f_n is fixed and the motor frequency (Hz) corresponds to the motor speed divided by 60 (and multiplied with the number of pole pairs in the electrical motor), it is possible to draw all these excitations in the Campbell diagram.

The red circles are added to highlight the intersections between excitations and TNFs. In this case it happens that the $12f_m - 12f_n$ cross the 2^{nd} and the 3^{rd} TNFs inside the range specified by the API standards: the crossing with the 3^{rd} TNF is within the operating range, while the crossing with the 2^{nd} TNF is outside the operating range, but inside the API margins.

When a crossing in the API range happens the designer has to perform a fatigue calculation to understand if these excitation torques can lead to a fatigue damage (see the *Forced Response* section for further details). Cyclic stresses due to these excitations are compared with design limits that are a fraction of the endurance limits of materials.

If this condition is not satisfied, the mechanical design is modified in order to increase the fatigue strength or to move the intersection outside the API range.

Usually, the couplings between machines are the more flexible components in the train; that is why the values of the lower TNFs are mainly function of couplings' stiffness and machines inertia [16]. Moreover, if a compression string has N couplings, the first N torsional frequencies will be significantly lower than the the higher ones: for the lower TNFs the deformation will be concentrated in couplings, and the shafts will be undeformed, while in the highest TNFs shafts are deformed and the stiffness of the deformed shafts has a relevant influence on the value of the TNFs.

2.2.4 Forced Response

The Forced Response analysis allows to evaluate the behavior of the train when external torques are applied. The equations of motions can be written in the form 2.4, but an additional term is needed to describe the damping of the mechanical system. The equations, including the damping matrix $[C]$ are, in matrix form:

$$[J]\ddot{\vec{\theta}} + [C]\dot{\vec{\theta}} + [K]\vec{\theta} = \vec{T} \tag{2.15}$$

It would not make sense, in this application, to analyze the response to an external torque without including a damping term, because the absence of damping leads to an

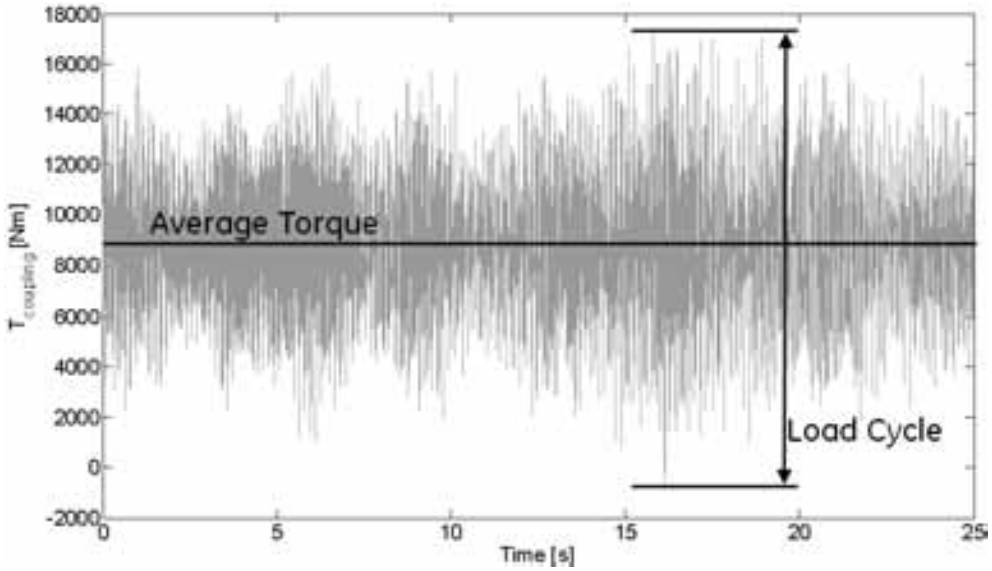

Figure 2.7: Evaluation of Load-Cycle for Fatigue Life Assessment

infinite amplitude of vibrations when a TNF is excited [22]. However it is very difficult to build the damping matrix $[C]$, because quantitative evaluation of damping due to physical phenomena that occur in torsional dynamics is still today a really challenging activity [10]. The model for the torsional damping mechanisms that has been implemented in the dynamic model developed by the author, is detailed in the *Reduced Modal Model* and *Torsional Damping* sections.

The forced response allows to calculate the torque acting on couplings and shafts over time; Fig. 2.7 shows an example of calculated torque for a certain coupling. Note that couplings are usually the most flexible and weak points on the shaft line, thus they usually are the most critical sections for assessing the fatigue life of the system.

Fatigue is a physical phenomenon, that has been firstly observed in history in railway wheelsets, for which a mechanical component fails after a time varying loading, even if the load never reaches the yield strength of the resistant section of the component [20]. The analysis of the behavior of steel, has demonstrated that it is possible to design components in order to avoid this phenomenon, thus having an infinite life of components under time varying loading, by using during the design phase the modified Goodman Diagram. However, it is very important to remark that fatigue is a stochastic phenomenon: it is not possible to have the 100% confidence on the fatigue strength, because the aforementioned Goodman Diagram is drawn for each steel alloy considering the resistance of 99% (or sometimes 95%) of the material samples. However, the use of appropriate safety factors in the design phase, quality checks on the manufactured couplings and periodical on-site inspections allow to avoid these problems on compression strings.

In order to understand how to design shafts and couplings using the Goodman Dia-

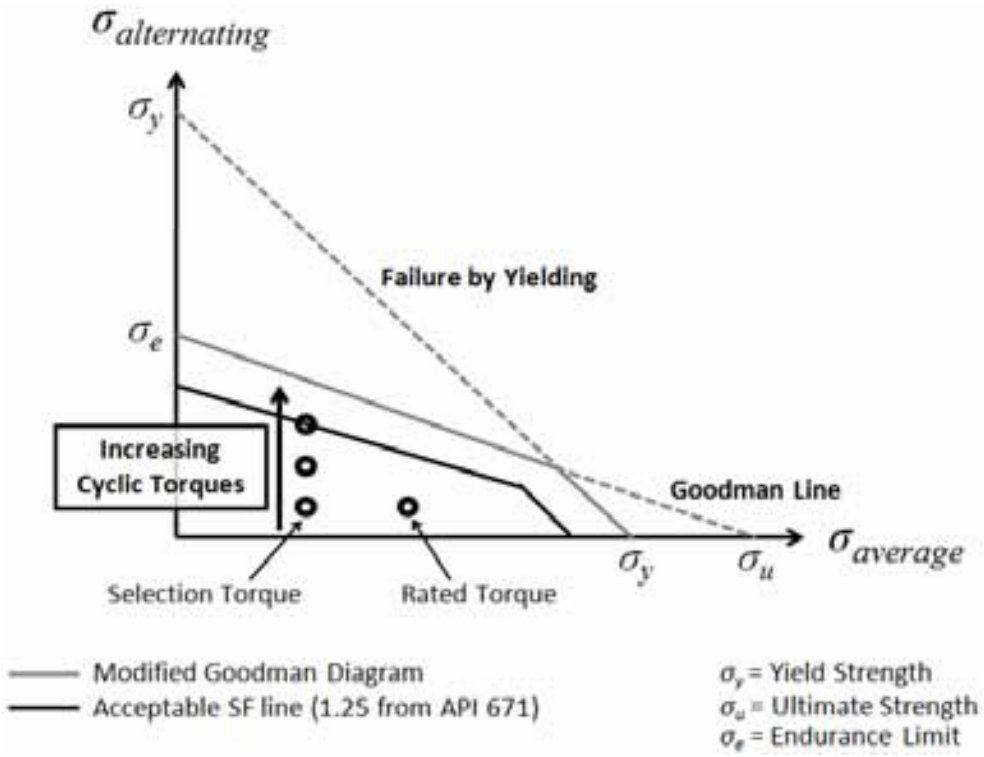

Figure 2.8: Example of Goodman Diagram

gram, it is firstly necessary to analyze Fig. 2.7, that shows the calculated torque acting on a certain coupling. In this condition, the average torque transmitted by the coupling is constant (about 9000 Nm), but external excitations lead to a time varying torque, that can be considered the sum of the average value with a number of harmonic components.

If the load condition acting on the coupling gives a torque that is the sum of an average value with only one sinusoid, the amplitude of that sinusoid would be defined as the alternating torque; however the frequency content of the torque is usually made of several components, thus a conservative assumption to define the amplitude of the alternating torque is to consider the maximum and minimum torque acting on the element, and suppose that their difference is the peak-to-peak amplitude of the Load Cycle. This is equivalent to suppose that these points are the maximum and minimum value of a constant amplitude sinusoidal torque acting on the coupling.

Then, the stress acting on the resistant section of the coupling due to the average torque is defined as the average stress $\sigma_{average}$; the stress on the coupling section due to the 0-peak amplitude of the Load Cycle is defined as the alternating stress $\sigma_{alternating}$.

The modified Goodman Diagram allows to verify both the static strength of the element, that means if the material reaches the Yield stress σ_y after loading, and the fatigue strength of the element. An example of a Goodman Diagram is depicted in Fig. 2.8.

The horizontal axis represents the average stress, while the vertical axis represents the

alternating stress.

In order to construct this diagram for a particular component, firstly two lines are drawn: the line which represents the failure by yielding (static strength), and the one which is related to fatigue failure, that is defined in figure *Goodman Line*.

The value σ_e is the endurance limit for the material, which is the value of cyclic stress (with no average stress applied) for which the material will have an infinite life. The value σ_u represents the ultimate stress, that is the stress due to a static load that leads to reach the ultimate tensile strength of the component.

The two lines define a safe area that is represented as a solid gray line, that identifies the so-called Modified Goodman Diagram. The peculiarity of this line is that if the combination of average and alternating stress is inside the area defined by this line, both the static and fatigue strength of the component are verified.

The API standard for couplings [12] requires the application of a minimum fatigue factor of safety equal to 1.25 when designing a coupling; this means that the safe area is reduced to that defined by the solid black line.

The Rated Torque operating point, depicted by a black circle, is the value of the torque capability of the coupling given by the manufacturer, that considers a combination of speed, angular misalignment and axial displacement that lead to a certain alternating stress. The manufacturer assures that this point is inside the region bordered by the solid black line.

The Selection Torque is a value which is related by a certain service factor to the actual maximum continuous torque that the coupling will have to transmit on the particular compression string where it will be integrated. The coupling is chosen in order to have a selection torque lower than rating torque, because this assures that this operating point will be inside the safe area.

When alternating stress becomes higher, because of alternating torques higher than the predicted values, the operating point in modified Goodman Diagram moves in vertical direction, as it is shown by the vertical arrow. If this point reaches or passes the solid black line, fatigue life of the coupling has to be analyzed in higher detail.

Thus it is very important to have a reliable estimation of cyclic stresses, because it allows to have an higher confidence in the design of couplings. The electromechanical model that is the object of the present activity has to be able to satisfactorily predict the time varying torques on couplings, in order to help the designer in the fatigue life assessment of the shaft line.

2.2.5 Reduced Modal Model

The aim of the activity, as stated before, is to build an electro-mechanical model that is able to describe the torsional dynamics of a compression train connected to an electrical motor. In order to reduce the computational burden (considering that the dynamics of the electrical system are very complex), it has been decided to describe the mechanical system using a reduced model, instead of the whole lumped parameter model. In the reduced modal model, the physical state variables are replaced by the amplitude of vibration for each torsional mode. Using the mass normalized modal matrix [22] and assuming that the damping matrix $[C]$ is a linear combination of inertia and stiffness matrix, the equation of motion for the i^{th} torsional mode will be expressed as:

$$\ddot{q}_i + 2\xi_i\omega_i\dot{q}_i + \omega_i^2 q_i = \vec{\phi_i} \cdot \vec{T} \tag{2.16}$$

where q_i is the modal amplitude of vibration, ω_i and $\vec{\phi_i}$ are the pulsation in rad/s and mode shape for the i^{th} vibration mode calculated from undamped analysis; ξ_i is the modal damping and $\vec{T}$ is the vector of external forces. The equation 2.16 is often written, in torsional analysis, in the form:

$$\ddot{q}_i + \frac{\omega_i}{AF_i}\dot{q}_i + \omega_i^2 s = \vec{\phi_i} \cdot \vec{T} \tag{2.17}$$

where AF_i is the modal Amplification Factor. Note that the modal Amplification Factor is related to the modal damping ξ according to the relation $AF = \frac{1}{2\xi\sqrt{1-\xi^2}}$, so it seems that the relation 2.17 is not correct. However, because of the low damping ξ that is present in torsional vibrations, it is possible to approximate $AF \approx \frac{1}{2\xi}$, thus explaining the relation between 2.17 and 2.16.

Note that in this approach, the designer does not need to include in the model the physical damping that is present in each section, but he has to estimate the modal damping for the modes that he decided to include in the modal model, thus simplifying the evaluation of the damping in the shaft line.

An important issue is the selection of the number of modes that shall be included in the reduced model. Different criteria are applied, considering:

1. the Variable Speed Drive bandwidth;
2. if a mode can be excited by the electrical motor, according to the mode shape;
3. if a mode involves machine rotors' deformation (the damping associated to these modes is usually higher than those without rotors' deformation [16]);
4. the maximum continuous speed (usually modes which frequency is higher than MCS are disregarded).

2.2.5.1 Physical Coordinates and Modal Coordinates

It is important to understand how it is possible to shift from physical coordinates (that means the angular position of each section of the shaft line, and their derivatives) to the modal coordinates (amplitude of vibration of each mode and their derivatives). Let us suppose that the equations of motion are written as in Eq. 2.4, for a system with N inertias, that correspond to N degrees of freedom, without including damping terms. The damping will be included in a later stage, in order to have an easier description of the damping phenomena. The eigenanalysis of these N equations, allows to calculate the N Torsional Natural Frequencies and mode shapes of the undamped system. The mathematical process that will be applied is based on the assumption that the TNFs and mode shapes does not change when a damping term is added: this is true only if the damping matrix is a linear combination of the inertia and stiffness matrix. However in torsional analysis it is approximately true even if the damping matrix does not meet this requirement, because the damping is always very low thus it does not affect TNFs and mode shapes.

It is very important to recall that a mode shape is not a unique vector: by multiplying the mode shape for a scalar, the result is still the same mode shape (remember that mode shapes are eigenvectors calculated from an eigenanalysis). A common way to present to mode shapes is to multiply each mode shape for a constant in order to have an unitary norm of the mode shape. In our application, the best way to scale the mode shapes is to define the so called mass-normalized mode shapes, obtained by dividing each mode shape for a scalar that is the square root of the mode shape's modal mass. The calculation process is as follows: if $\vec{\psi_i}$ is the i^{th} mode shape calculated by a mathematical routine, the modal mass m_i for that mode is evaluated as follows:

$$m_i = \vec{\psi_i}^T [J] \vec{\psi_i} \tag{2.18}$$

Then the i^{th} mass normalized mode shape is calculated as:

$$\vec{\phi_i} = \frac{\vec{\psi_i}}{\sqrt{m_i}} \tag{2.19}$$

The so-called normal modal matrix $[\Phi_N]$ is constructed by joining in a matrix the mass normalized mode shapes of all the N modes calculated for the system:

$$[\Phi_N] = [\vec{\phi_1} \quad \vec{\phi_2} \quad \dots \quad \vec{\phi_N}] \tag{2.20}$$

The normal modal matrix is very important because it is the basis of the coordinate transformation from physical coordinates to modal coordinates and vice-versa. If both members of Eq. 2.4 are premultiplied by the transpose of the modal matrix, the undamped

equations of motion become:

$$[\Phi_N]^T[J]\ddot{\vec{\theta}} + [\Phi_N]^T[K]\vec{\theta} = [\Phi_N]^T\vec{T} \tag{2.21}$$

The Eq. 2.21 can be manipulated by inserting the identity $[I]$ matrix before the inertia and stiffness matrices:

$$[\Phi_N]^T[J][I]\ddot{\vec{\theta}} + [\Phi_N]^T[K][I]\vec{\theta} = [\Phi_N]^T\vec{T} \tag{2.22}$$

Then the identity matrix can be substituted with the term $[\Phi_N][\Phi_N]^{-1}$:

$$[\Phi_N]^T[J][\Phi_N][\Phi_N]^{-1}\ddot{\vec{\theta}} + [\Phi_N]^T[K][\Phi_N][\Phi_N]^{-1}\vec{\theta} = [\Phi_N]^T\vec{T} \tag{2.23}$$

The vector of modal coordinates $\vec{q}_N$ is then defined as the product $[\Phi_N]^{-1}\vec{\theta}$; thus it is possible to write $\ddot{\vec{q}}_N = [\Phi_N]^{-1}\ddot{\vec{\theta}}$; the equation 2.23 is re-written in the form:

$$[\Phi_N]^T[J][\Phi_N]\ddot{\vec{q}}_N + [\Phi_N]^T[K][\Phi_N]\vec{q}_N = [\Phi_N]^T\vec{T} \tag{2.24}$$

The normal modal matrix has the following properties:

$$[\Phi_N]^T[J][\Phi_N] = [I] \tag{2.25}$$

$$[\Phi_N]^T[K][\Phi_N] = \begin{bmatrix} \omega_1^2 & & & \\ & \omega_2^2 & & \\ & & \ddots & \\ & & & \omega_N^2 \end{bmatrix} \tag{2.26}$$

Considering the Eqs. 2.25 and 2.26, the equation of motion for the i^{th} mode can be written as:

$$\ddot{q}_i + \omega_i^2 q_i = \vec{\phi_i^T} \cdot \vec{T} \tag{2.27}$$

where $\vec{\phi_i^T}$ is the transpose of the i^{th} mode shape.

Note that this coordinate transformation decouples the equations of motion: in the i^{th} equation there is only the unknown function $q_i(t)$ and its derivatives, thus the equation of motion for each degree of freedom can be solved separately. The modal coordinate q_i corresponds to the amplitude of vibration for the i^{th} mode.

It is possible to note that Eq. 2.27 corresponds to the Eq. 2.16, without the damping term. Now it is possible to include the damping term, choosing an appropriate value for the modal damping ξ_i for each mode.

By the inversion of the definition of modal coordinates $\vec{q} = [\Phi]^{-1}\vec{\theta}$, once the solution of equations of motions is calculated over time, it is possible to calculate the angular position of all sections:

$$\vec{\theta} = [\Phi_N]\vec{q}_N \tag{2.28}$$

Eq. 2.28 shows that the amplitude of vibrations for each section in the shaft line is calculated by the sum of N terms that are the mode shapes of the analyzed system; each mode shape is weighted by the amplitude of vibration for that mode shape q_i.

The calculations that has been detailed in the preceding equations, simply operate a change in coordinates, but does not reduce the number N of degrees of freedom in the model.

The reduction is performed by disregarding the effect of a certain number of modes, according to the criteria mentioned in the first part of this section, and suppose that the angular positions of all sections can be approximated with the expression:

$$\vec{\theta} \approx [\Phi]\vec{q} \tag{2.29}$$

where $[\Phi]$ is a reduced normal modal matrix that includes only the mode shapes that are retained in the reduced model, and $\vec{q}$ is a vector that contains only the amplitude of vibration of the selected modes. If the number of the selected modes is n, that is less than N, the reduced normal modal matrix is a rectangular $[N \times n]$ matrix, and the reduced vector of modal coordinates $\vec{q}$ has n elements.

2.2.6 Torsional Damping

The estimation of damping is very important, during the verification of the design, for two reasons: first the damping value affects the amplitude of the response to a constant amplitude harmonic excitation; secondly it affects the fatigue life estimation by affecting the rate of decay of torsional oscillations when external excitations are removed, because it determines the number of cycles needed to damp the oscillation.

Torsional damping for turbomachinery is generally very low in comparison to that of lateral vibrations because significant damping for the latter is obtained through radial motion in journal bearings that compresses the oil film, while in torsional vibrations there is no radial motion associated to the vibration (except for geared trains). As a matter of fact, when a torsional vibration is present in a geared train, the harmonic torques are associated to harmonic radial forces that lead to lateral vibrations in the gear unit. This lateral motion squeezes the oil in journal bearings, thus introducing a damping effect that increases the total damping in the compression train.

Modal damping values have been measured on several turbine-generator designs in service, as it can be found in [16], confirming in each case extremely low modal damping. Modal damping values (either estimated or measured) can be used directly in vibration analysis by writing the forced response equations in modal form.

It has been observed in turbine-generator tests at power stations or industrial plants that the modal damping values are functions of the turbine-generator power output and the transmission network configuration. The modal damping values increase substantially as the load on the turbine is increased, presumably because the aerodynamic damping forces on the turbine blades increase as the machine power output (and steam flow rates) rise. In addition, it has been found that there is a high degree of variability between the damping values measured on different turbine-generator designs. The modal damping values have also been observed to be slightly different on nominally identical turbine-generator designs under the same operating conditions, probably because of manufacturing tolerances.

The modal damping that is measured by observing the mechanical response (filtered into separate modal components) is made up of several constituents. Most of the individual damping mechanisms are complex and are not accurately predictable at the design stage. Some of the most significant mechanisms that introduce internal damping (see the *Lumped Parameters Model* section) are:

- shaft material hysteresis, particularly at high levels of oscillating strain;
- energy dissipation from coupling slippage (friction) during high torsional oscillations.

The most important mechanisms that produce external damping are:

- fluid forces on turbine and compressor blades and seals and windage forces on rotor surfaces;
- generator, shaft-driven alternator or motor electrical damping;
- electrical damping or undamping from the transmission network and control equipment.

Other mechanisms are listed and detailed in [10], that describes also relations to predict the damping related to some of these phenomena. However, if the designer estimates modal damping using these relations, he will probably underestimate the real damping (and no criterion has been defined to predict how much the damping is underestimated). That is why the designer usually assigns a modal damping value basing on experience, that means measurements on similar machines, or considering that by adopting that value in previous analyses he was able to correctly predict the stress values present in the machine's elements.

2.2.7 Open-Loop Analysis

In a torsional open-loop analysis, the electrical machine is considered as a device that applies a torque (constant or time varying) that is independent on the behavior of the mechanical system (e.g. instantaneous speed of electric machine's shaft). The torque of the electrical machine is evaluated using analytical relations or electrical models in which the speed of the electrical machine is assumed (constant or following a ramp, depending on the analysis). The open loop torsional analysis, that is performed during the design of the compression string, follows these steps:

- a lumped parameters model is developed, starting from the design of shafts and couplings;
- torsional natural frequencies and mode shapes are calculated with a modal analysis of the equations of motion for the developed model;
- Campbell diagram is drawn and intersections between exciting torques and torsional natural frequencies are identified;
- for all the intersections in the operative range ($\pm 10\%$, according to API standards), a forced responce analysis is conducted, in order to assess the fatigue life of the string; damping is usually estimated according to the designer past experience;
- transient and fault torque verifications (e.g. pulsating torques due to short circuits in electrical machines)

During the last phase, the amplitude of pulsating torques due to mechanical excitations are estimated considering API standards, while the amplitude of excitations due to electrical machines are suggested by the electrical machine's vendor that relies on analytical estimations or open-loop electrical models of the electric machine (that means a model in which the speed of the electrical machine is fixed and constant, so it is not the feedback of the mechanical dynamic model).

2.2.8 Closed-Loop Analysis and ElectroMechanical Interaction

The *Closed-Loop* model that has been developed to analyze the dynamics of this compression train is detailed in chapter 4; however it is very important to understand what *Closed-Loop* means in this kind of analysis, in order to understand the value added with this approach.

In the *Closed-Loop* system, the torque input given by the electrical machine is calculated using an electrical machine's model in which the speed of the electrical machine is

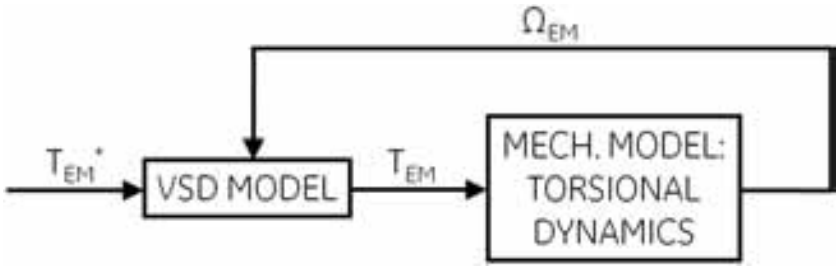

Figure 2.9: Closed-Loop System

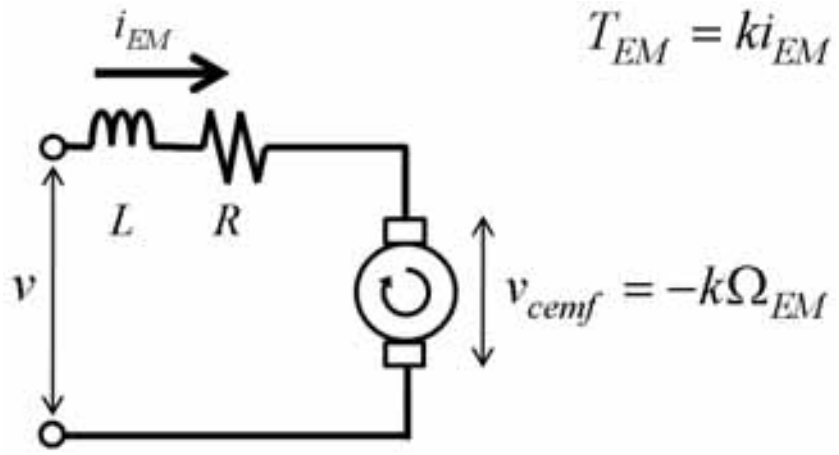

Figure 2.10: DC Motor Model

not assumed, but is the output of the mechanical dynamic model, as in Fig. 2.9. In this example, the electric motor is torque controlled: a reference torque signal T^*_{EM} is given to the electrical machine; the machine applies a torque T_{EM} to the mechanical system. The output speed in the electrical motor section Ω_{EM} is then an input of the electrical machine model.

This closed loop model allows to understand how the electrical motor reacts to the speed oscillations due to torsional vibrations. For instance, let us consider a DC electrical motor: this machine is far different from the system that we are going to analyze in the present dissertation, but its simple model clearly shows the meaning of electro-mechanical interaction. The machine model is shown in Fig. 2.10.

The machine counter-electromotive force v_{cemf} is proportional to the rotor speed: an harmonic component on rotor speed, due to a torsional vibration at a certain frequency, creates an harmonic component on v_{cemf} at the same frequency. If the applied voltage v is constant, then the current i_{EM} entering the machine will also have an harmonic component at that frequency; considering that the torque given by the electrical motor is proportional to the current i_{EM}, it is possible to conclude that the motor will apply a torque that contains an harmonic component at the same frequency of the torsional vibration. If the motor torque component is in counterphase with speed oscillations, then

the motor will damp the speed oscillations, while if the harmonic torque is in phase with speed oscillation, then the electrical motor will excite torsional vibrations, thus resulting in possible high-amplitude vibrations or even instability, that means that the electrical machine will continue to excite torsional vibrations of the compression string until the motor is stopped. This would be the most adverse form of electromechanical interaction.

Now that the meaning of Closed-Loop electromechanical interaction has been described, it is possible to conclude that torsional issues related to an electrical machine can be related to two different mechanisms:

- pulsating torques due to harmonics and interharmonics, which frequency depends only on the VSD architecture;
- pulsating torques due to electromechanical interaction, that means torque components that represent the response of the drive to torsional oscillations, which frequency depends both on the mechanical system and the electrical drive and can be predicted only using a detailed closed-loop model.

It's important to remark that even if the frequency of harmonics and interharmonics does not depend on the presence of torsional vibrations, the effect of these components in terms of torsional vibrations can be described only considering the closed-loop electromechanical interaction. That is why a closed-loop model is fundamental to have a proper evaluation of torsional dynamics of compression strings with VSDs.

2.3 Torque Measurements

The most common way to measure the torque acting on a shaft is to measure the strain on the surface of the shaft using strain-gauge rosettes. For torsional vibration measurements, two strain-gauge rosettes are commonly placed 180° apart on the shaft; then their signals are summed. This cancels out bending strains in the shaft because simple bending strains in a shaft would ideally be of equal magnitude but opposite in sign for the two rosettes. Details about this method can be found in [16]

Strain-gauge telemetry systems are very useful in tests but often lack the durability required for long-term monitoring of a machine. That is why other systems have been developed, that are designed to last for the whole machine life. Most of these systems are based on phase shift methods that require a measure of relative angular position of two sections. The torque is calculated by measuring the angular position θ_1 and θ_2 of two adjacent sections, and by multiplying their difference with the torsional stiffness K_t of the element which connects them, according to relation 2.30:

$$T = K_t \cdot (\theta_2 - \theta_1) = K_t \cdot \Delta\theta \tag{2.30}$$

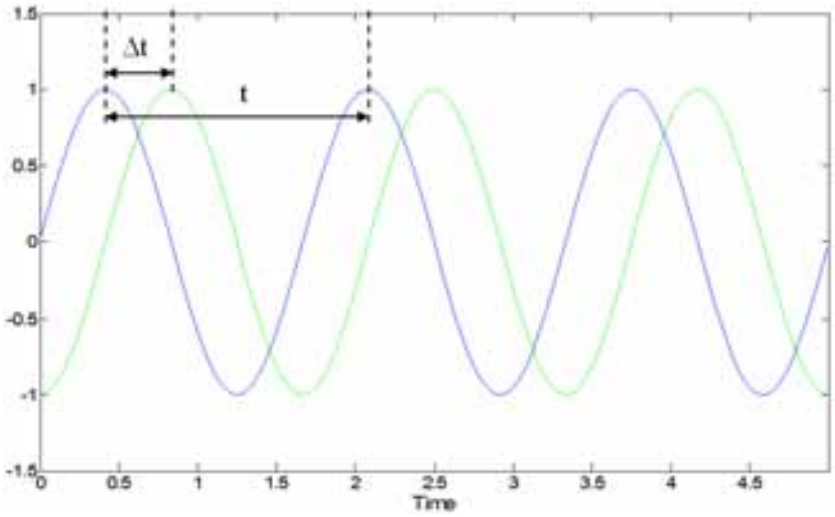

Figure 2.11: Phase Shift

where T is the torque acting on the shaft and $\Delta\theta$ is the difference in angular position, that is calculated according to Eq. 2.31:

$$\Delta\theta[rad] = 2\pi\frac{\Delta t}{t} \tag{2.31}$$

where t is the period of the signal that is measured to detect the angular position of the sections and Δt is the time delay between the signals for two adjacent sections.

For instance, a commercial torquemeter that has been developed to be installed in site for the whole life of the compression train, measures the phase shift between sections using a toothed wheel with a circumferential pickup that is installed on each of the two sections, as in figure 2.12; the rotation of the toothed wheel will generate a sinusoidal signal, and the phase of this signal will give the information about the current angular position of the section.

Other phase shift methods use the angular position of bolts in bolted flanges to measure the phase shift between adjacent sections. What is important to recognize, is that phase shift methods usually have poor performances at low rotational speed, because of the long time that elapses between two subsequent passages of the devices (teeth, bolts, etc.) that identify the angular position.

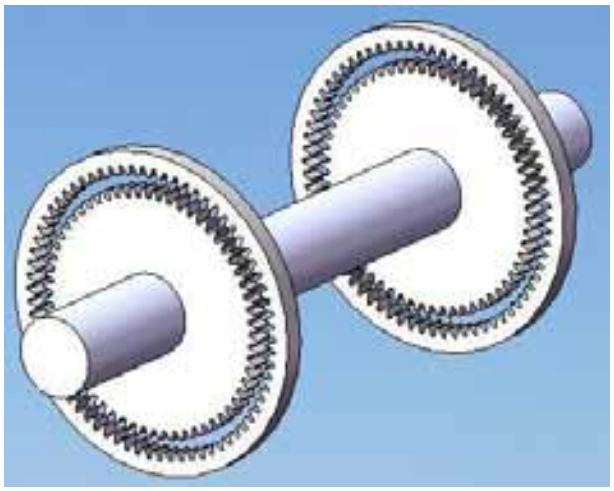

Figure 2.12: Toothed wheels with circumferential pickup

Chapter 3

Power Electronics and Variable Speed Drives

This chapter gives a brief introduction on the application of VSDs in LNG compression trains. Then it focuses on a particular kind of drive, the LCI converter with synchronous motor, because it has been the main object of the present research activity.

3.1 Variable Speed Drives

In the Oil & Gas Industry, applications of Variable Speed Drives are continuously increasing. The main features that make them attractive for Oil & Gas trains are adjustability over a wide range of rotational speeds and fast response in terms of the output torque of the motor. In addition, VSDs are very reliable and do not require special maintenance. The VSD can be the only motor in the compression string, or can be an additional source of power in trains with a gas turbine. In gas turbine applications, VSDs can be installed as starter motors or helper motors or both: the starter operates only during the starting procedure while the helper gives extra motor torque when, in particular environmental conditions, the gas turbine is not able to give the total power needed to move the compressors or in case of reduced gas turbine output (e.g., reduced availability of fuel gas, emission control, etc.). This solution is commonly adopted in Liquefied Natural Gas (LNG) plants. VSDs are also widely used in motor compressor trains (compressor driven by electric motor only) when a wide compression train operating speed range is required (speed range of 30-105%), in order to operate the compressors with an high efficiency even with low flow mass rate.

The scheme in Fig. 3.1 shows an high level diagram of a VSD, with an AC electrical motor. The drive is fed by a converter composed of a rectifier (AC/DC) and an inverter (DC/AC). This double conversion allows to feed the electrical motor at the frequency

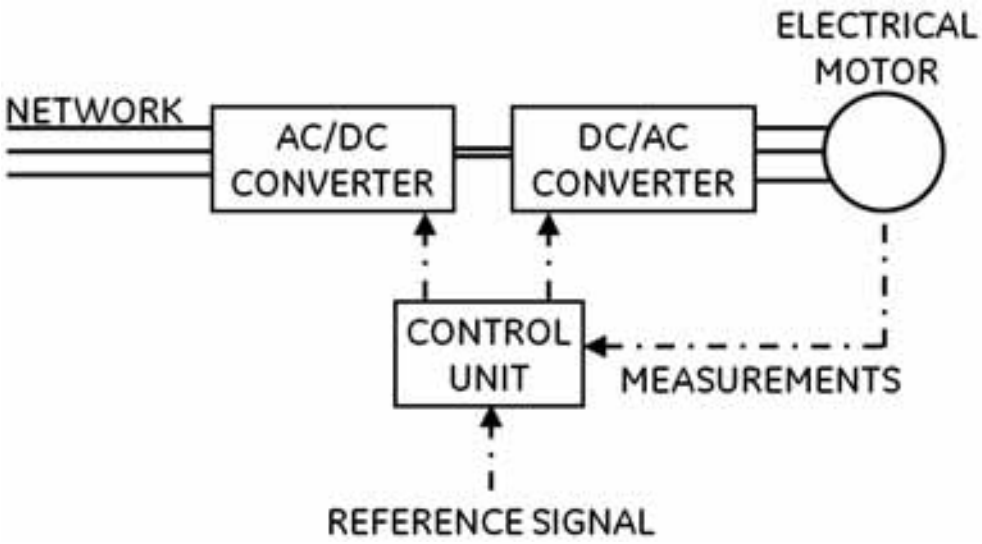

Figure 3.1: High Level Diagram of a Variable Speed Drive with AC motor.

that is needed by the process (feeding frequency should match rotating frequency of the motor, considering the number of pole pairs and the slip in asynchronous motors), that differs from the network frequency. Rectifier and inverter are power electronic converters that are composed by switches; these can be diodes, thyristors or transistors depending on the drive architecture. A control unit send input signals to the switches, considering a reference signal, that can be the target speed of the train, or the target motor torque, and comparing the reference signal with measurements on the machine.

The electrical motor is usually a 6-phase motor, because of the high power required; both synchronous and asynchronous motors are used in Oil & Gas applications.

Details about converters can be found in [24]. The dissertation will focus only on the converters that have been analyzed during the Ph. D. research activity.

3.2 Power Electronic Converters

Power electronic converters are a family of electrical circuits which convert electrical energy from one level of voltage or current or frequency to another using electronic switches. The process of switching the electronic devices in a power electronic converter from ON state to OFF and vice-versa is called modulation. Several modulation strategies have been developed for the different possible layouts, to optimize the circuit operation for the target criteria most appropriate for the particular application. Parameters such as switching frequency, distortion, losses, harmonic generation, and speed of response are the typical issues which must be considered when developing modulation strategies for a particular architecture.

According to their basic functions, converters can be divided into the following groups:

- Rectifiers (AC/DC converters)
- Inverters (DC/AC converters)
- AC/AC converters
- DC/DC converters

In a Variable Speed Drive with AC motor, the AC power from the network (usually at 50 or 60 Hz) is converted in AC power at the operating frequency of the electrical motor. This conversion, as it is shown in Fig. 3.1, is performed by firstly using a rectifier (AC/DC conversion) and then an inverter (DC/AC converter). The rectifier can be designed to create in output a DC voltage, or a DC current. That is why inverters are usually divided in two classes: *voltage fed* and *current fed* inverters. A *voltage fed* inverter receives in input a DC voltage, and converts it in an AC voltage in output. Usually, in this scheme, IGBTs and power MOSFETs are used. Conversely, a *current fed* inverter receives in input a DC current, and feeds the motor with an AC current. In these drives generally GTOs and thyristors are used.

The Load Commutated Inverter, that is the architecture of the drive that has been analyzed in the research activity, is a *current fed* inverter, in which rectifier and inverter are thyristors bridges. That is why, in the next paragraphs, the operation of thyristors will be firstly detailed; then the application of thyristors to rectifier and inverter bridges in LCI converters will be described. In order to make easier the understanding of the operation of a thyristor bridge, the diode bridge will be firstly detailed.

The full theoretical background of three phase rectifiers and inverters is beyond the scope of the present dissertation. The reader can find full theory of three phase bridges in [24].

3.2.1 Diodes

The bipolar diode is made of a crystal wafer with an n-type and a p-type layer. When a negative voltage is applied between the anode (p-layer) and the cathode (n-layer), the p-n junction is depleted of charge carriers. The diode blocks, that means that no current flows in it, and the voltage is supported by the p-n junction. If the voltage source is reversed, so that a positive voltage is applied between the anode and cathode, the diode conducts. As long as current is supplied by the external circuit, the diode continues to conduct. If the current falls to zero and the voltage between anode and cathode becomes negative, the valve blocks.

Figure 3.2: Scheme of a diode.

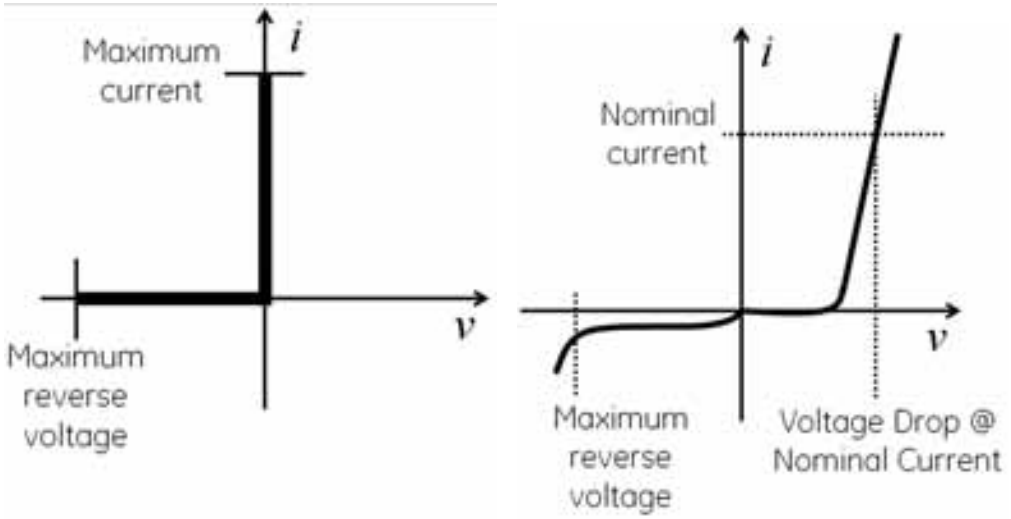

(a) Ideal characteristic **(b)** Real characteristic

Figure 3.3: Ideal and Real characteristic of a diode.

3.2.2 Thyristors

Thyristors (also known as SCRs, that means Silicon Controlled Rectifiers) are semiconductor valves made with four layers P-N-P-N, with three P-N junctions, as in Fig. 3.4.

When a negative voltage is applied between the anode and cathode, the two outer junctions are depleted of charge carriers and support the voltage, so that no current can flow. With a positive voltage applied between the anode and cathode, the middle junction is depleted and prevents the flow of current. This blocking effect, however, can be removed by a triggering pulse applied to the inner p-layer (the gate). The triggering pulse causes a sudden flooding of the whole crystal with charge carriers and the thyristor switches from the blocking to the conducting state. In the conducting state, as in the negative blocking state, the thyristor behaves exactly like a diode. The thyristor ideal and real characteristic are shown in Fig. 3.5.

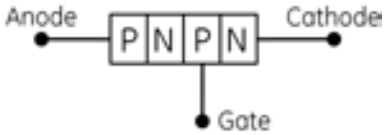

Figure 3.4: Scheme of a thyristor.

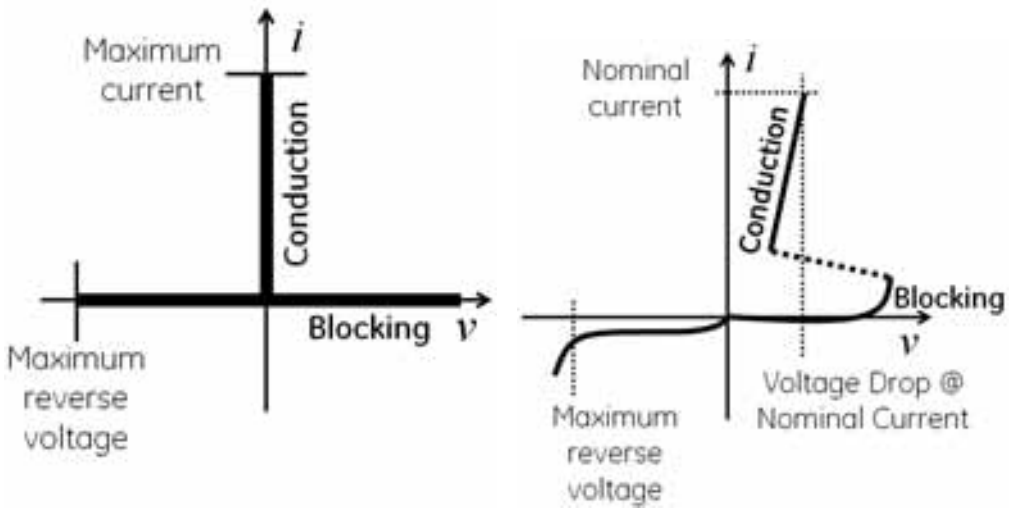

(a) Ideal characteristic **(b)** Real characteristic

Figure 3.5: Ideal and Real characteristic of a thyristor.

3.2.3 The uncontrolled three-phase bridge with diodes

The transmission and distribution of electrical energy is based upon the three-phase system, and most industrial equipment is fed by three-phase AC supply. The ideal three phase system is formed by three sinusoidal voltages (with the same constant amplitude) displaced in phase by 120 electrical degrees. In the rectifier bridge, the three-phase source is connected to a bridge that is composed of 6 diodes. In the scheme in Fig. 3.6, the diode bridge feeds a resistive load.

There will be always at least a diode that is conducting in the upper part of the bridge, and at least one in the lower part; which diode is/are conducting in each part depends on the phase to phase voltage in the three-phase source. Considering the three diodes in the upper part, that have a common cathode, the one that is conducting is that with the highest anode voltage; in the lower part the diode with the lowest voltage on cathode is conducting. When in the upper (lower) part there will be two diodes with the same anode (cathode) voltage, the diodes will be conducting simultaneously; this corresponds to the overlap period during the switching from one diode to another. The condition in which two switches are conducting in the same part will be detailed in the *Commutation Overlap* section. Note that the overlap between two switches is the result of a line inductance in the network that feeds the three-phase bridge. When no line inductance is present, the commutation is instantaneous so only one diode is conducting in each part.

In this case, the resulting output voltage v_d on the load is shown in Fig. 3.7.

The average value v_{d0} of the output voltage can be calculated as in Eq. 3.1:

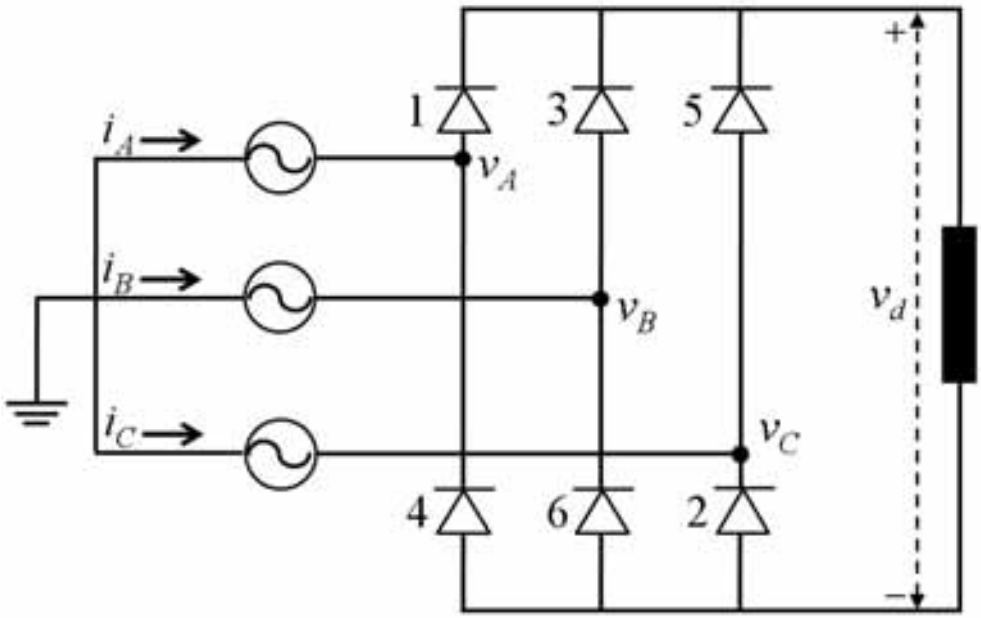

Figure 3.6: Scheme of a three phase diode bridge.

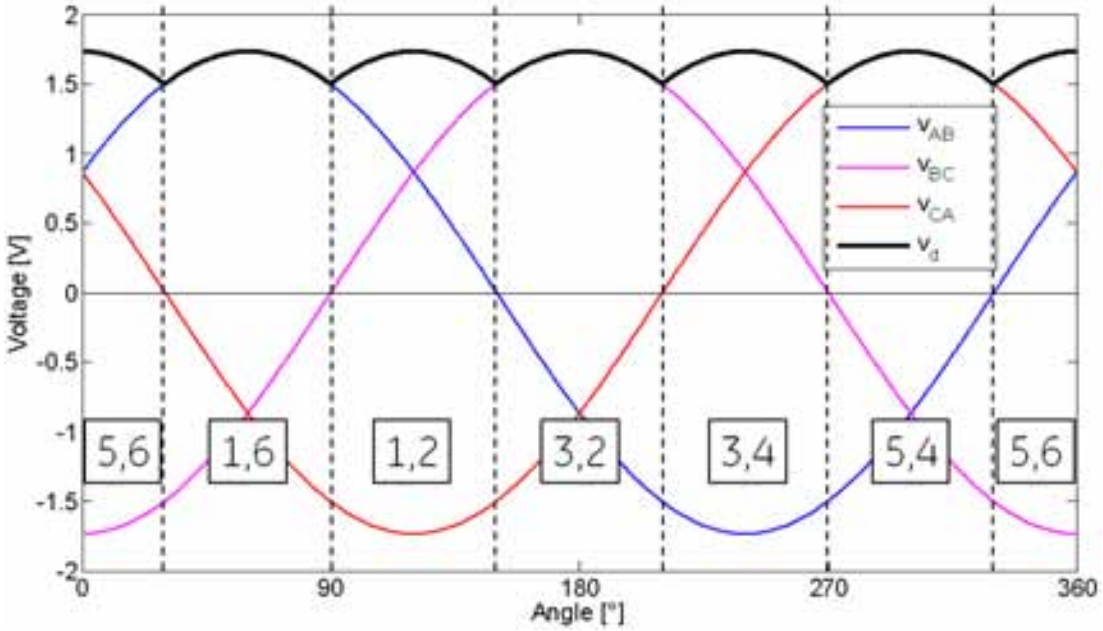

Figure 3.7: Three phase rectifier bridge: Output Voltage

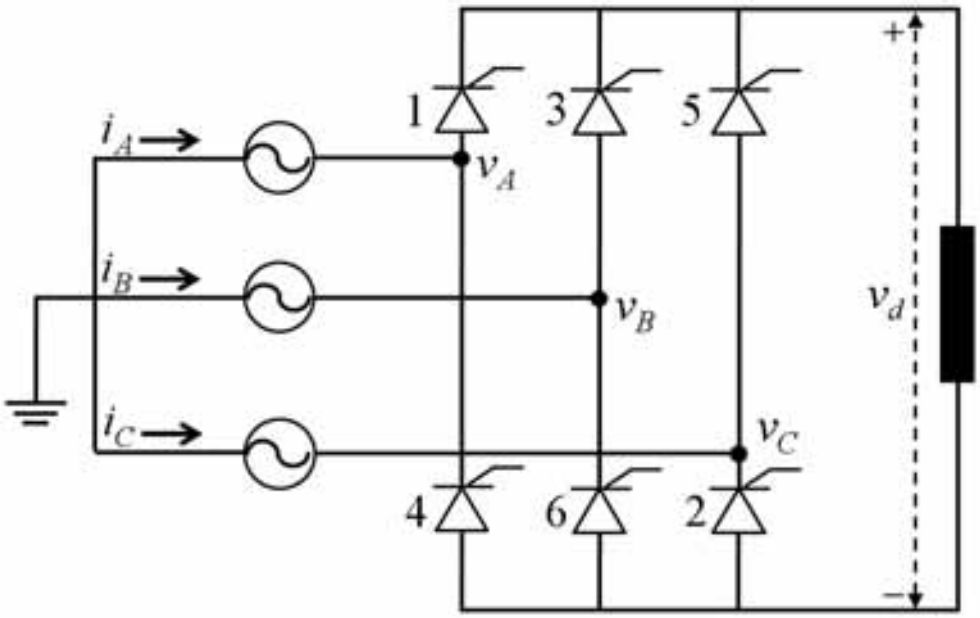

Figure 3.8: Scheme of a three phase thyristor bridge.

$$v_{d0} = \left(\frac{\int_{\frac{\pi}{3}}^{\frac{2\pi}{3}} \sqrt{3} v_{p-N} sin(\phi) d\phi}{\frac{\pi}{3}} \right) = \frac{3\sqrt{3}}{\pi} v_{p-N} = 1.654 v_{p-N} \tag{3.1}$$

where v_{p-N} is the 0-peak value of the phase to neutral voltage.

There are always two diodes carrying current simultaneously, one in the upper part of the bridge and one in the lower part. Each period in which a certain pair of diodes is conducting lasts 60 electrical degrees. Each diode conducts for two consecutive periods.

In one cycle the voltage v_d exhibits six pulses, that is why this operation is known as *six pulse mode*.

it is important to note that the output of this bridge is a continuous voltage applied to the load, with a fixed value. However the LCI inverter requires a DC current, which value has to be controlled considering that the counter-electromotive force of the load (that is the electrical motor) can vary during the operation. In the next subsection, the operation of the controlled three-phase bridge with thyristors will be detailed, in order to understand how the possibility to control the conduction of the switches allows to realize in output a DC current with a specified value.

3.2.4 The controlled three-phase bridge with thyristors

A three-phase bridge with thyristors is shown in Fig. 3.8 . A three-phase ideal sinusoidal generator is connected to a bridge composed of 6 thyristors. In the scheme in Fig. 3.8, the diode bridge feeds a resistive load.

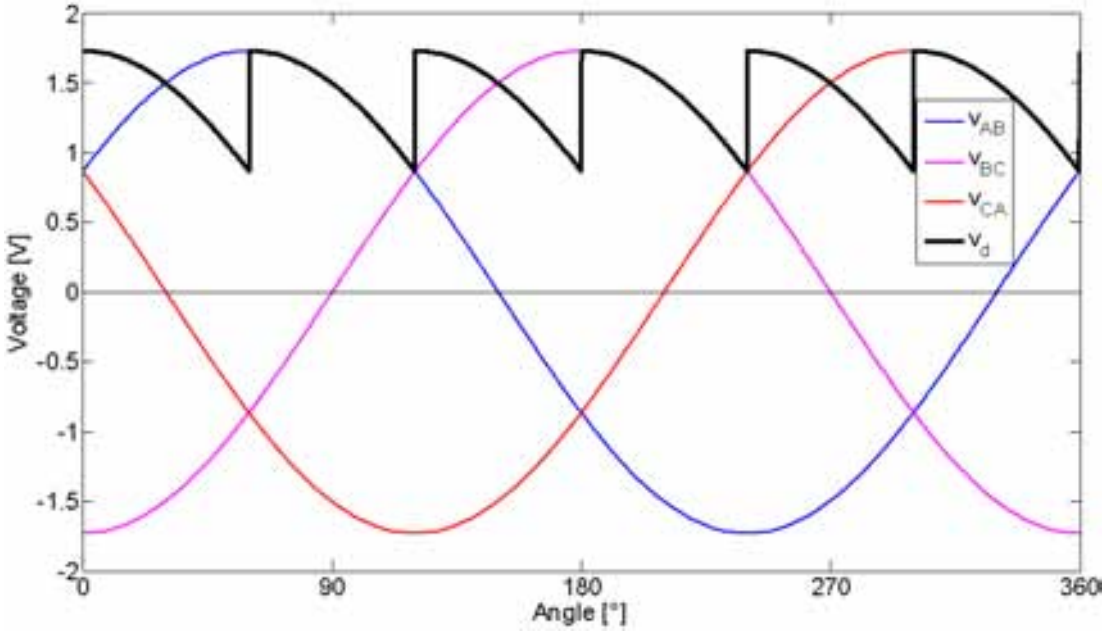

Figure 3.9: Three phase rectifier bridge: Output Voltage with firing angle equal to 30 °

In the controlled three-phase bridge with thyristors, an essential part of the converter is the control system, that produces the triggering pulses that allow the thyristors to conduct.

In the absence of triggering pulses the thyristors are non-conducting and, in the steady state, support the phase voltage of the supply.

The control pulses are synchronized to supply voltage. The reference point for the timing of the pulses can be assumed to be the natural turning-on point that would be experienced by diodes. The delay angle between this reference point and the point in which the thyristor is triggered is known as *firing angle* or triggering angle. Thus operation with firing angle equal to zero corresponds to the operation of an uncontrolled diode bridge; the voltage output will be the same as in Fig. 3.7.

The effect of using a non zero firing angle is to vary the output voltage of the converter. For instance, Fig. 3.9 shows the output voltage v_d applied to the load when the firing angle is equal to 30 °.

Note that the voltage is still a six-stepped wave, thus this operation is known as *six pulse mode*, as it has been previously shown for a diode bridge in Fig. 3.7.

Additionally, it is possible to note that the average voltage applied to the load is lower than in the uncontrolled diode bridge (that corresponds to a firing angle equal to 0 °).

It is possible to demonstrate that the average voltage $\bar{v}_d$ applied to the load is:

$$\bar{v}_d = v_{d0} cos(\alpha) \tag{3.2}$$

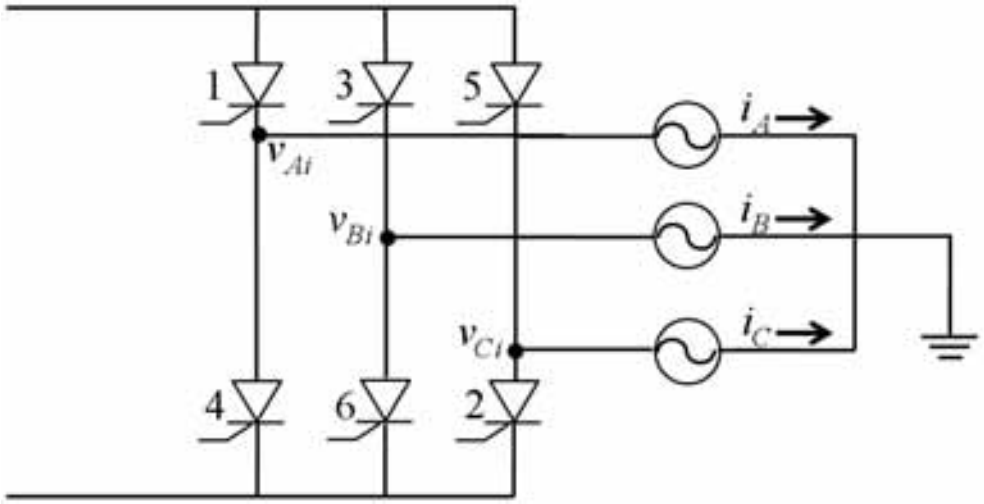

Figure 3.10: Scheme of a three phase thyristor bridge operated as an inverter.

where α is the rectifier firing angle and v_{d0} is the average voltage in output obtained with firing angle equal to 0°, as in Eq. 3.1. Starting from Eq. 3.2 it is possible to infer that if the bridge works as a rectifier (the energy flows from the AC side to the DC side), then the firing angle can assume values from 0° (maximum energy transfer) to 90° (average output voltage is zero).

If the firing angle is in the range from 90° to 180°, then the energy flows from the DC side to the AC side; in this condition, the three phase bridge works an inverter. A three-phase inverter is shown in Fig. 3.10.

3.2.4.1 Commutation Overlap

In the previous sections, the ideal three phase feeding network has been considered as directly connected to the thyristor bridge. However the converter is usually connected to a transformer that is fed by the network.

A secondary effect of the transformer is to introduce an additional series line inductance that modifies the conduction in the thyristor bridge. In both Fig. 3.7 and 3.9 it was assumed that there were always only two thyristors (or diodes) conducting at the same time: one in the upper part of the bridge and one in the lower part; the switching from a thyristor to another is considered to be instantaneous. For instance in 3.7, when the angle is equal to 90°, the thyristor 6 stops conducting and the thyristor 2 starts to conduct instantaneously.

However the effect of the line inductance is to determine a certain time of overlap between the subsequent conducting thyristors. Let us consider the system in Fig. 3.11. The load is described as a direct current source, because in a load commutated inverter the rectifier bridge has to realize in output a direct current, to feed the inverter.

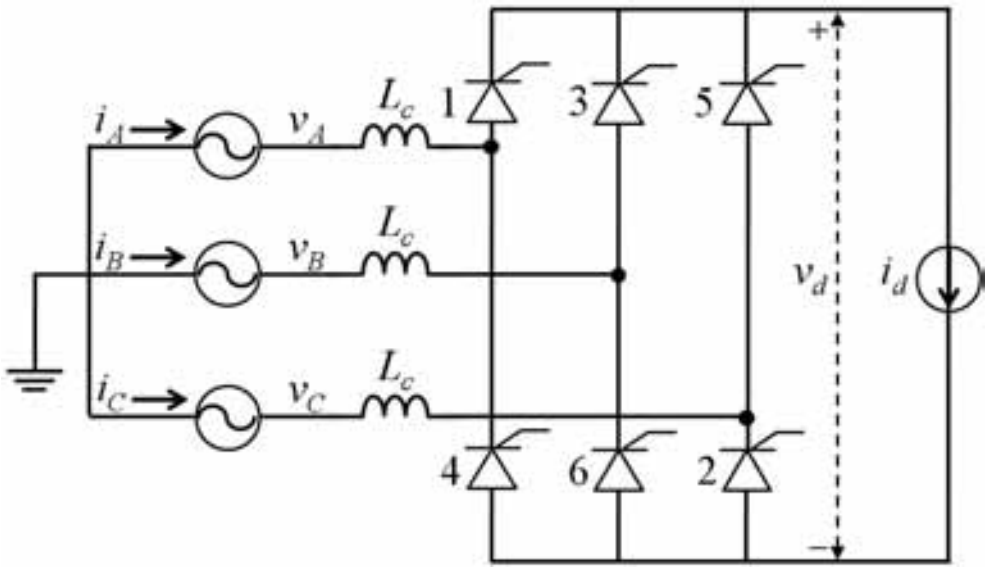

Figure 3.11: Scheme of a three phase rectifier with line inductance.

When there is a commutation between two thyristors, there will be a certain time period in which these thyristors will conduct simultaneously; in this time interval, the current in the previous conducting thyristor will go down to zero, while the current in the other one will rise to the nominal value i_d. The electrical angle corresponding to the overlap between these thyristors is known as overlap angle μ. By comparing Fig. 3.12 (no inductance) with Fig. 3.13 (non-zero inductance), that show the output voltage v_d and the thyristor currents in the upper part of the bridge, it is possible to understand the effect of the line inductance (figures from [24]).

As it is possible to see, during the commutation, the output voltage is reduced if compared with the case without commutation overlap.

If we consider the commutation from the thyristor 1 to 3 in the system depicted in Fig. 3.11, by applying the second Kirchoff circuit law it is possible to write:

$$\begin{cases} v_d = v_A - L_c \frac{di_1}{dt} \\ v_d = v_B - L_c \frac{di_3}{dt} \end{cases} \tag{3.3}$$

The first Kirchoff circuit law, applied to the node P, allows to write:

$$i_1 + i_2 = i_d \tag{3.4}$$

In this case i_d is fixed by the ideal current; however, even in the real system, we can consider that i_d is almost constant during the commutation, so that it is possible to write:

$$\frac{\mathrm{d}i_1}{\mathrm{d}t} + \frac{\mathrm{d}i_2}{\mathrm{d}t} = 0 \tag{3.5}$$

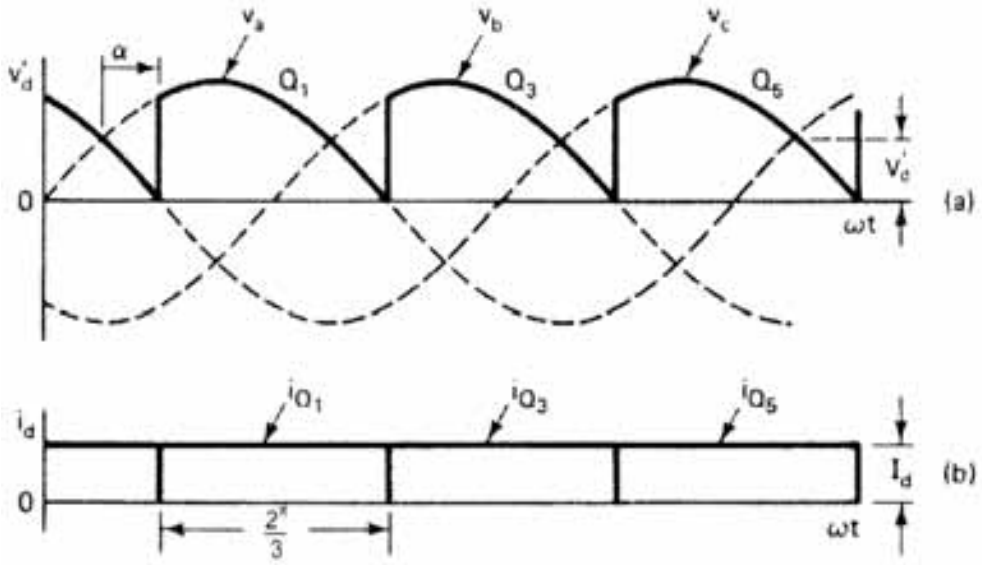

Figure 3.12: Output Voltage and Thyristors' Currents without Line Inductance Effect

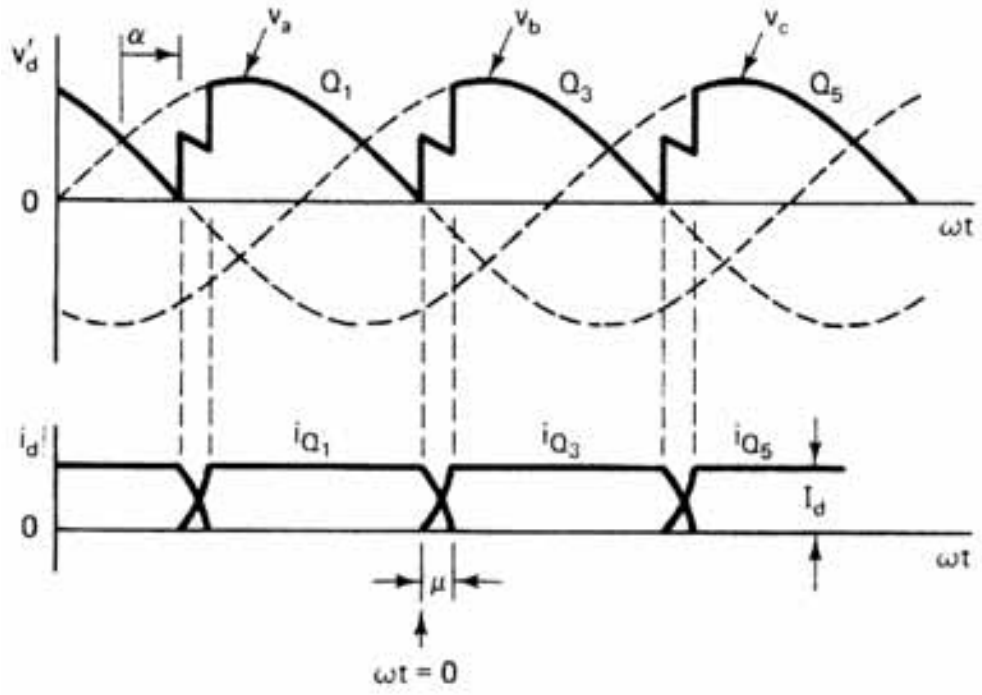

Figure 3.13: Output Voltage and Thyristors' Currents with Line Inductance Effect

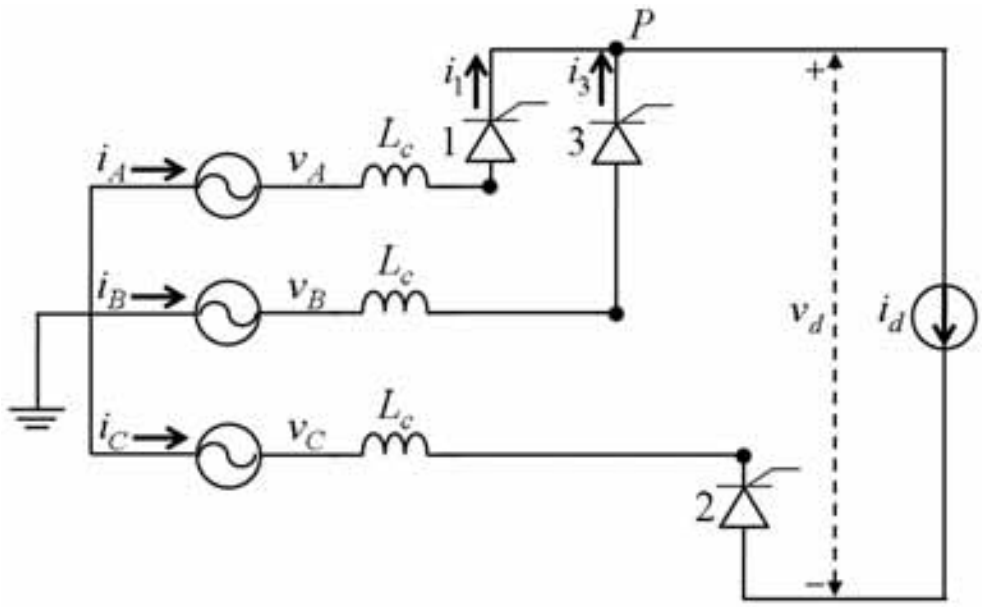

Figure 3.14: Equivalent circuit during commutation from thyristor 1 to 3

By imposing the equality of Eqs. 3.3 and considering the Eq. 3.5, it is possible to write:

$$v_d = \frac{1}{2}(v_A + v_B) \tag{3.6}$$

that means that during the commutation overlap the voltage applied to the load is the average value of the phase voltages connected.

By combining the first of 3.3 with 3.6, it is possible to conclude:

$$\frac{\mathrm{d}i_1}{\mathrm{d}t} = \frac{1}{2L_c}(v_A - v_B) \Rightarrow i_1 = \frac{1}{2L_c}\int (v_A - v_B)dt + C_0 \tag{3.7}$$

Considering that the phase to phase voltage $v_{AB} = v_A - v_B$ is:

$$v_{AB} = v_A - v_B = \sqrt{3}v_{p-N}sin(\omega t + \alpha) \tag{3.8}$$

where α is the rectifier firing angle and v_{p-N} is the 0-peak phase to neutral voltage. By substituting this expression in 3.7, it is possible to obtain:

$$i_1 = \frac{\sqrt{3}v_{p-N}}{2\omega L_c}cos(\omega t + \alpha) + C_0 \tag{3.9}$$

By considering $\omega t = 0$ when the commutation begins, the current i_1 in thyristor 1 will be equal to i_d, thus the integration constant C_0 can be evaluated:

$$C_0 = i_d - \frac{\sqrt{3}v_{p-N}}{2\omega L_c}cos(\alpha) \tag{3.10}$$

and substituted in 3.9 to obtain the current in thyristor 1:

$$i_1 = i_d - \frac{\sqrt{3}v_{p-N}}{2\omega L_c}[cos\alpha - cos(\omega t + \alpha)] \tag{3.11}$$

The current in thyristor 3 is calculated by substituting the calculated i_1 in Eq. 3.4:

$$i_3 = \frac{\sqrt{3}v_{p-N}}{2\omega L_c}[cos\alpha - cos(\omega t + \alpha)] \tag{3.12}$$

Considering that at the end of the commutation, when $\omega t = \mu$ (μ is the duration of the commutation overlap, and we choose $\omega t = 0$ when the commutation begins), the i_3 current is equal to i_d, thus it is possible to analytically calculate the overlap angle μ:

$$i_d = \frac{\sqrt{3}v_{p-N}}{2\omega L_c}[cos\alpha - cos(\omega t + \alpha)] \Rightarrow cos\alpha - cos(\omega t + \alpha) = \frac{2\omega L_c i_d}{\sqrt{3}v_{p-N}} \tag{3.13}$$

that allows us to conclude:

$$\mu = arccos(cos\alpha - \frac{2\omega L_c i_d}{\sqrt{3}v_{p-N}}) - \alpha \tag{3.14}$$

Eq. 3.14 shows that the overlap angle increases when the line inductance L_c and the direct current i_d are raised or when the phase-neutral voltage is reduced.

As it can be noted by comparing Fig. 3.12 with 3.13, the average voltage $\bar{v}_d$ in output from the thyristor bridge is reduced by the overlap; the reduction ΔV can be calculated as follows:

$$\Delta V = \frac{3}{2\pi}\int_0^{\mu}\frac{1}{2}(v_B - v_A)d\omega t = \frac{3\sqrt{3}v_{p-N}}{4\pi}[cos(\omega t + \alpha) - cos\alpha] \tag{3.15}$$

By substituting Eq. 3.13 in Eq. 3.15 it is possible to obtain:

$$\Delta V = \frac{3\omega L_c i_d}{2\pi} \tag{3.16}$$

Thus the average voltage applied to the load is:

$$\bar{v}_d = \frac{3\sqrt{3}v_{p-N}}{\pi}cos(\alpha) - 2\Delta V = \frac{3\sqrt{3}v_{p-N}}{\pi}cos(\alpha) - 2\frac{3\omega L_c i_d}{2\pi} \tag{3.17}$$

because there are two commutations on each cycle.

The overlap angle is very important during the operation as inverter, because it imposes a maximum value for the inverter firing angle β. As it was shown before, the bridge operates as an inverter when the firing angle is in the range from 90 ° to 180 °; however the commutation overlap imposes that the firing angle cannot exceed the value $180° - \mu$. Additionally it is necessary to consider the time t_{OFF} that the thyristors need to shut

down, that increases the margin needed for the commutation of an angle $\gamma = \omega t_{OFF}$; thus the maximum value for the inverter firing angle is $180\,^\circ - (\mu + \gamma)$. When the load is not constant, it is good practice to use an higher margin in order to avoid commutation failure.

3.2.4.2 Control of Rectifier Firing Angle in an Current-Fed converter

In a current-fed converter, the rectifier has to give in output a DC current, which value depends on air gap torque required to the electrical motor, as it will be demonstrated in the next sections.

The system is shown in Fig. 3.15 : the rectifier bridge feeds a load (that in our case will be the inverter bridge feeding the electrical motor) via an inductance.

As it has been described in the previous section, the average voltage $\bar{v}_d$ in output from the rectifier bridge can be controlled by regulating the rectifier firing angle, as in the equation 3.2. By applying the 2^{nd} Kirchoff's circuit law to the rectifier output, it is possible to write:

$$v_d - v_l = L\frac{\mathrm{d}i_d}{\mathrm{d}t} \tag{3.18}$$

The equation 3.18 shows that the current entering the load can be increased/decreased by regulating the voltage v_d: if the current should raise, then v_d have to be higher than v_l; vice-versa if the current has to decrease. As it has been shown before, the output voltage v_d can be regulated by varying the rectifier firing angle α according to Eq. 3.17. As it was already noted, during operation as a rectifier, the rectifier firing angle α can be varied from $0\,^\circ$ to $90\,^\circ$.

3.2.4.3 Harmonic components for a six pulse LCI converter

In the previous chapter, during the definition of the Campbell diagram, some of the exciting torque components due to a six pulse LCI converter have been presented; now it is possible to add further details to better understand the reason for these harmonic components.

It has been shown in Figs. 3.7 and 3.9 that the output voltage from the three-phase rectifier bridge (both with diodes or thyristors) is a six-stepped wave, thus this operation is known as six pulse mode. The scheme in Fig. 3.16 represents a six pulse LCI converter feeding a synchronous motor: the three-phase thyristor rectifier feeds a three-phase thyristor inverter with a DC current; the inverter is controlled to feed the motor with an AC current which frequency matches the rotating speed of the motor.

In high power applications however, a different architecture can be adopted, as it's shown in Fig. 3.17. As it's possible to see, in the rectifier side, two three-phase bridges are

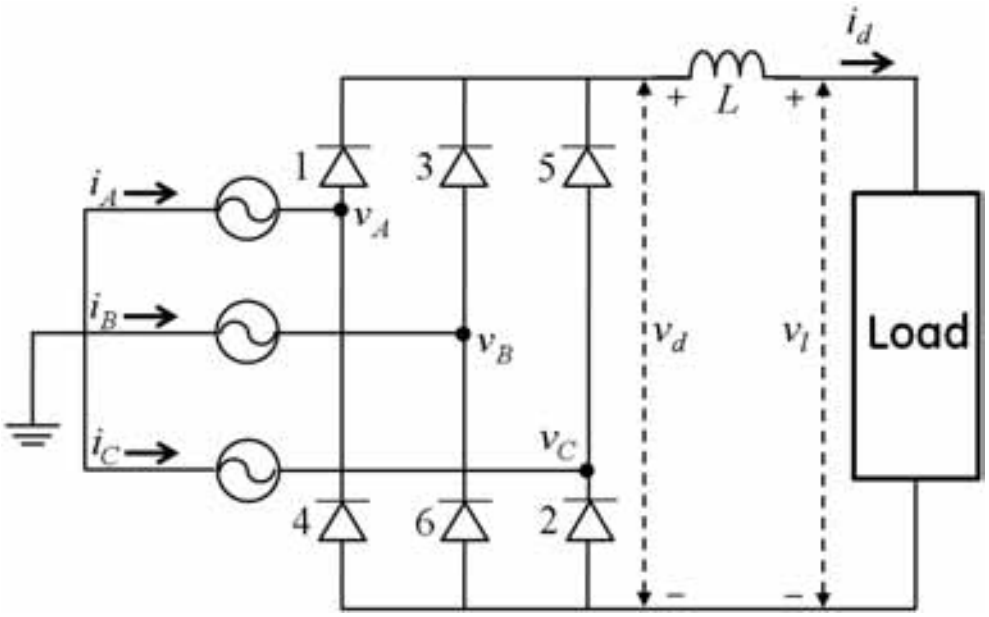

Figure 3.15: Three phase rectifier bridge feeding a load.

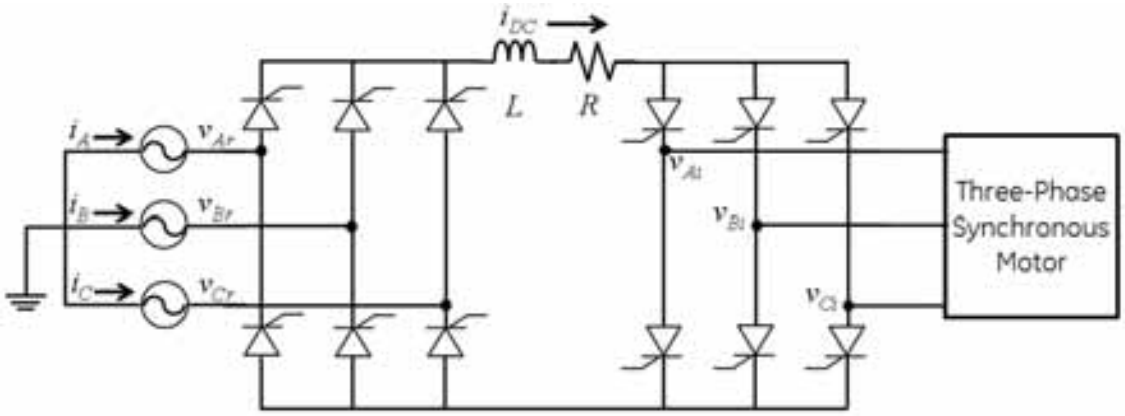

Figure 3.16: Scheme of a six-pulse LCI converter.

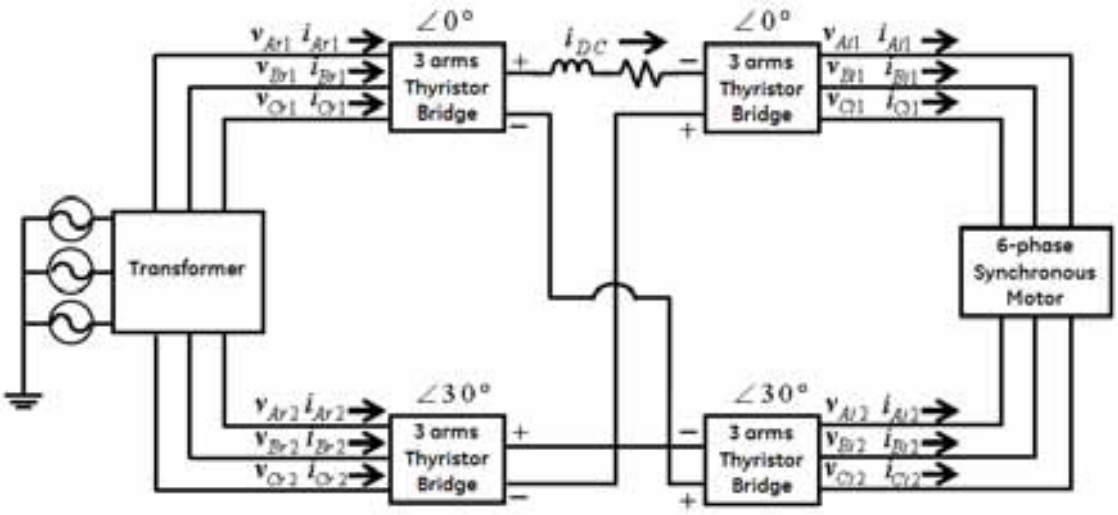

Figure 3.17: Scheme of a twelve-pulse LCI converter.

series connected: the output voltage on the inductance will be a twelve-stepped wave, thus the operation mode of this system is known as 12 pulse. This kind of architecture is useful to reduce the current ripple both in DC current (and both in line side and motor side), by installing both in rectifier and inverter side two bridges with a 30 ° phase displacement.

The frequencies of interharmonic components in output from a converter are given by Eq. 3.19:

$$f_{jk} = |n \cdot j \cdot f_m - n \cdot k \cdot f_n| \tag{3.19}$$

where j, k are integer indexes and n is the number of pulses. Thus, for a six-pulse converter, characteristic output frequencies will be $|6f_m - 6f_n|, |12f_m - 12f_n|, |12f_m - 6f_n|, |6f_m - 12f_n|$, but as it's possible to note, infinite components can be calculated by varying the indexes in Eq. 3.19. However, when higher values for indexes are considered (for instance $|6f_m - 18f_n|, |18f_m - 6f_n|, |12f_m - 18f_n|, |18f_m - 12f_n|$ and others), the amplitude of the resulting components is usually far lower than the above cited components, thus they are usually disregarded.

For a 12 pulse system, the most important components are those given by $|12f_m - 12f_n|$; the higher order components are usually negligible. As a matter of fact, the $|6f_m - 6f_n|$ components are theoretically canceled in 12 pulse systems; however the asymmetries that are always present in the real systems result also in non zero (but usually negligible) $|6f_m - 6f_n|$ components.

3.2.5 Synchronous Motors

A synchronous machine is an ac rotating machine whose speed under steady state condition is proportional to the frequency of the current in its armature. The magnetic field created by the armature currents rotates at the same speed as that created by the field current on the rotor, which is rotating at the synchronous speed, and a steady torque results.

Synchronous machines are commonly used as generators.

With power electronic variable frequency power supplies, synchronous motors are widely used for variable speed drives. If the stator excitation of a permanent magnet motor is controlled by its rotor position such that the stator field is always 90° (electrical) ahead of the rotor, the motor performance can be very close to the conventional brushed DC motors. The rotor position can be either detected by using rotor position sensors or deduced from the induced emf in the stator windings. Since this type of motors do not need brushes, they are known as brushless DC motors.

The advantages in not having brushes are the possibility to operate at higher speed, with a less frequent maintenance; the total weight and inertia of the motor are also reduced.

The stator of a synchronous machine consists of a ferromagnetic core with internal slots, a set of three-phase distributed stator windings placed in the core slots, and an outer framework with end shields and bearings for the rotor shaft. The turns of the stator windings are equally distributed over pole-pairs, and the phase axes are spaced $\frac{2\pi}{3}$ electrical radians apart.

The cross-sectional shape of the rotor can be salient or cylindrical. Salient pole construction is mostly used in low-speed applications where the diameter to length ratio of the rotor can be made larger to accommodate the high pole number. Salient pole synchronous machines are often used in hydro generators to match the low operating speed of the hydraulic turbines. Salient here, refers to the protruding poles; the alternating arrangement of pole iron and interpolar gap results in preferred directions of magnetic flux paths or magnetic saliency.

The cylindrical or round rotor construction is favored in high-speed applications where the diameter to length ratio of the rotor has to be kept small to keep the mechanical stresses from centrifugal forces within acceptable limits.

The magnetic field on the rotor can be provided by permanent magnets, or by a field winding on the rotor that is excited by DC current. The DC power supply required for excitation usually is supplied through a generator known as exciter, which is often mounted on the same shaft as the synchronous machine. Various excitation systems using AC exciter and solid state rectifiers are used with large motors (or large turbine generators).

The importance of having a field winding which current can be regulated by a control system is that it is possible to regulate the power factor of the electrical motor. This is very important because by operating the motor with a leading power factor, it allows to have a self commutation in the inverter; this is exactly what is done in a Load Commutated Inverter drive, where the load (the motor) turns off the thyristors in the inverter bridge, without the needing of an external system that regulates the turning off of semiconductor valves.

The advantages of an LCI drive with synchronous motor are those already mentioned for synchronous motor with DC exciter (no brushes and the possibility to regulate the power factor) plus the feasibility of very large motors (power higher than 40 MW).

An extended description of the operation of the synchronous motor is beyond the scope of the present dissertation; the reader can go into more depth by reading [25].

Chapter 4

Closed Loop Electro-Mechanical Model Implementation

4.1 Model Overview

The system that has been analyzed during the research activity is an LNG train made of a Gas Turbine, three Centrifugal Compressors and a Synchronous Motor fed by a Load Commutated Inverter (Rated Speed $\approx$ 3600 [rpm] = $60Hz = f_m$). The network frequency f_n is 50 Hz. An overview of the train is shown in Fig. 4.1.

The electro-mechanical model includes:

- a mechanical model that describes the torsional dynamics of all the machines in the shaft line;
- the speed governor;
- the high level gas turbine model;
- the compressors' resistant characteristics;
- the electrical model of the drive.

As it is possible to see, the electro-mechanical model includes all the terms that determine the torque acting on the shaft line, from the turbomachines (gas turbine and compressors) to the variable frequency drive.

An overview of the model is shown in Fig. 4.2.

The speed of the LNG train in the gas turbine shaft is an input for the Speed Governor, that regulates the reference torque for the electrical motor and the reference torque for the gas turbine. The electrical model of the VSD calculates the actual torque applied by the drive on the shaft line, while the torque applied by the gas turbine is calculated by another

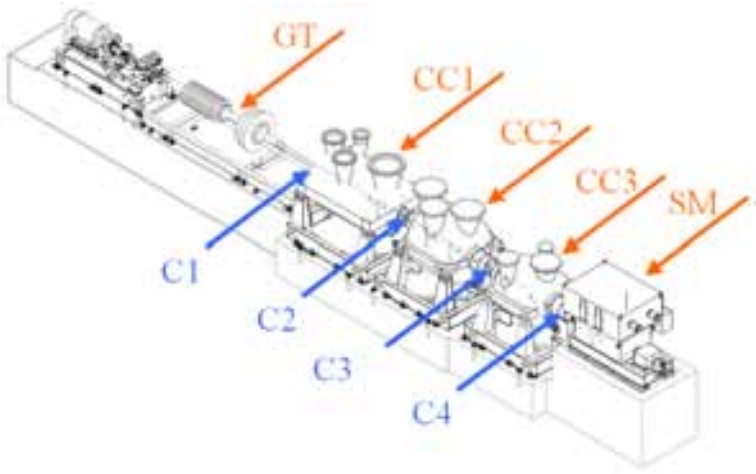

Figure 4.1: LNG train Overview

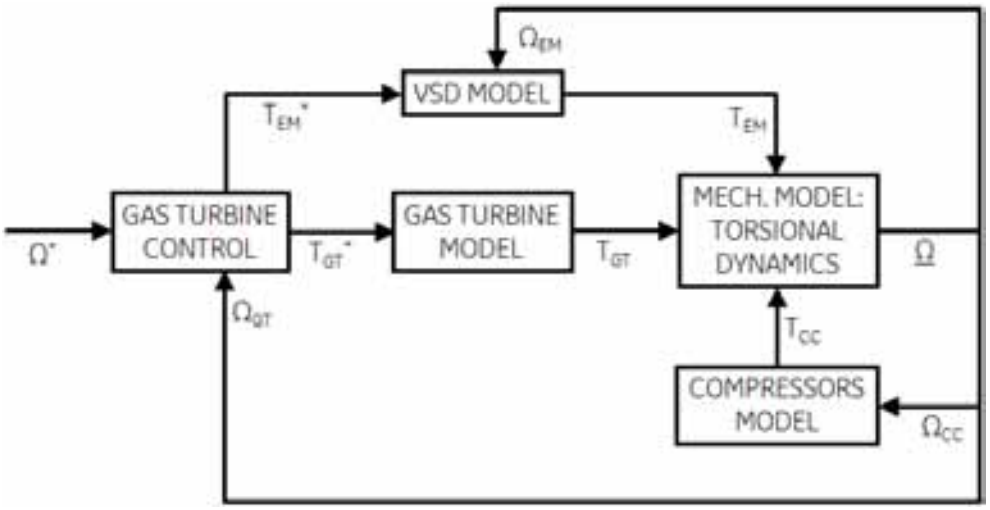

Figure 4.2: High-Level Diagram of the Electro-Mechanical Model

block describing the gas turbine output. The torque applied by these machines and the torque applied by compressors are the inputs of the mechanical model, that describes the torsional dynamics of the train; in output the torsional model gives the rotating speed of the shaft line in all machines' sections. The actual speed in compressors' shafts is the input of the compressors' model, that calculates the resistant torque applied by compressors, while the speed in the gas turbine's shaft is the feedback that enters the Speed Governor; additionally the electrical motor speed enters the dynamic model of the electrical drive, because the speed of the motor shaft affects the dynamics of the electrical system.

The electro-mechanical model has been implemented in *MatLab/Simulink*™ environment; the solver is an Ode 23t, that is the implementation of the trapezoidal rule using a free interpolant suited for stiff problems, giving a solution without numerical damping.

In the next sections, the different part of the model will be detailed.

4.2 Speed Governor

The Speed Governor model and the gas turbine model are both derived from the journal paper [26]. The cited paper describes a full model for the simulation of the dynamics of several gas turbines made by General Electric, including the gas turbine that is included in the compression train that has been analyzed during this research activity.

However, the aim of the research project is to define a simulation model for conditions in which the reference speed is constant, resulting in a train speed that is kept nearly constant by the control system. For these conditions it is possible to use a simplified simulation model that is also included in [26].

In the simplified model, the speed governor can be described as a transfer function that, given the speed error, calculates the reference torque T^*, as in Fig. 4.3. The static gain and the time constant of the speed governor can be adjusted during commissioning of the compression train. In the simulation model the value that has been implemented reflects those used in the analyzed system. The output of the transfer function is saturated, considering the maximum torque that the motors (gas turbine and electrical motors) are able to apply to the mechanical system.

The model described in [26] do not consider that there can be two motors: in that model the reference torque T^* becomes the input of the gas turbine governor. However in this case the reference torque has to be split in two terms: the reference value for the gas turbine T^*_{GT} and the reference value for the electrical motor T^*_{EM}. In the simulation model developed by the author, it is possible to regulate the gas turbine torque as a percentage of the reference total torque T^*.

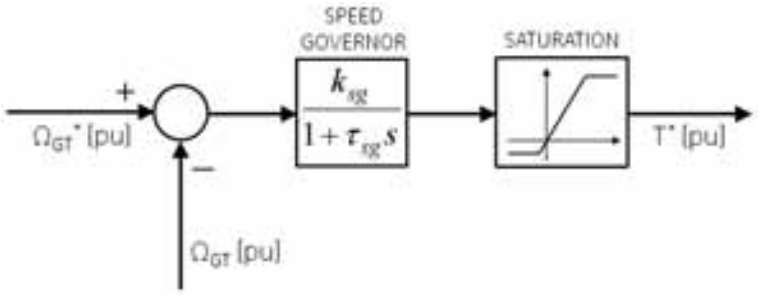

Figure 4.3: Simplified Model of the Speed Governor

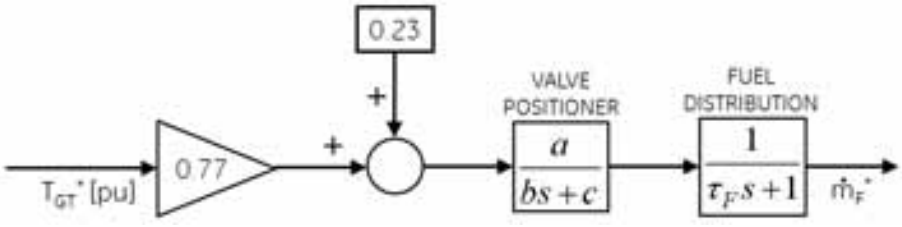

Figure 4.4: Turbine Torque Control

4.3 Gas Turbine's Model

The model of the output torque given by the gas turbine is derived by the aforementioned paper [26]. The fuel mass flow rate $\dot{m}$ is calculated considering the reference torque for the gas turbine. The reference torque is multiplied by 0.77 and the value 0.23 is added, because the gas turbine output torque is positive only if the mass flow rate is higher than the 23% of the rated fuel flow. This is due to the energy adsorbed by the turbine's compressor; in this application the gas turbine runs at constant speed with zero output torque when the fuel mass flow rate is 23% of the rated value. The fuel exceeding that value will lead to a positive torque output of the gas turbine.

The first transfer function describes the dynamics of the positioning system of the fuel control valve, while the second transfer function considers the downstream piping and the fuel distribution manifold.

The time constants related to the fuel control valve and downstream piping, that can be evaluated considering the model developed in [26], realize a cut-frequency for the large gas turbine present in the analyzed system that is lower than $1.5Hz$, while the TNF values are usually far from this value. That is why the influence of the gas turbine on the torsional dynamics is usually disregarded.

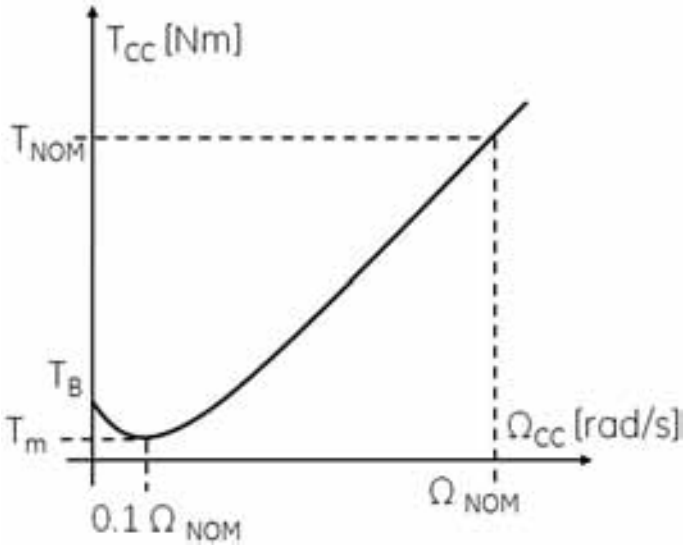

Figure 4.5: Compressor' Resistant Torque

4.4 Compressors' Model

The model includes a simplified description of the compressors' resistant torque, that is described as a function of the compressors' speed.

The resistant curve is a parabolic curve, that is constructed considering the passage trough three points: the first point is that at zero speed, in which the resistant torque is equal to the breakaway torque T_B; the second point corresponds to the minimum resistant torque, that is considered a fraction of the breakaway torque, and that is supposed to occur at 10% of the nominal speed. The third point corresponds to the nominal operating point, in which the speed is equal to the nominal speed Ω_{NOM} and the torque is equal to the nominal torque T_{NOM}.

Considering this model, when the reference speed is constant, the compressor' resistant torque can be approximated to the tangent to the curve in the simulated operating point, because the speed oscillations in compressors' shafts have usually a low amplitude.

The compression string can operate continuously in a speed range around the nominal speed Ω_{NOM}, with a minimum continuous speed that is higher than $0.1 \cdot \Omega_{NOM}$ (10% of the nominal speed). Thus, inside the operating speed range, the resistant torque is monotonically increasing with the speed, resulting in a positive slope of the tangent line. The compressor' torque, for small speed variations, is thus approximated with a constant term plus a line with a positive slope. The latter term introduces a torsional damping in the system, because if the speed increases the resistant torque rises thus having a braking effect on the shaft; vice versa if the speed decreases.

4.5 Variable Speed Drive Model

The definition of a simulation model for the VSD has been the most challenging part of the activity. The simulation model has been developed in *MatLab/Simulink*™, without using the SimPowerSystems toolbox, in order to have the maximum portability of the model; additionally, only few information about the drive have been available from manufacturer. The main goal in the development of this model is to realize a tool that can describe the dynamics of the electro-mechanical system, considering the limited information available and with a limited computational burden.

Firstly, the definition of the model of the main hardware included in the drive is described; secondly the description of the control logics implemented is detailed.

4.5.1 Hardware Modelling

An overview of the electrical system is shown in Fig. 4.6. The three-phase feeding network is the input of a transformer that modifies the peak voltage and gives in output two three phase sinusoidal systems, with a phase displacement phase equal to 30 ° electrical degrees. These three-phase systems feed two rectifier bridges; the output of each rectifier is a DC current that enters an inverter bridge. The two three-phase inverters feed a six-phase synchronous motor with an AC current which frequency matches the angular speed of the machine.

Note that this system is different from the one depicted in Fig. 3.17. In this application there are two DC links, and each one is working as a six-pulse system; however, by feeding the synchronous machine with the output of these systems, with a 30 ° phase displacement, the output torque will exhibit the harmonic components typical of a 12-pulse system (N.B typical components of a 6 pulse system are not exactly canceled, but their amplitude is usually far lower than 12-pulse components).

In the next subsections, the modelling of the main hardware is described.

4.5.1.1 Feeding Network and Transformer

In order to limit the computational burden of the dynamic model, a detailed description of the feeding network and of the transformer are neglected, because it has been supposed that their characteristics do not affect the dynamics in the scope of the present dissertation.

The system that feeds the two rectifier bridges is described as two ideal three phase systems, with a constant 30 ° electrical degrees phase displacement. The phase voltage is a constant amplitude sinusoid; the 0-peak phase to ground voltage is equal to the nominal output of the transformer V_{TR}. The input voltages are described in Eq. 4.1. No limit is

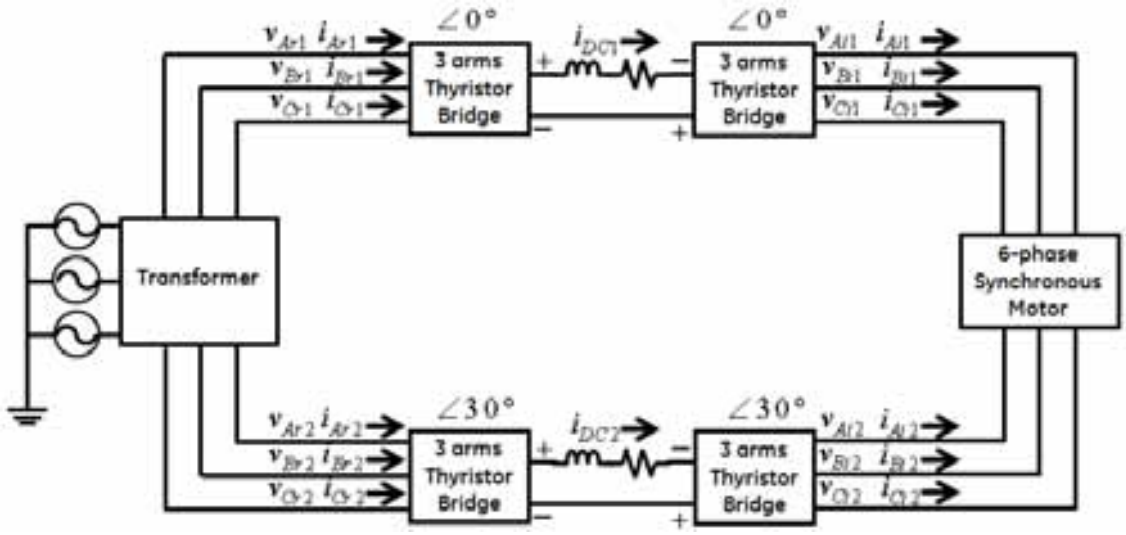

Figure 4.6: Overview of the Electrical System

given to the output current of the ideal sinusoidal generator.

The line inductance included in the model of the feeding system is necessary in order to model the commutation overlap in thyristor bridges (see next subsection); the value of the line inductance has been calculated considering the commutating reactance of the transformer.

$$\begin{aligned} v_{Ar1} &= V_{TR}\sin\left(2\pi f_{LINE}t\right) \\ v_{Br1} &= V_{TR}\sin\left(2\pi f_{LINE}t - \tfrac{2}{3}\pi\right) \\ v_{Cr1} &= V_{TR}\sin\left(2\pi f_{LINE}t - \tfrac{4}{3}\pi\right) \\ v_{Ar2} &= V_{TR}\sin\left(2\pi f_{LINE}t + \tfrac{\pi}{6}\right) \\ v_{Br2} &= V_{TR}\sin\left(2\pi f_{LINE}t - \tfrac{2}{3}\pi + \tfrac{\pi}{6}\right) \\ v_{Cr2} &= V_{TR}\sin\left(2\pi f_{LINE}t - \tfrac{4}{3}\pi + \tfrac{\pi}{6}\right) \end{aligned} \tag{4.1}$$

4.5.1.2 Three-Phase Thyristor Bridge Model

In the electrical drive that has been analyzed in the present dissertation, there are four thyristor bridges: two of them are working as rectifiers while the other two work as inverters. The model that has been developed for the description of a three phase bridge is the same for all bridges; the only difference between rectifiers and inverters is in the connection of the terminal of these circuits.

The three-phase thyristor bridge has been modeled in *Simulink*™ by introducing a *MatLab*™ function that receives in input the phase to phase voltages applied to the bridge, the value of the current in the DC side and the triggering pulses to the thyristors' gates; at each integration step the function calculates the current and the voltage drop in

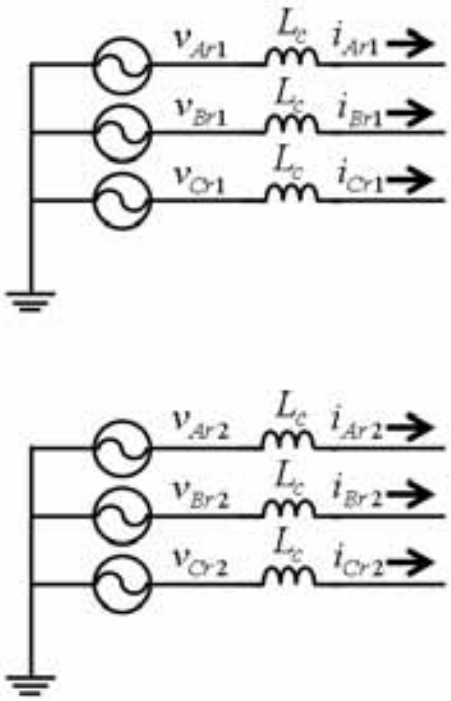

Figure 4.7: Model of the input to the rectifier

each thyristor, thus allowing to calculate the voltage in the DC side of the bridge.

In order to understand the calculations operated in the *MatLab*$^{\mathrm{TM}}$ function, it is necessary to consider the rectifier bridge depicted in Fig. 3.8. Considering the circuit described in the aforementioned figure, it is possible to write:

$$\begin{gathered}
\Delta v_1 + v_d + \Delta v_2 = v_A - v_C = v_{AC} \\
\Delta v_3 + v_d + \Delta v_4 = v_B - v_A = v_{BA} \\
\Delta v_5 + v_d + \Delta v_6 = v_C - v_B = v_{CB} \\
v_d = -(\Delta v_2 + \Delta v_5) = -(\Delta v_6 + \Delta v_3) = -(\Delta v_4 + \Delta v_1) \\
i_A = i_1 - i_4 \\
i_B = i_3 - i_6 \\
i_C = i_5 - i_2 \\
i_d = i_1 + i_3 + i_5 = i_2 + i_4 + i_6
\end{gathered} \tag{4.2}$$

where Δv_i and i_i are the voltage drop and the current across the i^{th} switch.

Firstly we consider an ideal diode bridge. As it has been shown in the previous chapter, the characteristic of a diode does not allow a positive voltage across the switch.

Now let us consider a certain condition in terms of signs of the phase to phase voltages; for instance it is possible to choose:

$$\begin{aligned} v_{BA} &< 0 \\ v_{AC} &> 0 \\ v_{CB} &> 0 \end{aligned} \tag{4.3}$$

By considering the equations for voltages in 4.2 we find:

$$\begin{aligned} \Delta v_1 > \Delta v_5 > \Delta v_3 \\ \Delta v_6 > \Delta v_2 > \Delta v_4 \end{aligned} \tag{4.4}$$

As it has been stated before, the ideal diode does not allow a positive voltage across the switch, thus the unique solution is:

$$\begin{aligned} \Delta v_1 &= 0 \\ \Delta v_6 &= 0 \\ \Delta v_3 &< 0 \\ \Delta v_2 &< 0 \\ \Delta v_5 &< 0 \\ \Delta v_4 &< 0 \end{aligned} \tag{4.5}$$

Considering the characteristic of the ideal diode, it is possible to conclude that in this condition only diodes 1 and 6 are conducting. This means that once the signs of phase to phase voltages are known, it is possible to easily evaluate which diodes are conducting.

If diodes are substituted with ideal thyristors, the equation for voltages and currents are still valid, but now we have to consider that if a thyristor is not triggered on, it can withstand also a positive voltage. This means that the signs of the phase to phase voltages are not enough to evaluate which thyristors are conducting, but additional information is needed about the triggering of the gates of thyristors.

As it has been done for the diodes, once the signs of phase to phase voltages are known, it is possible to write a relation as in Eq. 4.4. In this case, for instance, if thyristor 1 has been triggered, then it will be:

$$\begin{aligned} \Delta v_1 &= 0 \\ \Delta v_3 &< 0 \\ \Delta v_5 &< 0 \end{aligned} \tag{4.6}$$

so thyristor 1 is conducting, while 3 and 5 are off; if thyristor 1 has not been triggered, but 3 has been triggered, then it will be:

$$\begin{aligned} \Delta v_1 &> 0 \\ \Delta v_3 &= 0 \\ \Delta v_5 &< 0 \end{aligned} \tag{4.7}$$

that means that 3 is conducting while 1 and 5 are off; finally, if both 1 and 3 have not been triggered, 5 is conducting, according to:

$$\begin{aligned} \Delta v_1 &> 0 \\ \Delta v_3 &> 0 \\ \Delta v_5 &= 0 \end{aligned} \tag{4.8}$$

The equations that have been detailed consider the condition of no commutation overlap between thyristors; when a line inductance is present, the expression of the current in commutating thyristors during the overlap has been shown in the *Commutation Overlap* subsection in chapter 3.

Concluding, the embedded *MatLab*™ function allows to calculate the voltage drop and current on each thyristor and the output voltage of the thyristor bridge, as a function of DC link current, phase to phase voltages and triggering of thyristors.

4.5.1.3 Six-Phase Synchronous Motor

The electrical motor adopted is a six-phase synchronous motor that is fed by two three-phase inverters with a 30 ° electrical degrees phase displacement. This architecture is adopted in order to reduce the ripple in the output torque of the electrical motor.

In order to have a limited computational burden, the electrical motor has been described with a simplified model that reproduces the essential features that are considered important in the present activity, avoiding a full model of the six-phase machine.

The working principle of the synchronous machine is to have a stator field and a rotor field that are rotating at the same speed [25]. Thus it is possible to assume that the frequency of the phase voltages corresponds to the rotating speed multiplied with the number of pole pairs in the electrical machine.

The electrical motor is thus described as two three-phase machines, that give an output voltage at terminals which frequency is related to the rotor speed, according to the above described assumption.

The amplitude of motor voltage is also related to the speed as it is shown in Fig. 4.8. When the motor speed is lower than the nominal speed, the excitation current is regulated in order to keep constant the flux at its nominal value, thus resulting in a motor voltage that is proportional to the motor speed. When the motor speed is higher than the nominal

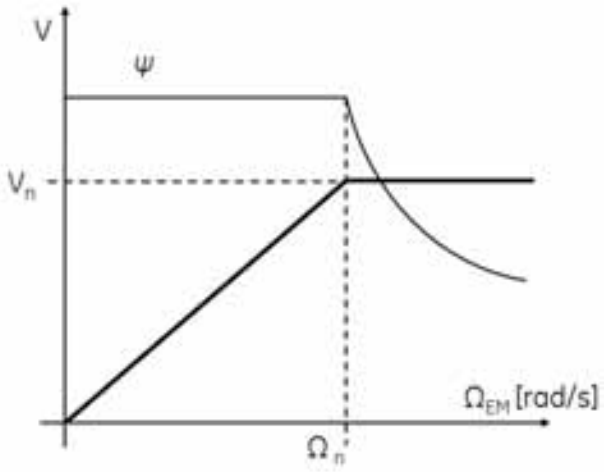

Figure 4.8: Motor Voltage versus Speed

speed, the excitation current is regulated to keep the motor voltage constant and equal to its nominal value.

The control loop acting on the excitation current has been designed by the drive's vendor to have a low bandwidth; considering the slow response of this control loop it is possible to assume that if the reference motor speed is kept constant, the control loop is not sensitive to speed oscillations related to torsional vibrations, because the torsional vibrations occur at TNFs whose frequencies are higher than the control loop bandwidth. That is why the motor model assumes constant flux that means a motor voltage proportional to the motor speed. The simplified motor model is shown in Fig. 4.9; Eqs. 4.9 show the motor voltage on each phase as a function of motor speed Ω_{EM} and rotor angular position ϑ_{EM}. $V_{n(p-n)}$ is the nominal phase to neutral motor voltage (0-peak value) and Ω_n is nominal motor speed.

$$\begin{aligned}
v_{Ai1} &= \frac{V_{n(p-n)}}{\Omega_n}\Omega_{EM}\sin\left(\vartheta_{EM}t\right) \\
v_{Bi1} &= \frac{V_{n(p-n)}}{\Omega_n}\Omega_{EM}\sin\left(\vartheta_{EM}t - \tfrac{2}{3}\pi\right) \\
v_{Ci1} &= \frac{V_{n(p-n)}}{\Omega_n}\Omega_{EM}\sin\left(\vartheta_{EM}t - \tfrac{4}{3}\pi\right) \\
v_{Ai2} &= \frac{V_{n(p-n)}}{\Omega_n}\Omega_{EM}\sin\left(\vartheta_{EM}t + \tfrac{\pi}{6}\right) \\
v_{Bi2} &= \frac{V_{n(p-n)}}{\Omega_n}\Omega_{EM}\sin\left(\vartheta_{EM}t - \tfrac{2}{3}\pi + \tfrac{\pi}{6}\right) \\
v_{Ci2} &= \frac{V_{n(p-n)}}{\Omega_n}\Omega_{EM}\sin\left(\vartheta_{EM}t - \tfrac{4}{3}\pi + \tfrac{\pi}{6}\right)
\end{aligned} \tag{4.9}$$

The dependency of machine's voltages on motor speed is a very important effect in torsional electro-mechanical interaction: the speed oscillations of electrical motor's shaft, due to torsional vibrations, produce an harmonic component on machine's voltage. The electrical motor is the load of the rectifier bridges, thus the harmonic components on motor voltages produce harmonic components on DC current, because the rectifier sees

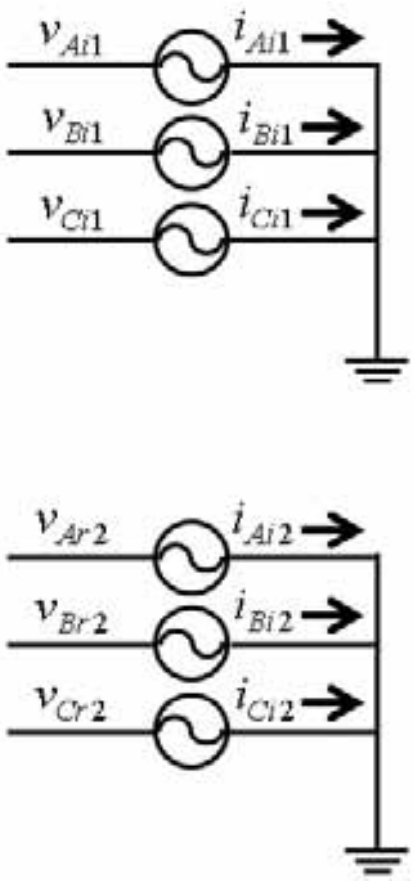

Figure 4.9: Scheme of the Electrical Motor Model

a time-varying load. The DC current, via the rectifier bridges, feeds the motor, thus the harmonic components on DC current are reflected on phase currents. Then, considering that the air-gap torque depends on currents, it is possible to conclude that the air-gap torque will have harmonic components at the same frequency of speed oscillations. This effect is very important, because if the air-gap torque components are in counterphase with speed oscillations, then the electrical drive will be damping the speed oscillations, while if these harmonics are in phase, then the electrical drive will be exciting torsional vibrations, thus resulting in possible high-amplitude vibrations or even instability.

The motor output torque is usually calculated by the implementation of a d, q model of the machine, that is a description of the machine in a reference frame that rotates with the rotor, with the direct axis d that coincides with the direction of rotor flux phasor and the quadrature axis q normal to the d axis. This model is known as Park's transformation; the reader can go more in depth by reading [25].

Phase currents and voltages are transformed in the d, q reference frame using a transformation matrix, that depends on the angular position of the electrical motor shaft, that can be obtained by integrating the shaft rotational speed. The motor air gap torque is then calculated as:

$$T_{EM} = k \cdot p \cdot (\psi_d i_q - \psi_q i_d) \tag{4.10}$$

where i_d, i_q are the current in direct and quadrature axis, ψ_d, ψ_q are fluxes in direct and quadrature axis, p is the number of pole pairs and k is a constant which value depends on the transformation matrix that has been used in the transformation to d, q reference frame.

However the d, q model requires as an input the rotor speed of the machine; this input is available in the motor model, but it is not available for the real motor; in order to coherently compare the simulation results with measurements, it has been decided to use the same algorithm for torque calculation both for simulations and measurements.

Thus the Clarke's transformation algorithm has been applied: in this algorithm the physical quantities (voltages and currents) are calculated in a fixed reference frame α, β, where the direction α is coincident with the magnetic axis of the stator phase A. The algorithm for the calculation of the air gap torque for a three phase motor is shown in Fig. 4.10, where $v_{Ai1}, v_{Bi1}, v_{Ci1}$ are motor phase voltages, $i_{Ai1}, i_{Bi1}, i_{Ci1}$ are motor phase currents. The label i denotes that voltages and currents are on inverter side, while the label 1 denotes that the calculation refers to the first three phase motor; the algorithm is the same for the second three phase system (the six phase synchronous motor is described as two distinct three-phase machines). Phase voltages and currents are transformed in the α, β reference frame according to Eq. 4.11. Voltages in the α, β reference frame are then

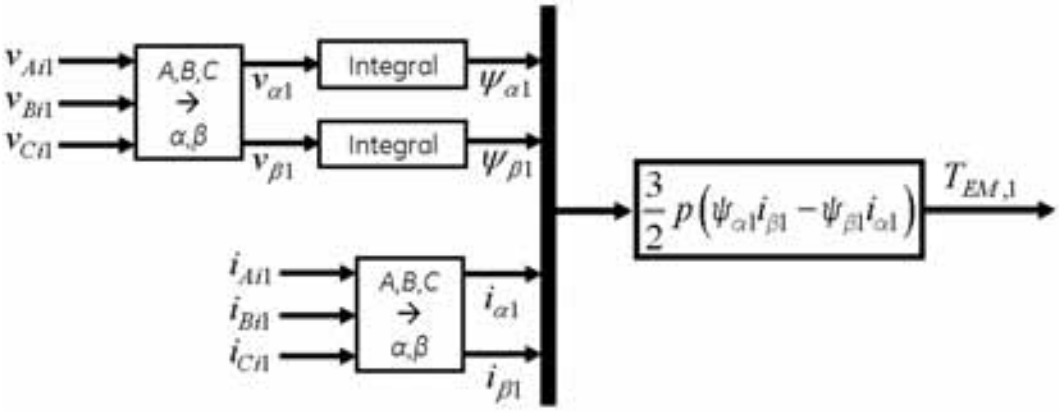

Figure 4.10: Air Gap Torque Calculation

integrated to obtain machine fluxes ψ_α, ψ_β. Air Gap Torque is then calculated considering also the number of machine pole pairs p, according to the Eq. shown in Fig. 4.10.

$$\begin{bmatrix} v_\alpha \\ v_\beta \end{bmatrix} = \frac{2}{3} \cdot \begin{bmatrix} 1 & -\frac{1}{2} & -\frac{1}{2} \\ 0 & \frac{\sqrt{3}}{2} & -\frac{\sqrt{3}}{2} \end{bmatrix} \cdot \begin{bmatrix} v_a \\ v_b \\ v_c \end{bmatrix} \tag{4.11}$$

4.5.2 Variable Speed Drive Control Scheme

The Reference motor air-gap torque, coming from the Speed Governor, is converted in a reference DC link current. Then, the rectifier units are controlled, acting on the firing angle of thyristors, in order to have an output voltage from the rectifier that gives the desired DC link current. By acting on the inverter firing angle and on the excitation field of the electrical machine is then possible to control the machine power factor. The main equations and control loops will be detailed in the next subsections.

4.5.2.1 Calculation of reference DC link current

The mechanical power output P_m of the electrical motor is given by multiplying the average motor air-gap torque in a period T_{EM} with the motor speed Ω_{EM}; considering the power balance on the electrical machine it is possible to write that the mechanical power P_m is equal to the electrical power entering the machine P_e multiplied with the conversion efficiency of the electrical machine η:

$$P_m = P_e \cdot \eta = T_{EM} \cdot \Omega_{EM} \tag{4.12}$$

The machine's efficiency is supposed to be constant and equal to the nominal efficiency at 100% load. The electrical power entering a three-phase AC machine can be written in

the form:

$$P_e = \sqrt{3} V_s I_s cos(\phi) \tag{4.13}$$

where V_s and I_s are the RMS value of the fundamental (that means the harmonic component which frequency equals the speed of the electrical machine) of the phase to phase voltage and phase current; $cos(\phi)$ is the power factor of the machine. The second term of Eq. 4.13 should be multiplied with 2 in our case, because the electrical machine is composed of 2 three-phase systems.

The power factor $cos(\phi)$ can be approximated with the cosine of the inverter firing angle, that is a function of DC link current I_{DC} and line voltage V_L, as it will be shown in Fig. 4.13.

In this application, the machine vendor implemented a look-up table that calculates the inverter firing angle as a function of DC link current; then, for reduced line voltage, the calculated inverter firing angle is modified by subtracting a correction term.

This control logic is peculiar to this VSD system. In order to write a relation with general validity, the power factor is substituted with a general function of the average DC link current and 0-peak amplitude of line voltage.

Then it is possible to write, for the six phase electrical motor:

$$P_e = 2\sqrt{3} V_s I_s cos(\phi) = \eta 2\sqrt{3} V_s I_s f(I_{DC}, V_L) \tag{4.14}$$

Note that in other drives, the correction due to line voltage can be absent, and $cos(\phi)$ can be only a function of DC link current.

The RMS phase current I_s can be evaluated, considering that the current entering the machine is a square wave with amplitude equal to the average DC current. I_s is the RMS value of the fundamental harmonic component, that for a square wave can be written as:

$$I_s = \frac{\sqrt{6}}{\pi} I_{DC} \tag{4.15}$$

Additionally the phase voltage is related to the speed of the electrical machine, as in Eq. 4.9. The 0-peak phase to neutral voltage V_p can be written as:

$$V_{p(0-peak)} = \frac{V_{n(p-n)}}{\Omega_n} \Omega_{EM} \tag{4.16}$$

Thus the 0-peak phase to phase voltage is:

$$V_{s(0-peak)} = \sqrt{3} V_{p(0-peak)} = \frac{V_n}{\Omega_n} \Omega_{EM} \tag{4.17}$$

where $V_n = \sqrt{3} V_{n(p-m)}$ is the nominal phase to phase voltage (0-peak). while the RMS

value V_s is:

$$V_s = \frac{1}{\sqrt{2}} \frac{V_n}{\Omega_n} \Omega_{EM} \tag{4.18}$$

By substituting the expression of V_s (Eq. 4.18) and I_s (Eq. 4.15) in the Eq. 4.13, it is possible to write:

$$P_e = 6 \frac{V_n}{\Omega_n} \Omega_{EM} I_{DC} f(I_{DC}, V_L) \tag{4.19}$$

Then by equating the expression of the electrical power 4.19 with the mechanical power, as in Eq. 4.12 it is possible to write:

$$P_m = T_{EM} \cdot \Omega_{EM} = P_e \cdot \eta = \eta \frac{6 V_n}{\Omega_n} \Omega_{EM} I_{DC} f(I_{DC}, V_L) \tag{4.20}$$

Thus the motor air gap torque can be calculated dividing both terms by the electrical motor speed Ω_{EM}:

$$T_{EM} = \eta 6 \frac{V_n}{\Omega_n} I_{DC} f(I_{DC}, V_L) = \eta \frac{6\sqrt{2} V_{n(RMS)}}{\Omega_n} I_{DC} f(I_{DC}, V_L) \tag{4.21}$$

where the RMS value of the phase to phase nominal motor voltage $V_{n(RMS)}$ has been introduced, because it represents the rated voltage of the electrical machine.

Summarizing, the average air gap torque in a period, given by the electrical motor, has been expressed as a function of rated voltage $V_{n(RMS)}$, nominal speed Ω_n, DC current I_{DC} multiplied with the function $f(I_{DC}, V_L)$ that represents the dependency of the power factor $cos(\phi)$ with the DC current and line voltage.

Once the relation $cos(\phi) = f(I_{DC}, V_L)$ is known, the non-linear relation between air gap torque T_{EM} and DC current I_{DC} shown in Eq. 4.21 can be inverted, thus allowing the calculation of the DC current that is needed for a certain torque output. Thus the reference air gap torque (that comes from the Speed Governor) is converted in a reference DC link current.

4.5.2.2 Control of Rectifier Firing Angle

The DC link current is controlled by acting on the rectifier firing angle α, as it has been briefly shown in the previous chapter for a three-phase rectifier feeding a load (see Eq. 3.18).

In the analyzed system, the load is a three-phase inverter bridge, as it is possible to see in Fig. 4.11.

The DC link current is related to the voltage on the DC side of the thyristor bridges, as in Eq. 4.22 :

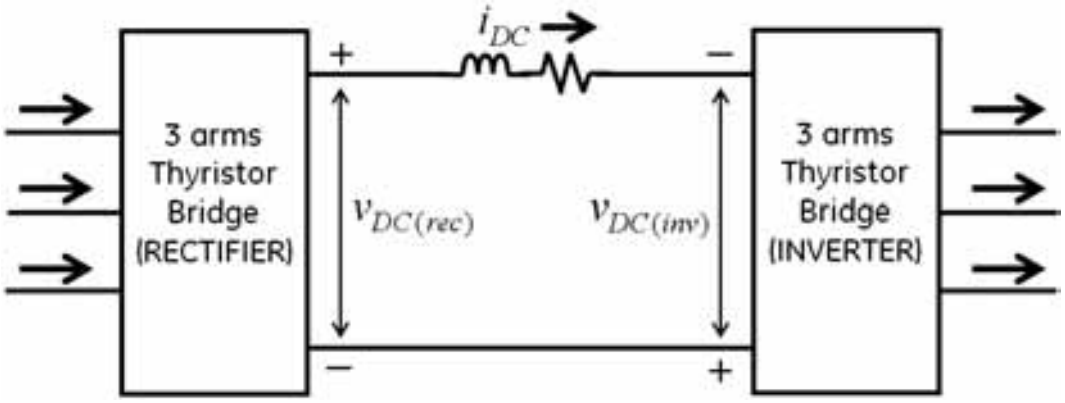

Figure 4.11: DC link current control

$$v_{DC(rec)} - v_{DC(inv)} = L_{DC}\frac{di_{DC}}{dt} + R_{DC}i_{DC} \tag{4.22}$$

where L_{DC} and R_{DC} are the inductance and resistance of the DC link.

The voltage drop $v_{DC(inv)}$ is related to the operation of the electrical motor; $v_{DC(rec)}$ is regulated by acting on the rectifier firing angle, according to Eq. 3.17, that is now rewritten as a function of V that is the RMS phase to phase voltage on the AC rectifier side, calculated as $V = v_{p-n}\frac{\sqrt{3}}{\sqrt{2}}$:

$$v_{DC(rec)} = \frac{3\sqrt{2}V}{\pi}cos(\alpha) - \frac{3\omega L_c i_d}{\pi} \tag{4.23}$$

The Eq. 4.23 allows to calculate the rectifier firing angle that is needed to obtain a certain voltage on the rectifier DC side; thus it is possible to calculate α as a function of the reference voltage on rectifier side $v_{DC(rec)}$.

The rectifier reference voltage is calculated as a function of the error on DC link current: the reference I^*_{DC} (that is a function of the reference torque, as it has been shown in the previous subsection) is compared with the actual current I_{DC} (the current measure is filtered with a first order low-pass filter). The error on DC current is the input of a PI controller, that outputs the reference DC voltage on rectifier side.

The control of the rectifier firing angle can be then described as in Fig. 4.12.

4.5.2.3 Control of Inverter Firing Angle

The control logic for the inverter firing angle is shown in Fig. 4.13. It must be noted that this control logic is peculiar to this drive, and it can be different in other drives with the same architecture.

Firstly it must be noted that a thyristor bridge works as an inverter when the firing angle is in the range from 90 ° to 180 °; however in the previous chapter it has been shown

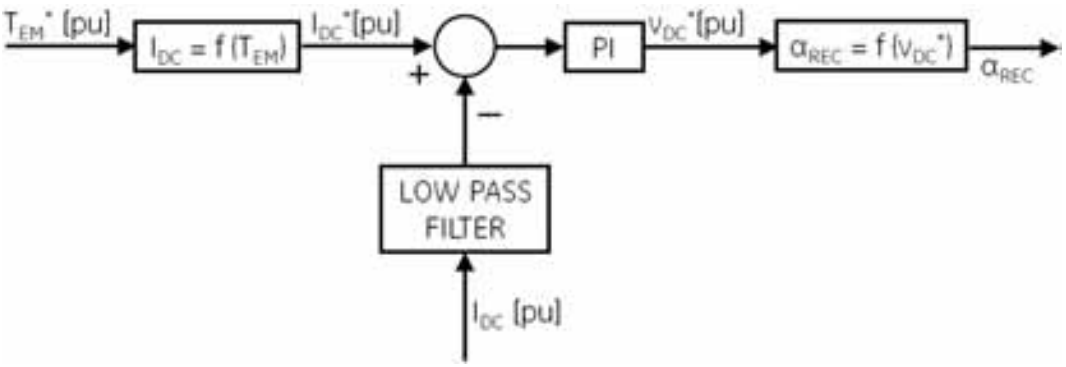

Figure 4.12: Control of Rectifier Firing Angle

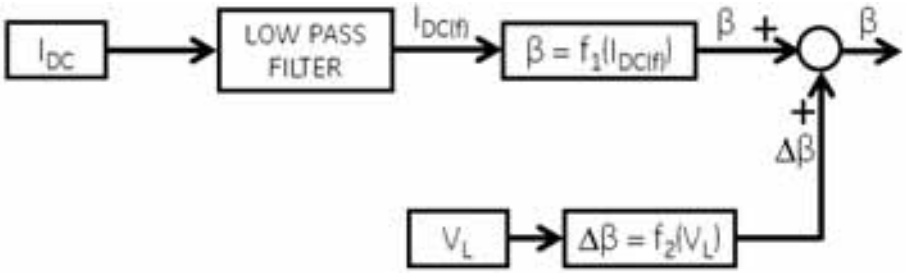

Figure 4.13: Control of Inverter Firing Angle

that considering the time for commutation overlap and the time needed to turn off a thyristor, the inverter firing angle should not exceed a maximum value that is lower than 180 °. Additionally when the load is not constant, it is good practice to use an higher margin in order to avoid commutation failure.

In the control logic implemented in the analyzed drive, a look up table calculates a reference inverter firing angle as a function of the filtered DC link current. The output value is always lower than a value β_{lim} that has been chosen to have a proper margin to avoid commutation failure.

Additionally, a correction that considers the line voltage V_L is applied; this correction can only reduce the value of the reference inverter firing angle.

4.5.2.4 Triggering of thyristors

The rectifier and inverter firing angles are controlled by the logics that have been described in previous sections; then the thyristors have to be triggered in order to actuate that firing angle.

Let us consider a thyristor bridge: the frequency of the phase to phase voltages applied to that bridge is integrated over time. Note that in rectifier bridges the frequency is the network frequency that is supposed to be constant, while in the inverter bridges the frequency of phase to phase voltages is given by the rotational speed of the electrical

motor shaft (multiplied with the number of pole pairs of the machine).

There is one integrator for each thyristor. The integrator for each thyristor is set to zero every time the phase to phase voltages assume the signs that would allow the conduction of that thyristor. If thyristors were substituted by diodes, that would be the time in which the diode would start to conduct. That time instant corresponds to firing angle equal to zero.

The frequency of phase to phase voltages f is multiplied with 2π to obtain the pulsation $\omega = 2\pi f$; by integrating over time the pulsation, an angle is obtained. This output angle is compared with the reference firing angle: when the output of the integrator equals the reference firing angle, a triggering pulse is sent to the thyristor, in order to turn it on.

The procedure implemented in the developed model probably does not reflect the actual triggering system in the VSD; usually in the real drives a Phase Locked Loop system (PLL) receives in input the phase voltages, and detects the zero-crossing of phase-to-phase voltages.

The dynamics of the PLL are very important for the motor side bridges, because the switching of thyristors produces sudden voltage drops in motor phase voltages that can lead to an erroneous detection of a zero-crossing. This phenomenon is shown in the next chapter in Fig. 5.3, where it is possible to see that in the measured phase to phase voltage there are zero crossings due to the commutations in thyristors, while in the simulation model these crossings are absent because of the simplifying hypotheses implemented in the model In the real system, the PLL (or another control logic) filters this signals in order to avoid erroneous zero crossing detections.

The absence of the dynamics of this control logic in the developed model may lead to a different dynamic response of the triggering system; this may result in a different dynamic behavior of the model, if compared with the real system.

4.5.2.5 Control of Excitation Field

The excitation current is the output of a controlled three-phase rectifier bridge with thyristors. The reference excitation current is calculated in order to obtain 100% of nominal flux in the speed range from zero to the nominal speed of the machine.

Tests conducted by the vendor of the drive demonstrated that the control loop acting on the excitation current is very important in terms of stability of the closed loop electro-mechanical system. In order to minimize the risks of instability, the control loop has been set in order to be very slow (high time constants), thus it has been decided not to introduce this loop on our simplified model, because we supposed that the very slow control loop could not affect the dynamics related to electro-mechanical instability.

4.6 Mechanical Model for Torsional Dynamics

In the previous sections, it has been described how the torque applied by each machine is calculated. In all the machine's models, the torque is calculated considering as an input the machines' speed. However no clarifications have been made in order to describe how the speed of each machine is calculated.

The model for torsional dynamics allows to calculate the speed of the shaft of each machine considering as an input the torque applied by each machine. The torsional model is described in Fig. 4.14: the torque calculated for each machine is multiplied with a proper vector that allows to apply each torque in the correct shaft.

Then a transformation in modal coordinates is operated, via the modal matrix $[\Phi]$, in order to reduce the computational burden. The transformation from physical coordinates to modal coordinates and vice-versa has been detailed in Chapter 2. The second order differential equations, previously shown in Eq. 2.17, can be solved by integrating twice. The output of the integrators are the amplitude and the speed of each modal coordinate. By multiplying the vector of modal coordinates with the transpose $[\Phi]^T$ of the modal matrix, it is possible to calculate the physical quantities such as the angular position and the speed of all sections in the shaft line.

From the vector that contains the speed of all sections it is possible to extract the speed of the shaft of each machine, while the angular position allows to calculate the torque acting on couplings, as in Eq. 2.30.

The Amplification Factor for torsional modes, that is included in Eq. 2.17, is supposed to be the same for all torsional modes; the selected value comes from experience in similar compression trains.

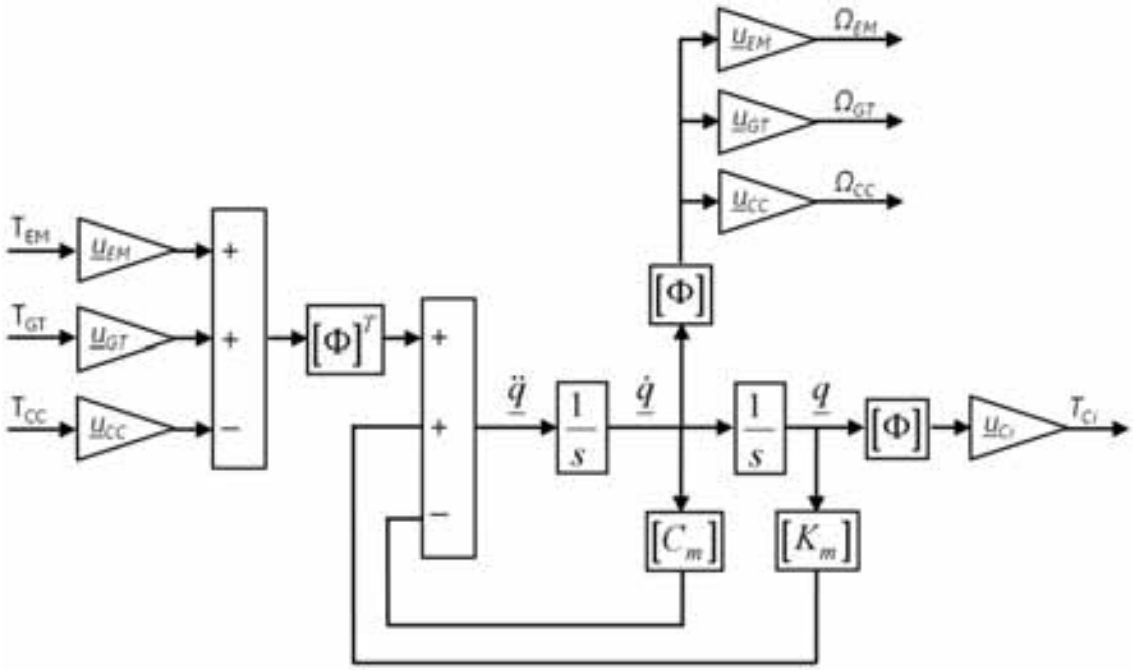

Figure 4.14: Simulation Model for Torsional Dynamics

Chapter 5

Model Validation: Simulation Results Compared with Measurements

The electro-mechanical model that has been described in the previous chapter, has been firstly validated by checks on the output quantities, comparing them with the theoretical output values. Then the most important part of the activity began: the simulation results have been compared with the measurements that have been performed during the testing of the compression string, in order to understand if the simulation model is able to predict the closed loop behavior of the electromechanical system.

Firstly, a brief introduction on the measurement system implemented in the compression train is given. Then the simulation model is tested using different control parameters, in order to evaluate the closed loop behavior of the electro-mechanical system. Finally the simulation results are compared with measurements.

5.1 Data Acquisition System

During the test phase of the compression string, a Data Acquisition System has been set up in order to monitor the operation of the system. The set up allowed the collection, analysis and storage of electrical, mechanical, thermal and thermodynamic data measured for the equipment under test.

Considering the need to study the closed loop behavior of the entire electromechanical system and the torsional response, synchronization of the acquisition of all variables (both mechanical and electrical) is fundamental.

Moreover, the data acquisition system implemented is able to perform real-time analysis in order to identify dynamic events as soon as they arise. For example real time Fast Fourier Transforms (FFTs) allow observation of the excitation of natural modes almost immediately if something in the system changes during the tests. Waterfall diagrams are

a convenient graphical representation for the FFT output, since they show the frequency content of the signal over time.

All electrical variables related to the main motor (such as motor currents, phase to phase voltages, excitation current, etc.) were acquired by means of external current and voltage probes. Additional measurements on internal quantities (such as DC-link currents, motor electromagnetic torque calculated by the drive's control system, etc.) were performed using an optical fiber digital link with the LCI converter control board.

The verification of the torsional behavior requires the measurement of torques transmitted between machines. Torque measurements have been set up on two couplings, because they are the most flexible elements in the mechanical system and yield the highest response. First the coupling on the drive end side of the electric motor has been instrumented in order to observe the torque which the motor transmits to the train. In addition, the coupling in which the first mode shape has a node (turbine side) has been monitored because the first mode is usually the most problematic in electromechanical interactions, and in the node there is the highest transmitted cyclic torque for a given oscillation level, has it has been detailed in Chapter 2.

The measurements were done using two different methods: the torque on the motor side coupling has been acquired both using a strain gauge system and a temporary Phase Shift method, while the other coupling has been monitored using a Phase Shift system, that will also be used at the installation site.

5.2 Closed Loop Behavior of the Electro-Mechanical system

The closed loop behavior of the electro-mechanical system has been tested by evaluating the effect of a speed oscillation of the electric motor's shaft on the air gap torque given in output by the electrical drive. The aim of these simulations is to understand how the electric motor reacts to torsional vibrations of the shaft line, that can be caused for instance by torque steps given by the electrical motor itself or excitations due to the other machines in the shaft line.

The motor speed is kept initially constant and equal to the reference value; then a speed disturbance is added, which amplitude is equal to $0.2 rad/s$. The amplitude of the speed disturbance has been chosen considering that it is consistent with an high amplitude torsional vibration that can arise in the shaft line, without compromising the resistance of couplings. The frequency of the speed disturbance is $5Hz$; this value has been chosen because it is considered the minimum value for the first TNF for long shaft lines (and it is quite close to the first TNF of the compression string analyzed in the present dissertation).

Tests have been performed considering two different torque set points (TSP) for the electrical motor: TSP = 20% of the rated torque and TSP = 100% of the rated torque. For each TSP, three different values have been implemented for the proportional gain K_P in the PI current controller, while the integral gain K_I has been kept constant. This reflects the real tests that have been conducted on the compression string.

The exact values used for the K_P and K_I constants have been omitted, because of intellectual property reasons. Thus, the values for K_P are referred to as high, medium and low.

The results are presented in the form of Fast Fourier Transforms (FFTs) of significant quantities, such as Air Gap Torque AGT, DC link current I_{DC}, rectifier and inverter firing angle α and β. The FFTs are shown in Tables 5.1, 5.2, 5.3, 5.5, 5.6 and 5.7.

The components of Air Gap Torque are normalized by dividing them with the electric motor Rated Torque, while those of the DC currents are normalized using the rated DC current.

The frequency of the components shown in tables, has been chosen considering the architecture of the analyzed drive: $50Hz$ is the network frequency f_n, $60Hz$ is the motor frequency f_m. As it is possible to see in Fig. 4.6, the system is composed of two AC to AC converters, that are both 6-pulse converters. That is why the output DC link current I_{DC} will have the highest components at $6 \cdot f_n = 300Hz$, given by the 6-pulse rectifier bridge and at $6 \cdot f_m = 360Hz$, given by the 6-pulse inverter bridge.

The rectifier and inverter firing angles are controlled using the filtered DC link current (the first is controlled by a PI system, while the second is controlled by a look-up table), thus also these signals will have the highest components at $300Hz$ and at $360Hz$.

The Air Gap Torque (AGT) in output from the electrical motor is the sum of the torque given by two three-phase 6-pulse systems, that have a 30 ° phase displacement. This phase displacement reduces the output torque ripple, because the typical components of the 6-pulse systems ($6 \cdot f_m$ and $6 \cdot f_n$) will be in counter-phase, thus reducing their amplitude in the total output torque. That is why, by observing the FFT of the Air Gap Torque, the amplitude of the $6 \cdot f_m$ and $6 \cdot f_n$ components is very low, while the most important components are those at $12 \cdot f_m$ and $12 \cdot f_n$, because the torque components at these frequencies given by the two three-phase systems will be in phase.

In the presented FFTs there will be also a component at $5Hz$, given by the speed disturbance on the electric motor's shaft.

Table 5.4 shows the variation of the components at $5Hz$ when the K_P constant is varied from the low value to the high value: the variation ΔX is calculated as in Eq. 5.1:

$$\Delta X = \frac{X(K_P\ high) - X(K_P\ low)}{X(K_P\ low)} \tag{5.1}$$

Variable	X(5 Hz)	X(50 Hz)	X(60 Hz)	X(300 Hz)	X(360 Hz)	X(600 Hz)	X(720 Hz)
AGT[pu]	$1.47 \cdot 10^{-3}$	$9.69 \cdot 10^{-5}$	$8.21 \cdot 10^{-3}$	$5.96 \cdot 10^{-5}$	$5.38 \cdot 10^{-5}$	$1.19 \cdot 10^{-2}$	$3.08 \cdot 10^{-2}$
I_{DC}[pu]	$1.03 \cdot 10^{-3}$	$2.92 \cdot 10^{-5}$	$1.22 \cdot 10^{-3}$	$5.63 \cdot 10^{-2}$	$3.43 \cdot 10^{-2}$	$1.35 \cdot 10^{-2}$	$8.21 \cdot 10^{-3}$
$\alpha[^\circ]$	$7.38 \cdot 10^{-3}$	$2.04 \cdot 10^{-4}$	$8.2 \cdot 10^{-3}$	$4.39 \cdot 10^{-2}$	$1.87 \cdot 10^{-2}$	$2.65 \cdot 10^{-3}$	$1.12 \cdot 10^{-3}$
$\beta[^\circ]$	$2.0 \cdot 10^{-2}$	$5.61 \cdot 10^{-4}$	$2.25 \cdot 10^{-2}$	$1.2 \cdot 10^{-1}$	$5.13 \cdot 10^{-2}$	$7.3 \cdot 10^{-3}$	$3.07 \cdot 10^{-3}$

Table 5.1: Torque Set Point = 20%, low K_P

Variable	X(5 Hz)	X(50 Hz)	X(60 Hz)	X(300 Hz)	X(360 Hz)	X(600 Hz)	X(720 Hz)
AGT[pu]	$1.04 \cdot 10^{-3}$	$7.0 \cdot 10^{-5}$	$7.54 \cdot 10^{-3}$	$7.14 \cdot 10^{-5}$	$3.77 \cdot 10^{-5}$	$1.20 \cdot 10^{-2}$	$3.11 \cdot 10^{-2}$
I_{DC}[pu]	$4.32 \cdot 10^{-4}$	$3.14 \cdot 10^{-5}$	$2.27 \cdot 10^{-3}$	$5.62 \cdot 10^{-2}$	$3.45 \cdot 10^{-2}$	$1.36 \cdot 10^{-2}$	$8.19 \cdot 10^{-3}$
$\alpha[^\circ]$	$1.25 \cdot 10^{-2}$	$8.59 \cdot 10^{-4}$	$6.12 \cdot 10^{-2}$	$1.76 \cdot 10^{-1}$	$7.52 \cdot 10^{-2}$	$1.06 \cdot 10^{-2}$	$4.46 \cdot 10^{-3}$
$\beta[^\circ]$	$8.44 \cdot 10^{-3}$	$5.88 \cdot 10^{-4}$	$4.19 \cdot 10^{-2}$	$1.2 \cdot 10^{-1}$	$5.15 \cdot 10^{-2}$	$7.31 \cdot 10^{-3}$	$3.07 \cdot 10^{-3}$

Table 5.2: Torque Set Point = 20%, medium K_P

As it is possible to see, by raising the K_P constant, the amplitude of the air-gap torque given by the motor at the frequency of the speed disturbance is reduced: the reason is that with the higher K_P, the PI controller will have a stricter control on the DC link current, thus better rejecting the speed disturbance. This results in a lower amplitude of the component at the frequency of the speed disturbance, both in the Air Gap Torque (that is strictly connected to the current entering the motor) and in the DC link current. The amplitude of the component of the rectifier firing angle α raises because this is the output quantity of the PI controller, thus raising the K_P constant leads to an higher output of the aforementioned controller.

The reduction in the component of the inverter firing angle β (-70.5%) is approximately equal to the reduction in the DC link current (-70.4%). This is due to the fact that the β angle is controlled using the filtered DC link current, and the bandwidth of the filter is higher than the frequency of the speed disturbance.

The comments that have been made on the effect of the change of K_P with a Torque Set Point equal to the 20% of the rated torque still apply when TSP is equal to 100%; the results are shoown in Table 5.8

It is possible to conclude that the results of the simulations confirm the expected

Variable	X(5 Hz)	X(50 Hz)	X(60 Hz)	X(300 Hz)	X(360 Hz)	X(600 Hz)	X(720 Hz)
AGT[pu]	$9.25 \cdot 10^{-4}$	$6.42 \cdot 10^{-5}$	$8.35 \cdot 10^{-3}$	$4.72 \cdot 10^{-5}$	$5.19 \cdot 10^{-5}$	$1.19 \cdot 10^{-2}$	$3.1 \cdot 10^{-2}$
I_{DC}[pu]	$3.03 \cdot 10^{-4}$	$1.1 \cdot 10^{-5}$	$2.93 \cdot 10^{-3}$	$5.56 \cdot 10^{-2}$	$3.46 \cdot 10^{-2}$	$1.34 \cdot 10^{-2}$	$8.16 \cdot 10^{-3}$
$\alpha[^\circ]$	$1.65 \cdot 10^{-2}$	$5.88 \cdot 10^{-4}$	$1.49 \cdot 10^{-1}$	$3.27 \cdot 10^{-1}$	$1.42 \cdot 10^{-1}$	$1.96 \cdot 10^{-2}$	$8.39 \cdot 10^{-3}$
$\beta[^\circ]$	$5.9 \cdot 10^{-3}$	$2.13 \cdot 10^{-4}$	$5.4 \cdot 10^{-2}$	$1.18 \cdot 10^{-1}$	$5.15 \cdot 10^{-2}$	$7.19 \cdot 10^{-3}$	$3.05 \cdot 10^{-3}$

Table 5.3: Torque Set Point = 20%, high K_P

Variable	ΔX[%]
AGT	-37.2
I_{DC}	-70.4
α	+124.
β	-70.5

Table 5.4: Variation in components at the frequency of the speed disturbance due to a raising of K_P, TSP = 20%

Variable	X(5 Hz)	X(50 Hz)	X(60 Hz)	X(300 Hz)	X(360 Hz)	X(600 Hz)	X(720 Hz)
AGT[pu]	$6.15 \cdot 10^{-3}$	$3.1 \cdot 10^{-4}$	$5.33 \cdot 10^{-3}$	$4.64 \cdot 10^{-5}$	$6.64 \cdot 10^{-5}$	$1.26 \cdot 10^{-2}$	$1.02 \cdot 10^{-1}$
I_{DC}[pu]	$3.41 \cdot 10^{-3}$	$7.46 \cdot 10^{-5}$	$8.65 \cdot 10^{-4}$	$4.71 \cdot 10^{-2}$	$2.41 \cdot 10^{-2}$	$1.12 \cdot 10^{-2}$	$5.46 \cdot 10^{-3}$
α[°]	$2.98 \cdot 10^{-2}$	$6.24 \cdot 10^{-4}$	$7.06 \cdot 10^{-3}$	$4.45 \cdot 10^{-2}$	$1.59 \cdot 10^{-2}$	$2.65 \cdot 10^{-3}$	$8.97 \cdot 10^{-4}$
β[°]	$2.55 \cdot 10^{-3}$	$3.85 \cdot 10^{-3}$	$1.57 \cdot 10^{-2}$	$7.13 \cdot 10^{-3}$	$8.89 \cdot 10^{-3}$	$2.58 \cdot 10^{-2}$	$2.69 \cdot 10^{-3}$

Table 5.5: Torque Set Point = 100%, low K_P

Variable	X(5 Hz)	X(50 Hz)	X(60 Hz)	X(300 Hz)	X(360 Hz)	X(600 Hz)	X(720 Hz)
AGT[pu]	$3.67 \cdot 10^{-3}$	$2.7 \cdot 10^{-4}$	$5.48 \cdot 10^{-3}$	$2.22 \cdot 10^{-5}$	$8.18 \cdot 10^{-5}$	$1.27 \cdot 10^{-2}$	$1.03 \cdot 10^{-1}$
I_{DC}[pu]	$5.59 \cdot 10^{-4}$	$2.51 \cdot 10^{-5}$	$8.49 \cdot 10^{-4}$	$4.7 \cdot 10^{-2}$	$2.4 \cdot 10^{-2}$	$1.12 \cdot 10^{-2}$	$5.39 \cdot 10^{-3}$
α[°]	$3.61 \cdot 10^{-2}$	$8.59 \cdot 10^{-4}$	$2.79 \cdot 10^{-2}$	$1.77 \cdot 10^{-1}$	$6.31 \cdot 10^{-2}$	$1.04 \cdot 10^{-2}$	$3.55 \cdot 10^{-3}$
β[°]	$9.97 \cdot 10^{-4}$	$1.36 \cdot 10^{-4}$	$2.16 \cdot 10^{-2}$	$4.81 \cdot 10^{-3}$	$1.11 \cdot 10^{-2}$	$3.49 \cdot 10^{-2}$	$1.51 \cdot 10^{-3}$

Table 5.6: Torque Set Point = 100%, medium K_P

Variable	X(5 Hz)	X(50 Hz)	X(60 Hz)	X(300 Hz)	X(360 Hz)	X(600 Hz)	X(720 Hz)
AGT[pu]	$3.62 \cdot 10^{-3}$	$3.51 \cdot 10^{-4}$	$4.89 \cdot 10^{-3}$	$1.17 \cdot 10^{-4}$	$7.34 \cdot 10^{-5}$	$1.18 \cdot 10^{-2}$	$1.02 \cdot 10^{-1}$
I_{DC}[pu]	$5.50 \cdot 10^{-4}$	$9.21 \cdot 10^{-5}$	$9.94 \cdot 10^{-4}$	$4.36 \cdot 10^{-2}$	$2.4 \cdot 10^{-2}$	$1.03 \cdot 10^{-2}$	$5.38 \cdot 10^{-3}$
α[°]	$3.92 \cdot 10^{-2}$	$6.2 \cdot 10^{-3}$	$6.73 \cdot 10^{-2}$	$3.35 \cdot 10^{-1}$	$1.29 \cdot 10^{-1}$	$1.94 \cdot 10^{-2}$	$7.23 \cdot 10^{-3}$
β[°]	$4.92 \cdot 10^{-4}$	$1.09 \cdot 10^{-4}$	$2.2 \cdot 10^{-2}$	$3.68 \cdot 10^{-3}$	$1.25 \cdot 10^{-2}$	$3.15 \cdot 10^{-2}$	$1.80 \cdot 10^{-3}$

Table 5.7: Torque Set Point = 100%, high K_P

Variable	ΔX[%]
AGT	-41.2
I_{DC}	-83.9
α	+31.7
β	-80.7

Table 5.8: Variation in components at the frequency of the speed disturbance due to a raising of K_P, TSP = 100%

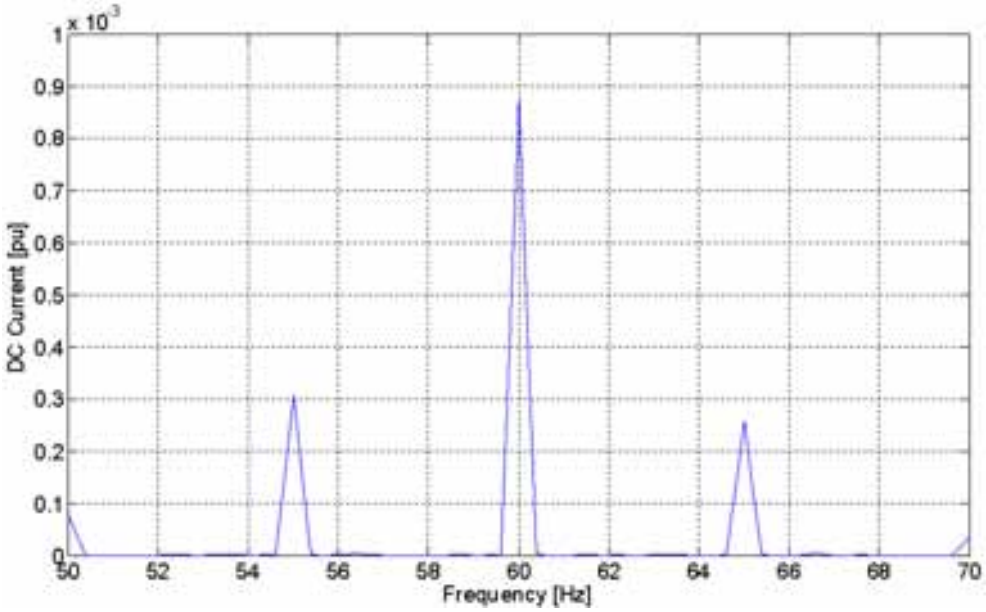

Figure 5.1: Side components due to speed disturbance.

trends for the analyzed system; in the next section a comparison between the measured quantities and the simulation results will be presented.

For completeness, it is important to remark that the speed disturbance at a certain frequency results not only in current component at the same frequency, but also in other side components around the most important components in output from the VSD. For instance, in this case, the speed disturbance at 5 Hz produces current components at 50 ± 5 Hz, 60 ± 5 Hz, and for all the other components listed in the preceding tables. Fig. 5.1 shows the side components at 720 ± 5 Hz.

5.3 Simulation Results: comparison with test measurements

In this section, the results obtained using the simulation model are compared with the measurements obtained during the string test.

The first subsection presents a comparison of the Air Gap Torque between simulation model and measurements in conditions with a constant Torque Set Point; the second subsection refers to conditions in which the Torque Set Point is varied over time. Lastly, a comparison between simulated and measured cyclic torques on machines' couplings is presented.

5.3.1 Constant Torque Set Point

In this subsection, the results of a comparison with constant TSP are shown. The comparison shows the Air Gap Torque, because it represents the most important quantity to be reproduced by the simulation model. The comparison also includes the phase currents entering the motor and the phase to phase voltages, because these are the quantities from which the Air Gap Torque is calculated.

The phase currents are normalized considering the 0-peak amplitude of the fundamental harmonic of the stator current, that is $\sqrt{2}I_s$, where I_s is calculated as in Eq. 4.15, by imposing that I_{DC} assumes its nominal value. The phase to phase voltage is normalized by dividing the amplitude of each component by the nominal 0-peak phase to phase voltage of the machine.

The comparison has been conducted with two different Torque Set Points (20% and 100%); the K_P constant assumes a medium value. The error is calculated as in Eq 5.2.

$$Error \ = \frac{X(Simulation) - X(Measurement)}{X(Measurement)} \tag{5.2}$$

	X(50 Hz)	X(60 Hz)	X(300 Hz)	X(360 Hz)	X(600 Hz)	X(720 Hz)
Simulation	$7.07 \cdot 10^{-5}$	$7.73 \cdot 10^{-3}$	$5.65 \cdot 10^{-5}$	$1.42 \cdot 10^{-4}$	$1.2 \cdot 10^{-2}$	$3.1 \cdot 10^{-2}$
Measurement	$1.16 \cdot 10^{-4}$	$5.16 \cdot 10^{-3}$	$8.38 \cdot 10^{-4}$	$2.32 \cdot 10^{-3}$	$4.95 \cdot 10^{-3}$	$2.46 \cdot 10^{-2}$
Error [%]	-39.0	49.8	-93.3	-93.9	141.	26.0

Table 5.9: FFT of Air Gap Torque: TSP = 20%

	X(50 Hz)	X(60 Hz)	X(300 Hz)	X(360 Hz)	X(600 Hz)	X(720 Hz)
Simulation [pu]	$3.29 \cdot 10^{-4}$	$5.26 \cdot 10^{-3}$	$9.86 \cdot 10^{-5}$	$1.63 \cdot 10^{-4}$	$1.24 \cdot 10^{-2}$	$1.03 \cdot 10^{-1}$
Measurement [pu]	$3.37 \cdot 10^{-4}$	$4.9 \cdot 10^{-3}$	$1.5 \cdot 10^{-3}$	$8.64 \cdot 10^{-3}$	$6.33 \cdot 10^{-3}$	$6.28 \cdot 10^{-2}$
Error [%]	-2.60	7.27	-93.4	-98.1	96.	63.4

Table 5.10: FFT of Air Gap Torque: TSP = 100%

Let us firstly consider the error on the Air Gap Torque components, that is shown in Tables 5.9 and 5.10. As it is possible to see, the error on the components at $50Hz$ and $60Hz$ is very low for TSP = 100%, while is higher for TSP = 20%, but the order of magnitude is still correct.

However, the $300Hz$ and $360Hz$ are strongly underestimated by the simulation model, but this is not a big issue, because these components are very low for this 6-phase motor. The error on the $600Hz$ and $720Hz$ components is quite high (in particular the simulation model predicts a $600Hz$ component that is twice the measured one), but these are the

harmonic components with the highest amplitude for the real motor, thus it is better not to underestimate them.

As a matter of fact, if this motor would be operated as a starter (that means that the motor is applying torque on the shaft line during the starting sequence), the $6 \cdot f_m$ component could coincide with one of the lowest TNFs, thus exciting it. So, it is very important not to underestimate this component, in order to have a conservative design of the shaft line in such a system. In this case this is only an hypothesis because in this system the motor works only in a narrow speed range around the rated speed.

Tables 5.11 and 5.12 show the FFTs of simulated and measured phase currents entering the electrical motor, while 5.13 and 5.14 show the FFTs of phase to phase voltages for the electrical motor. These quantities are very important because they represent the inputs of the algorithm that calculates the Air Gap Torque of the electrical motor, thus it is possible to understand the reason of the errors in AGT components.

It is important to recall that the 6 phase motor is described as two three phase motors fed by two six pulse systems, thus for voltages and currents, the 6-pulse components, such as $300Hz$ and $360Hz$ are predominant if compared with the $600Hz$ and $720Hz$ components.

The motor is running at rated speed (3600 rpm = 60 Hz) thus the highest component for phase currents and voltages is that at 60 Hz.

As it is possible to note by examining Tables 5.11 and 5.12, the simulation model usually overestimate all the current components, except the component at 50 Hz, that however is always the lowest one. Figure 5.2 represents the simulated and measured phase current with TSP = 100%.

Tables 5.13 and 5.14 show the FFTs of phase to phase voltages. As it is possible to note, the error on the 60 Hz component is very low, but the error on all the other components is always 100%, considering numbers with three significan digits, because the simulation model strongly underestimates all these components.

The reason can be easily seen by analyzing Fig 5.3: the phase voltage, in the simulation model, is constructed as a sinusoid, which amplitude and frequency can change when the running speed changes. However in the real phase to phase voltage it is possible to observe other components due to the sudden change in phase currents during commutations: the absence of the description of this phenomenon in the simulation model results in a very strong error on the description of phase to phase voltage.

However, it is important to say that the most important output of the simulation model is the Air Gap Torque, because it is the only quantity that affects the torsional dynamics of the whole system, and in the previous paragraphs it has been shown that the description of the AGT can be considered satisfactory for the verification of the torsional design of the shaft line, because the highest components of the real AGT are always

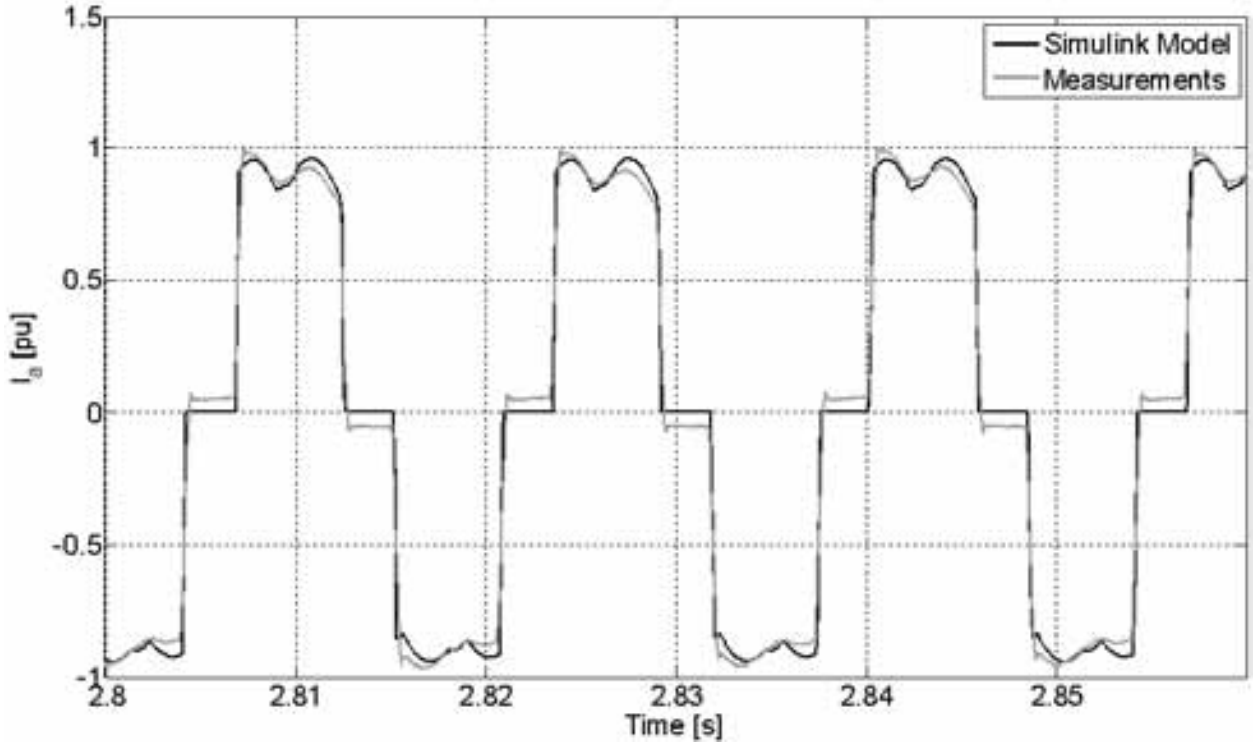

Figure 5.2: Phase Current, TSP = 100%

overestimated by the simulation model, thus resulting in a conservative design.

	X(50 Hz)	X(60 Hz)	X(300 Hz)	X(360 Hz)	X(600 Hz)	X(720 Hz)
Simulation	$2.07 \cdot 10^{-5}$	$2.46 \cdot 10^{-1}$	$6.68 \cdot 10^{-2}$	$3.05 \cdot 10^{-2}$	$6.02 \cdot 10^{-3}$	$5.79 \cdot 10^{-3}$
Measurement	$1.28 \cdot 10^{-4}$	$3.18 \cdot 10^{-1}$	$7.4 \cdot 10^{-2}$	$2.5 \cdot 10^{-2}$	$5.39 \cdot 10^{-3}$	$3.4 \cdot 10^{-3}$
Error [%]	-83.8	-22.6	-9.75	22.0	11.9	70.2

Table 5.11: FFT of Phase Current: TSP = 20%

5.3.2 Change in Torque Set Point

A second comparison has been conducted considering two situations in which the TSP of the electrical motor is changed by the speed governor: firstly, a change in TSP from 100% to 85% is analyzed, with the K_P constant assuming a medium value; then a situation in which TSP is changed from 20% to 10% is considered, with the K_P constant assuming an high value.

These conditions allow to compare the behavior of the model with the physical system, in dynamic conditions. The scale in all figures that show angles is omitted because of intellectual property reasons; however in each figure there is an information that allows to understand the amplitude of variations in these quantities.

	X(50 Hz)	X(60 Hz)	X(300 Hz)	X(360 Hz)	X(600 Hz)	X(720 Hz)
Simulation	$3.05 \cdot 10^{-5}$	1.	$2.1 \cdot 10^{-1}$	$2.45 \cdot 10^{-2}$	$5.13 \cdot 10^{-3}$	$4.47 \cdot 10^{-3}$
Measurement	$5.16 \cdot 10^{-5}$	0.997	$17.9 \cdot 10^{-1}$	$1.53 \cdot 10^{-2}$	$2.73 \cdot 10^{-3}$	$1.91 \cdot 10^{-3}$
Error [%]	-40.9	0.44	17.4	60.2	87.6	134.

Table 5.12: FFT of Phase Current: TSP = 100%

	X(50 Hz)	X(60 Hz)	X(300 Hz)	X(360 Hz)	X(600 Hz)	X(720 Hz)
Simulation	$6.15 \cdot 10^{-8}$	1.	$4.94 \cdot 10^{-8}$	$1.47 \cdot 10^{-8}$	$3.34 \cdot 10^{-7}$	$3.99 \cdot 10^{-7}$
Measurement	$6.25 \cdot 10^{-4}$	1.14	$3.52 \cdot 10^{-2}$	$6.59 \cdot 10^{-3}$	$4.27 \cdot 10^{-3}$	$3.51 \cdot 10^{-3}$
Error [%]	-100.	-12.1	-100.	-100.	-100.	-100.

Table 5.13: FFT of Phase to Phase Voltage: TSP = 20%

	X(50 Hz)	X(60 Hz)	X(300 Hz)	X(360 Hz)	X(600 Hz)	X(720 Hz)
Simulation	$3.37 \cdot 10^{-8}$	1.	$1.81 \cdot 10^{-8}$	$2.42 \cdot 10^{-9}$	$2.45 \cdot 10^{-7}$	$3.03 \cdot 10^{-7}$
Measurement	$8.98 \cdot 10^{-5}$	0.989	$7.42 \cdot 10^{-2}$	$4.29 \cdot 10^{-3}$	$2.39 \cdot 10^{-3}$	$1.98 \cdot 10^{-3}$
Error [%]	-100.	1.08	-100.	-100.	-100.	-100.

Table 5.14: FFT of Phase to Phase Voltage: TSP = 100%

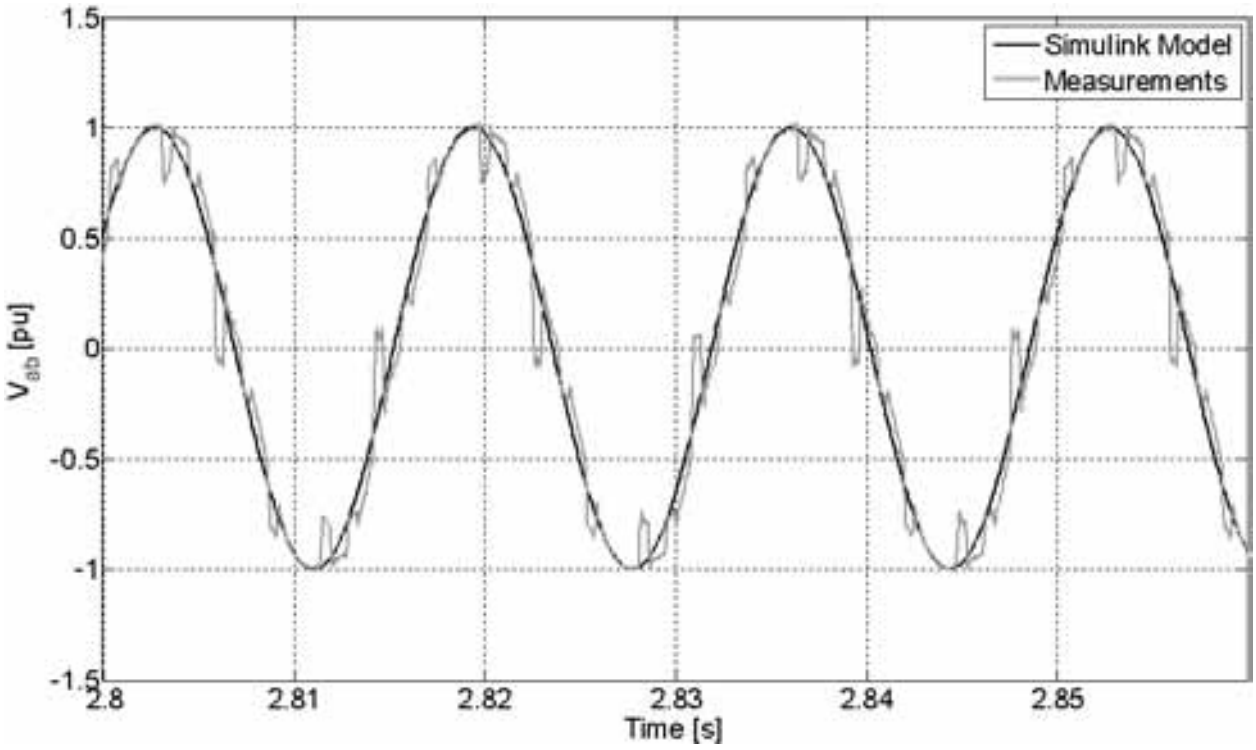

Figure 5.3: Phase to phase voltage, TSP = 100%

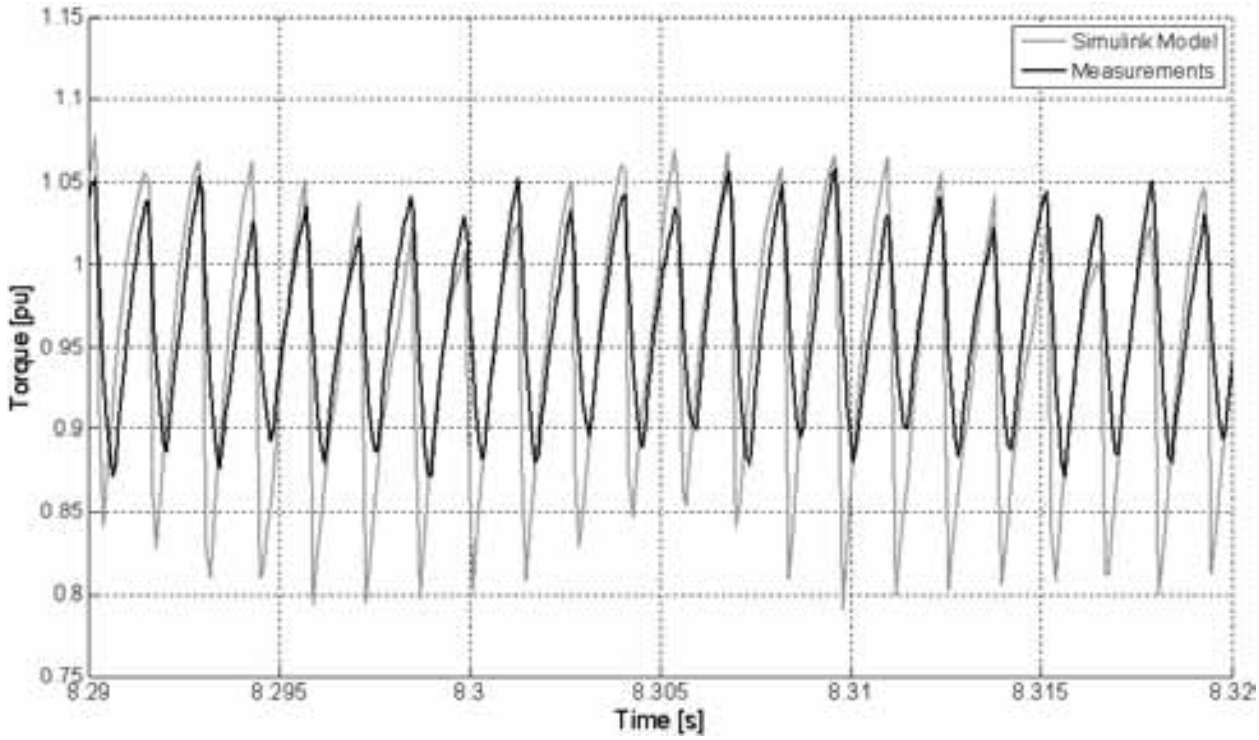

Figure 5.4: Air Gap Torque vs Time, TSP = 100%, medium K_P

5.3.2.1 TSP from 100% to 85%, medium K_P

In the first condition that has been analyzed, the TSP changes from 100% to 85%, with the K_P constant assuming a medium value. The results are presented using time plots of the most significant quantities.

Firstly, Fig. 5.4 shows the simulated and measured Air Gap Torque when the Torque Set Point is still constant at 100%; as it is possible to see, the simulated Air Gap Torque has an higher amplitude ripple than the real torque; this is coherent with the FFTs shown in the previous subsection, that confirm that the simulated torque has higher amplitude components at the most significant frequencies.

A quite good accordance can be seen for steady state DC link current, shown in Fig. 5.5. Then, Fig. 5.6 shows the DC link current when the Torque Set Point changes from 100% to 85%; The most important feature to be observed is that, after the change in TSP, the simulated DC link current seems to reach an higher average value rather than the measured current. By observing Fig. 5.7, that shows a longer time window, it is possible to see that the simulated DC link current reaches the new correct average value after half a second, so it is far slower than the real system.

This is confirmed by observing the rectifier firing angle, shown in Fig. 5.8: as it is possible to see, when the Torque set point is reduced, the firing angle raises in order to reduce the DC link current, because the average output voltage from the rectifier bridge

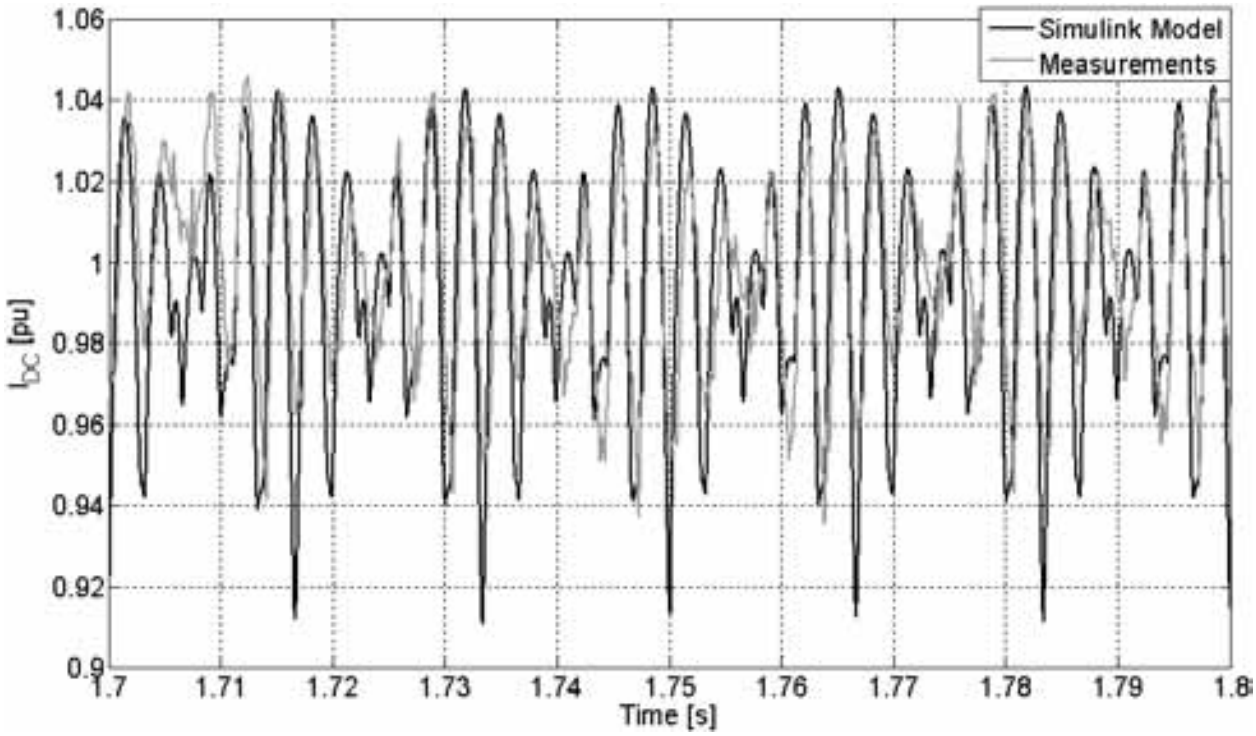

Figure 5.5: DC link current vs Time, TSP = 100%, medium K_P

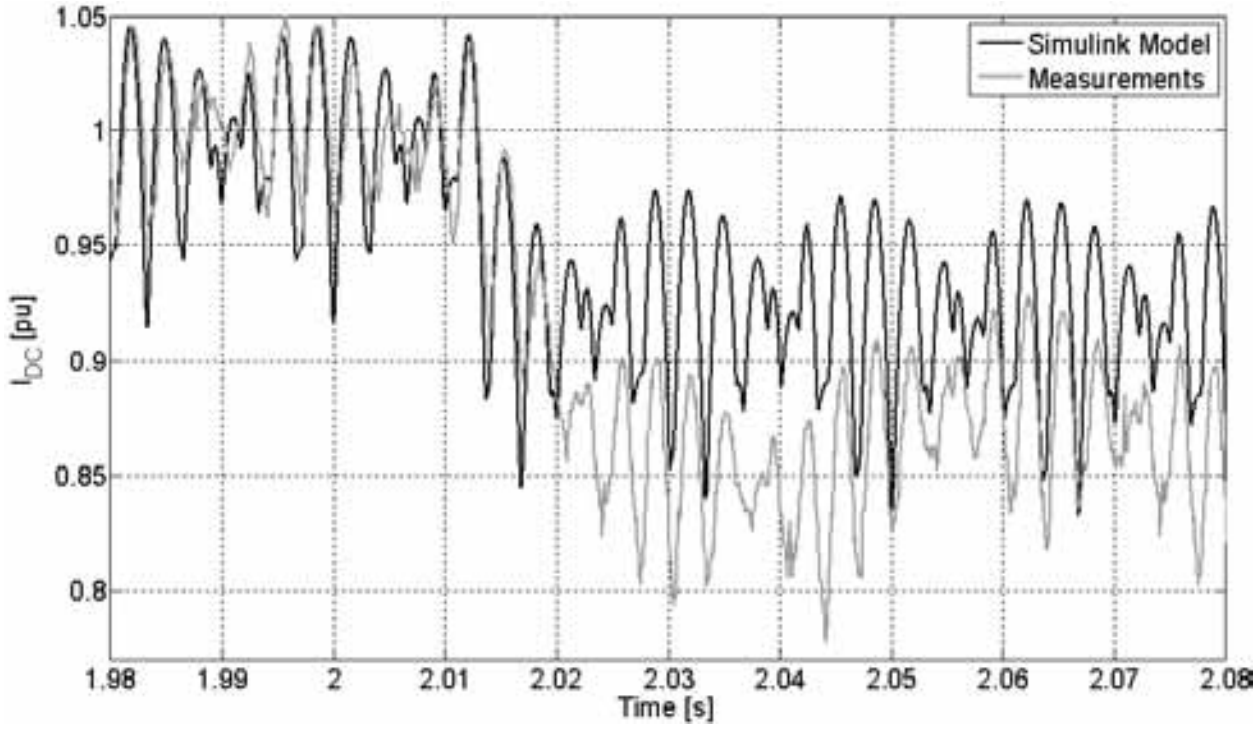

Figure 5.6: DC link current vs Time, TSP from 100% to 85%, medium K_P

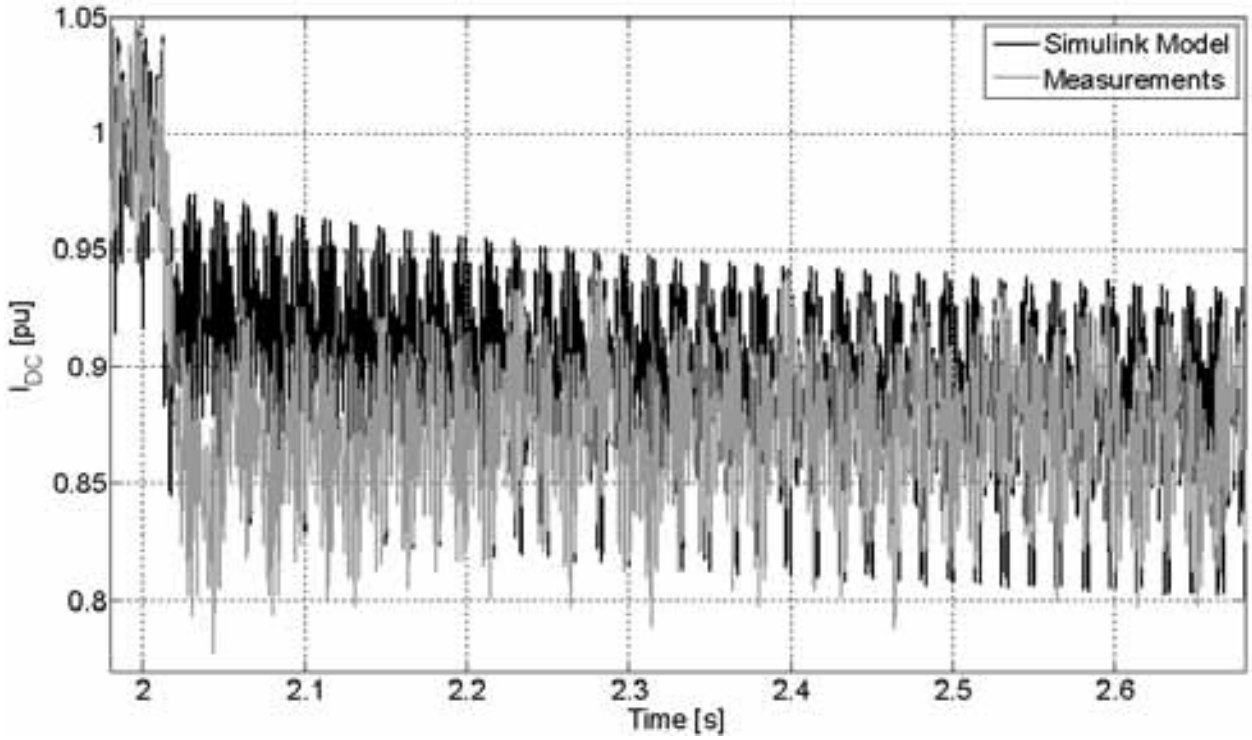

Figure 5.7: DC link current vs Time, TSP from 100% to 85%, medium K_P

is proportional to the cosine of the rectifier firing angle. In the real system, the rectifier firing angle has a peak after 2 seconds that is wider than in the simulation model. This allows for a faster reduction in the DC link current, confirming the behavior for the DC link current shown in Fig. 5.7. Note that the rectifier firing angle is a quantized quantity in measurements, thus its pattern seems far different from that of the simulation model. This is only due to the measurement system of this quantity, that is described with a very low number of bits; the vendor of the electrical drive confirmed that inside the control system this quantity is described with an higher precision. The same consideration on the measurement system applies also to the inverter firing angle, as it will be shown in the next paragraphs.

Fig. 5.9 shows the inverter firing angle: firstly it must be noted that the low precision in the measurement does not allow to clearly understand the real dynamics of this quantity; additionally, when TSP is still 100% the measured angle is always higher than the value β_{lim} that is the maximum value of the firing angle that canbe calculated in output by the look-up table implemented in the control system. The measurement system probably has an offset, thus the real values assumed by this angle can be obtained by shifting down the measured values, by subtracting about $1 \div 1.5\,^{\circ}$. The decrease in the inverter firing angle after the change in TSP is due to the look-up table implemented in the control system. The maximum value for the simulated β angle is β_{lim}, as it can be noted in Fig. 5.9.

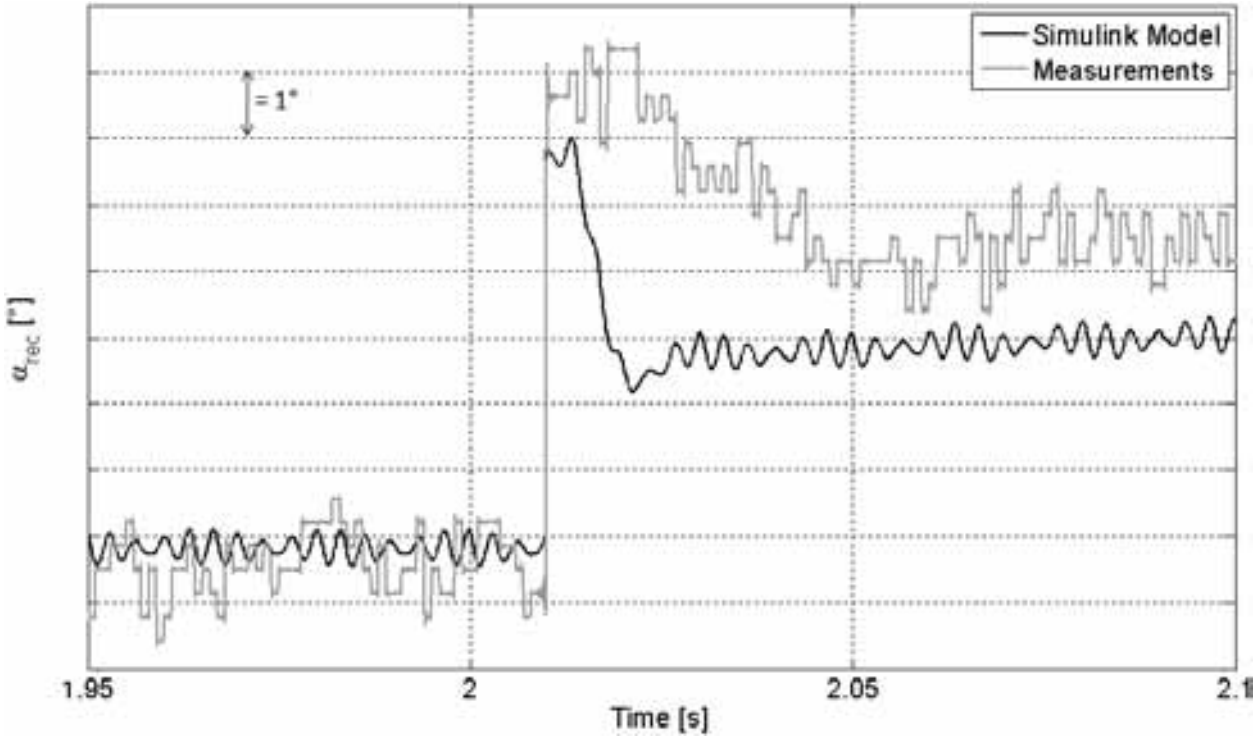

Figure 5.8: Rectifier firing angle vs Time, TSP from 100% to 85%, medium K_P

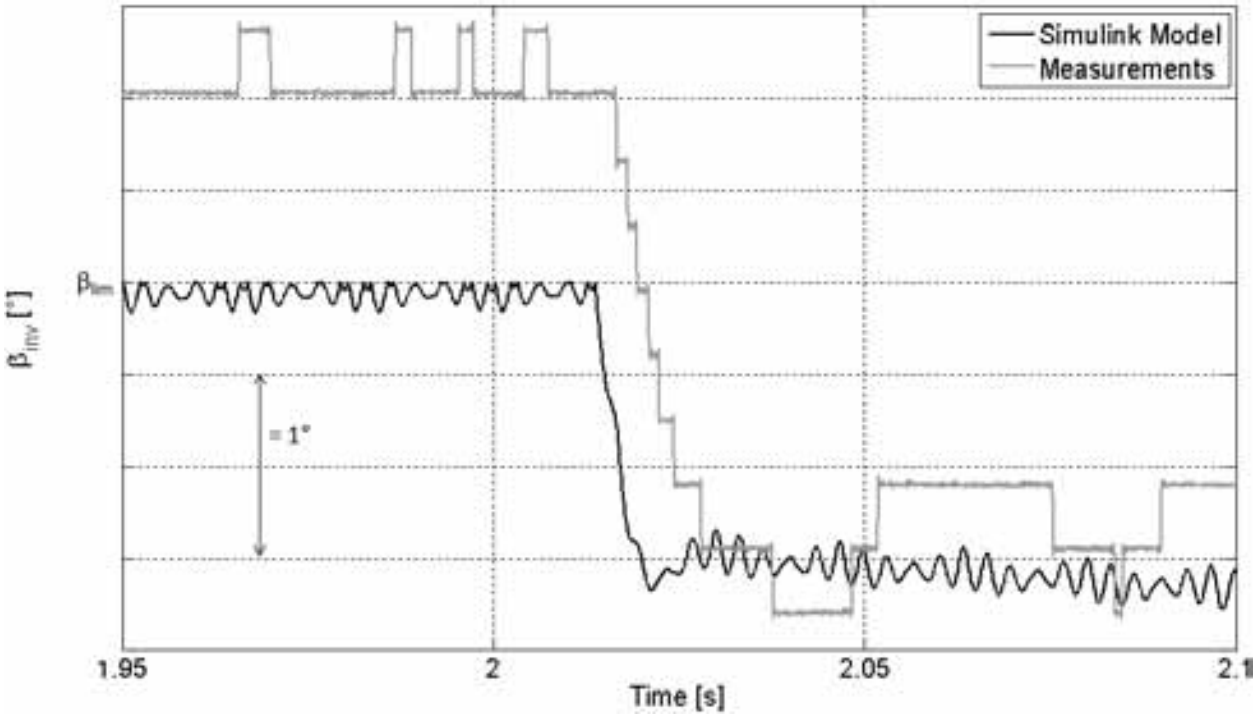

Figure 5.9: Inverter firing angle vs Time, TSP from 100% to 85%, medium K_P

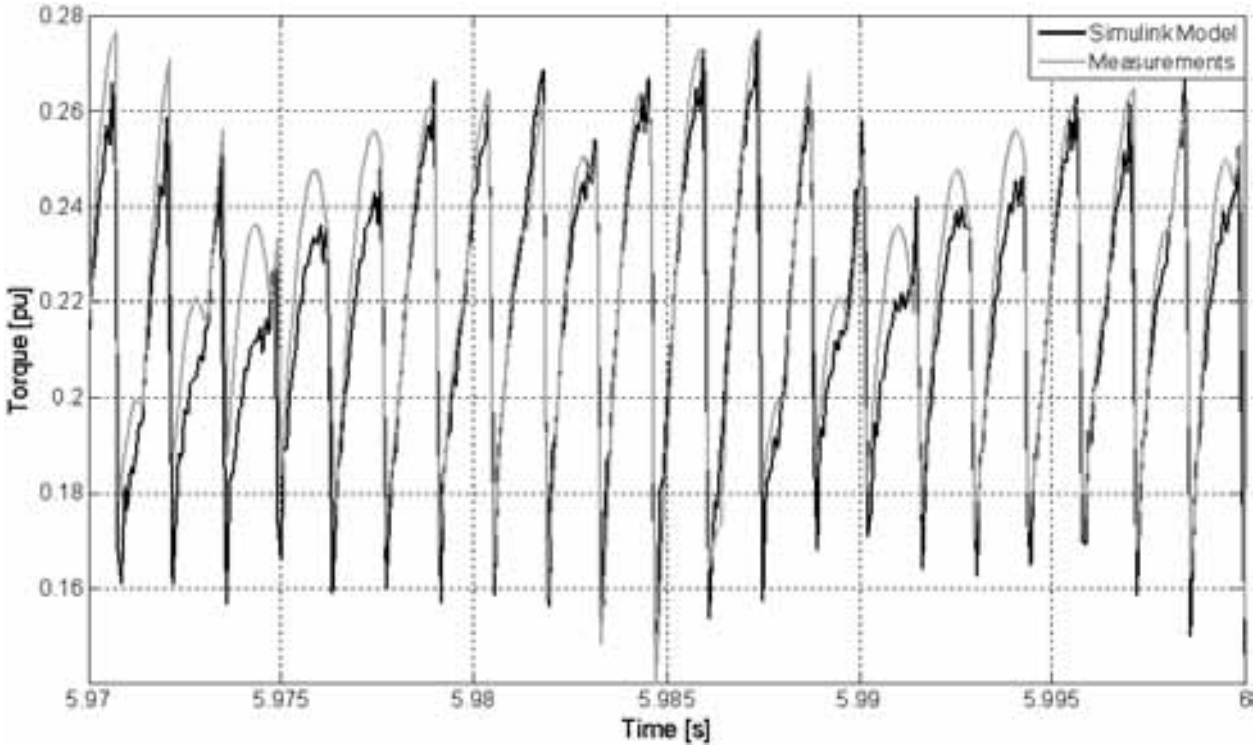

Figure 5.10: Air Gap Torque vs Time, TSP = 20%, high K_P

5.3.2.2 TSP from 20% to 10%, high K_P

In the second condition that has been analyzed, the TSP changes from 20% to 10%, with the K_P constant assuming an high value. The results are presented using time plots of the most significant quantities. Firstly, Fig. 5.10 shows the simulated and measured Air Gap Torque when the Torque Set Point is still constant at 20%; as it is possible to see, there is a good accordance between simulation and measurements. The same comment can be made for the DC link current, shown in Fig. 5.11.

Then, Fig. 5.12 shows the DC link current when the Torque Set Point changes from 20% to 10%; firstly it is possible to note that there is not a perfect syncronization in the change in TSP between simulation model and physical system, because the DC link current reduces in the *Simulink*^{TM} model before that in the measurements, but this is only due to the difficulties in having a perfectly synchronized change in TSP.

Also in this case, as it has been shown in the previous subsection, the simulated current takes a longer time to reach the new average value, but the difference from the measurements is very limited in this case.

Fig. 5.13 shows the rectifier firing angle vs time: there is a good accordance between simulation and measurements, but also in this case it can be seen that the peak in the measured quantity is wider than in simulation. The same considerations, that have been made in the previous subsection, on the precision of the measurement apply.

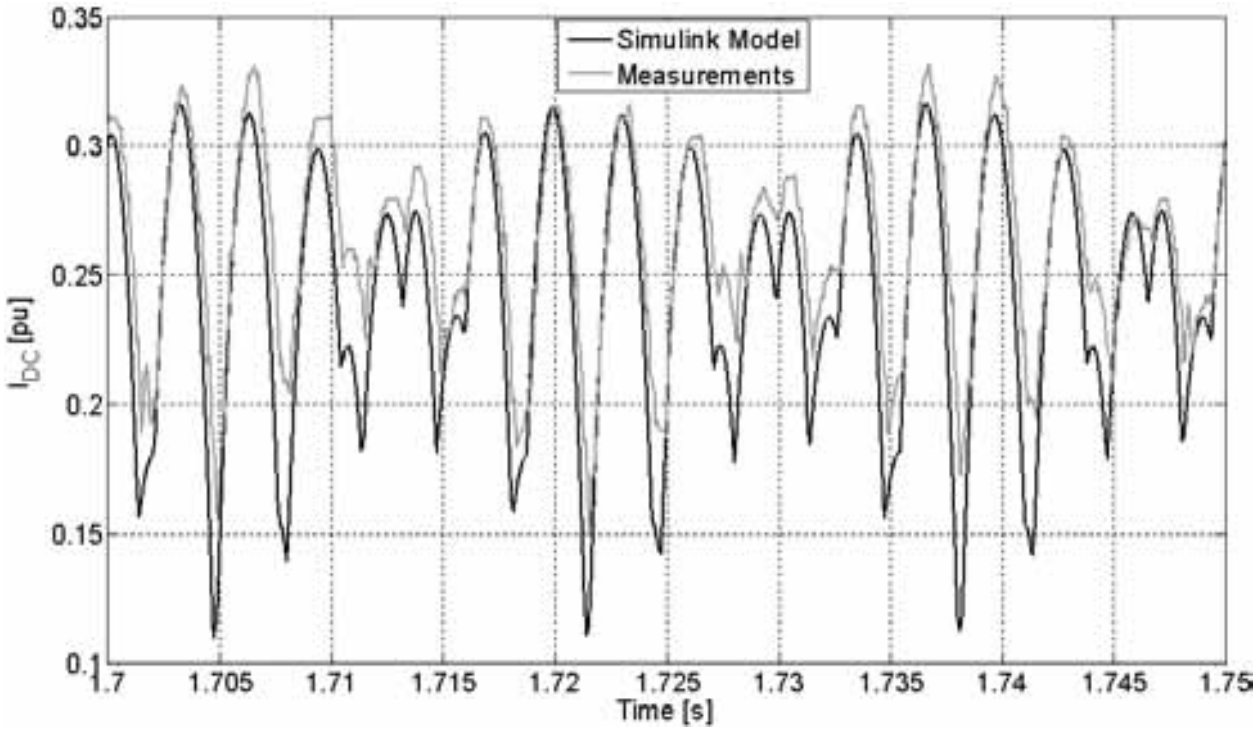

Figure 5.11: DC link current vs Time, TSP = 20%, high K_P

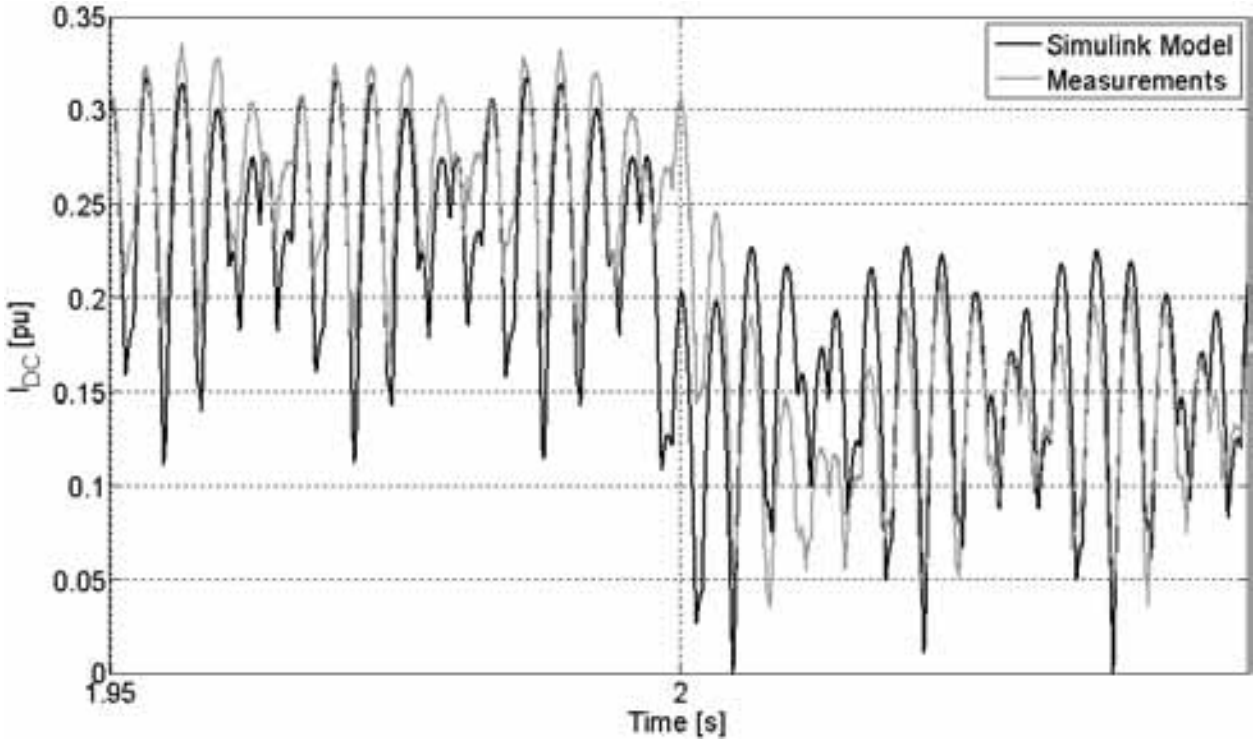

Figure 5.12: DC link current vs Time, TSP from 20% to 10%, high K_P

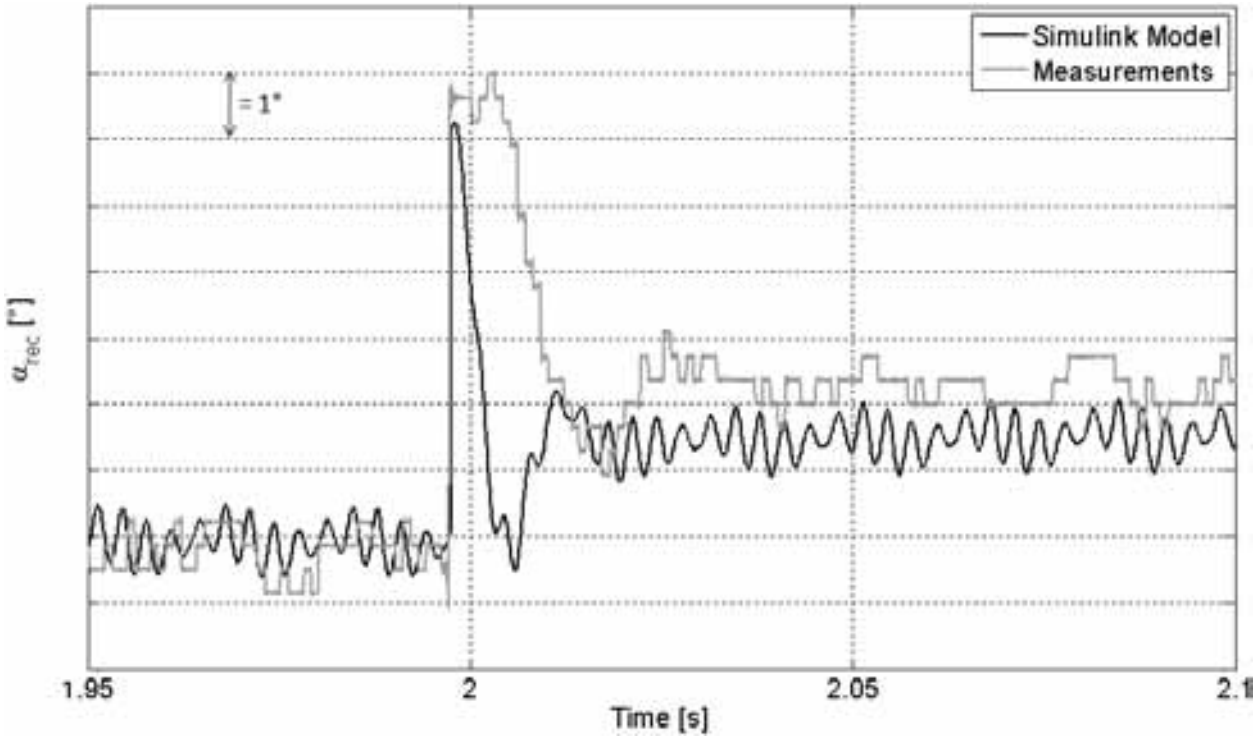

Figure 5.13: Rectifier firing angle vs Time, TSP from 20% to 10%, high K_P

By observing Fig. 5.14, it is possible to note that by subtracting about $1 \div 1.5\,^{\circ}$ to the measured quantity, as it has been suggested in the previous subsection, a good accordance can be found between simulations and measurements.

5.3.3 Cyclic Torques on Couplings

The previous subsections has presented a comparison between simulation and measurements for all the electrical quantities, in order to understand the performances of the electrical model that has been developed to describe the dynamics of the electrical drive. However, an important goal of the research activity, is to correctly predict the cyclic torques acting on the shaft line, in order to evaluate with the simulation model the fatigue life of the shafts and couplings, as it has been described in the *Goodman Diagram* section, in Chapter 2.

The compression string has been instrumented in order to measure the cyclic torques acting on two couplings, as it has been described in the *Data Acquisition System* section in this chapter.

Firstly, it will be shown the comparison between simulated and measured cyclic torques acting on the electrical motor drive end coupling. In this coupling, two different measurement systems have been installed: both a strain gauge system and a phase shift system have been implemented. The different measurement system gave approximately the same

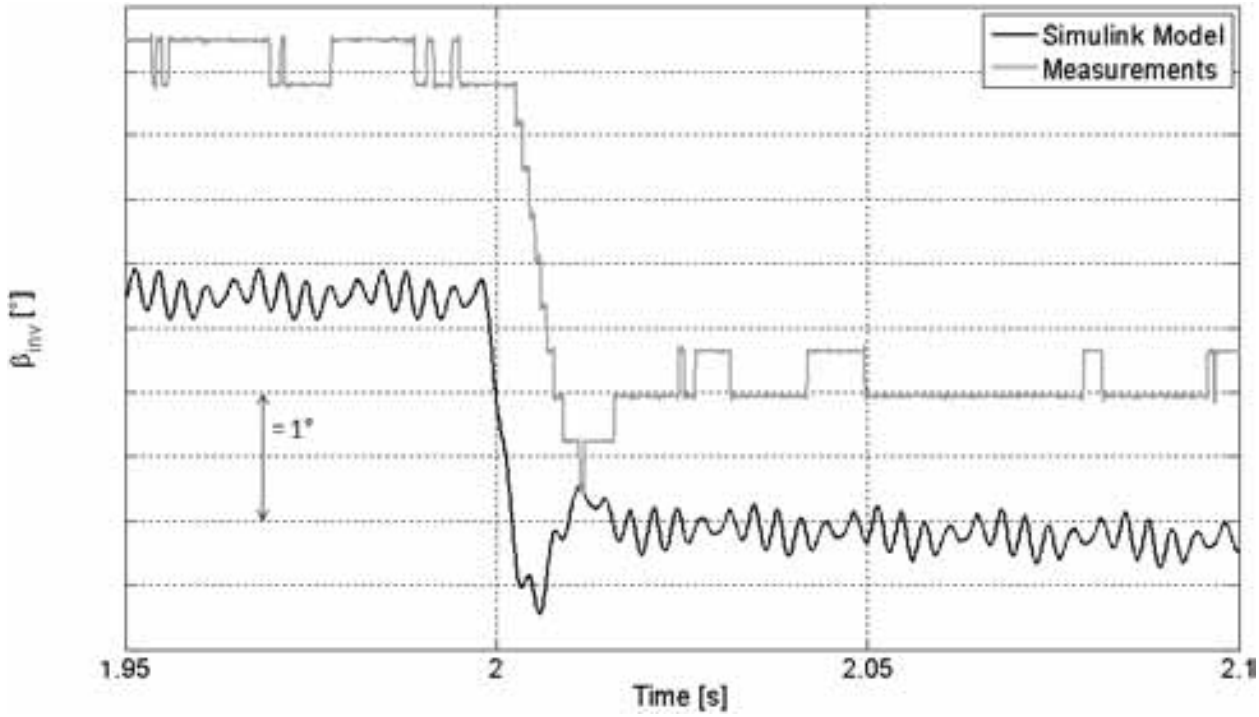

Figure 5.14: Inverter firing angle vs Time, TSP from 20% to 10%, high K_P

results; so, for the sake of brevity, the comparison between simulation and measurements is conducted only considering the strain gauge measure, because it is considered the most accurate method.

Table 5.15 shows the FFT of the simulated and measured torque, considering the components at the Torsional Natural Frequencies of the compression string, because these are the components with higher amplitude. The cyclic torques are scaled by the rated torque of the electrical motor. The comparison refers to a condition in which the motor Torque Set Point is 20% and the K_P constant of the current regulator has been set to a medium value.

	$X(1^{st}\,TNF)$	$X(2^{nd}\,TNF)$	$X(3^{rd}\,TNF)$	$X(4^{th}\,TNF)$
Simulation [pu]	$4.69 \cdot 10^{-3}$	$2.98 \cdot 10^{-3}$	$3.0 \cdot 10^{-3}$	$1.26 \cdot 10^{-3}$
Measurement [pu]	$5.36 \cdot 10^{-3}$	$3.46 \cdot 10^{-2}$	$3.33 \cdot 10^{-2}$	$5.06 \cdot 10^{-2}$
Error [%]	-12.5	-91.4	-91.	-97.5

Table 5.15: FFT of Torque on Motor Drive End Coupling, TSP = 20%, medium K_P

Table 5.16 shows the same comparison conducted on the coupling on the drive end side of the gas turbine shaft. In this case, the measurement has been conducted with a phase shift method that is designed to operate also at the installation site.

Firstly, it is important to remark that the amplitude of the measured cyclic torques is very low if compared with the capability of the couplings, thus it is possible to conclude

	$X(1^{st}\,TNF)$	$X(2^{nd}\,TNF)$	$X(3^{rd}\,TNF)$	$X(4^{th}\,TNF)$
Simulation [pu]	$5.\cdot 10^{-2}$	$1.5\cdot 10^{-1}$	$4.16\cdot 10^{-2}$	$2.22\cdot 10^{-1}$
Measurement [pu]	$3.39\cdot 10^{-2}$	$8.69\cdot 10^{-3}$	$8.95\cdot 10^{-4}$	$3.02\cdot 10^{-4}$
Error [%]	-32.2	-94.2	-97.8	-99.9

Table 5.16: FFT of Torque on Gas Turbine Drive End Coupling, TSP = 20%, medium K_P

that the torsional design of the shaft line, including the electrical drive, is satisfactory, and no concern is raised about the fatigue life of the couplings. If a Load Cycle is defined, as it has been shown in the *Forced Response* section, by using the time history of the measured torques, it is possible to verify that the stress condition is inside the safe area.

What is common to both the comparisons, is that while the cyclic torque at the $1^{st}\,TNF$ is predicted with a limited error, the components at the other TNFs are almost absent in the simulation model, while in the real system, the amplitude of these components is close to the amplitude of that at the $1^{st}\,TNF$.

This difference, that has been shown for a particular TSP and value of the K_P constant, has been found also in other operating conditions.It must be noted that in the simulation model the only machine that can excite a TNF is the electrical motor, because the bandwidth of the gas turbine model is far lower than the TNFs, and the compressors' model behaves simply as a torsional damper. However, the torque applied by the real turbomachines has a wide frequency content, due to different aerodynamic phenomena and irregularities in combustion. So, while the torque applied by turbomachines in the simulation model is almost a continuous torque, the real machines apply a pulsating torque that can excite the torsional natural frequencies. That is why the measured torque components are higher than those obtained by the simulation model.

However, it is important to remember what has been observed in the later sections: the simulation model of the electrical motor usually overestimate the pulsating torques applied by the motor. So if we consider that the results of the simulation models refer to the excitations due to the electrical motor only, it is possible to infer that the exciting torques due to the electrical motor are low if compared with those due to the other turbomachines. This has been confirmed by analyzing the pulsating torques acting on couplings when the electrical motor is off: in the simulation model, the amplitude of cyclic torques is almost zero, while in the real system the amplitude of these components has the same order of magnitude of the time periods in which the motor Torque Set Point is different from zero.

This allows also to say that the design of the electrical motor is satisfactory, because the cyclic torques acting on couplings does not change noticeably when the electrical motor is started, thus it will not arise torsional issues. It is possible to conclude that the torsional design of the compression string is satisfactory.

Chapter 6

Conclusions and Next Steps

The present dissertation is a summary of the construction of a dynamic model devoted to describe the torsional dynamics of a compression string that includes a Variable Speed Drive. The aim of the activity is to build a simulation tool that allows to predict if the electrical motor could create problems for the strength and fatigue life of the shaft line.

The activity has been sponsored by GE-Nuovo Pignone, that currently designs, assembles and sells compression strings that includes Variable Speed Drives.

A dynamic model has been created inside the *MatLab/Simulink*^{TM} environment. Firstly, a model that describes the torsional vibrations of shafts has been created, considering the API standards for turbomachinery. Secondly, a model for the torque applied by the turbomachines has been implemented, considering the models that have been developed inside GE. Lastly, an electrical model for the Variable Speed Drive has been implemented, considering the information that GE could receive by VSDs' vendors.

The electrical and mechanical models have been integrated in a unique model, that describes the physical connection of electrical and mechanical dynamics. This allows to understand the effects of torsional vibrations on the Air Gap Torque in output from the electrical motor, and vice-versa, the effect of the motor torque on torsional vibrations.

The behavior of the closed-loop system has been analyzed in order to evaluate the reaction of the electrical motor to speed disturbances; results of simulations confirm the trends that could be predicted considering the theoretical background of VSDs.

The parameters inside the simulation model have been set in order to describe the behavior of a real compression string, that has been tested in the GE-Nuovo Pignone facility in Massa. The simulation model requires in input a limited set of data, that are always included in the VSD data sheet. The results obtained in simulation have been compared with the measurements that have been collected during the compression string tests.

The first comparison has been conducted considering the motor output torque in

steady state conditions, with a constant Torque Set Point for the electrical motor. The frequency content of the simulated and measured Air Gap Torque have been compared, showing that the simulation model is able to predict the frequency of torque harmonics, and can predict the amplitude of the highest amplitude components with a limited error. The simulation model is always conservative, if torsional vibrations are considered, because the torque ripple predicted by the model is always higher than the real ripple.

Then the comparison considered situations in which the Torque Set Point changes, showing that the dynamics of the simulation model are usually slower than the real system.

The last comparison has been conducted by analyzing the cyclic torques acting on couplings. The alternating torque calculated by the simulation model are far lower than those measured during the operation of the compression string, because the simulation model does not include any excitation given by the turbomachines, that, in this case, are preeminent if compared with those given by the electrical motor.

The outcome of the research activity is that the simulation model is able to describe the behavior of the Variable Speed Drive, confirming the satisfactory performances of the tested compression string.

However, there is an important drawback that must be specified: the simulation model does not include some secondary features that resulted as being critical for the vibrations induced by the VSD, as it has been demonstrated by the compression string tests and other tests conducted by GE in conjunction with the VSD vendor. Thus, using this model, it is not possible to analyze the influence on torsional dynamics of these secondary control loops, that must be adjusted using other techniques.

However, the simulation model can be used to adjust the control settings for the current regulator, before the testing and installation of the compression string, with the aim to reduce the pulsating torques on couplings for the real system. Thus, the simulation model can be useful for a virtual pre-tuning of the VSD system. By adjusting the value of a limited set of parameters, it is possible to adapt the simulation model to describe different drives with LCI architecture.

In order to have a more complete model, it would be important to describe also the dynamics of secondary control loops that are critical for the torsional interaction. However, it is very important to remark that these secondary features, as other additional features not included in the present model, are peculiar of the VSD vendors, which are not likely to transmit such proprietary informations to a client.

That is why the most important outcome of the research activity is the consciousness of the importance of a deep understanding of the phenomenon of the electro-mechanical interactions in the design phase of the compressor train, that can be achieved only through a strong synergy between train designers, components manufacturers and process and train owners.

The research activity, that has been supported inside GE both by the shaft line integrators (*Auxiliary System Engineering GEAR team*), by the electrical designers of the *Oil & Gas ENG PA EDES* and by the *Advanced Technology/Oil & Gas Technology Laboratory, Test Data Analysis (TDA)* team, created the basis for a deeper insight on the dynamics of the electro-mechanical systems, thus leading to a competitive advantage in the design of compression string that include Variable Speed Drive systems.

Bibliography

[1] R. Baccani, R. Zhang, T. Toma, A. Iuretig, M. Perna, Electric systems for high power compressor trains in oil and gas applications - system design, validation approach and performance, Proc. of 36th Annual Turbomachinery Symposium.

[2] M.A. Miranda, E.S. Brick, Life Cycle Cost Assessment of Turbomachinery for offshore applications, Proc. of 33rd Annual Turbomachinery Symposium.

[3] Krattiger, H.; Bondoni, C.; Kobi, H.; Remorini, H.D. , Increase competitive level by replacing steam turbines with electric adjustable speed drive system, Petroleum and Chemical Industry Technical Conference, 2004. Fifty-First Annual Conference 2004.

[4] Wikstrom, P.; Terens, L.A.; Kobi, H., Reliability, availability, and maintainability of high-power variable-speed drive systems, IEEE Transactions on Industry Applications, Volume 36, Issue 1, Jan.-Feb. 2000.

[5] A. Kocur, Jr., J.P. Corcoran, VFD Induced Coupling Failure, Case study of the 37th Annual Turbomachinery Symposium.

[6] T. Shimakawa, T. Kojo, The Torsional Torque Fluctuations of Compressor Train with Vector Control PWM Inverter, Case study of the 36th Annual Turbomachinery Symposium.

[7] V. Hutten, R. Zurowski, M. Hilscher, Torsional Interharmonic Interaction Study of 75 MW Direct-Driven VSDS Motor Compressor Trains for LNG Duty, Proceedings of the 37th Turbomachinery Symposium.

[8] M. Hernes, B. Gustavsen, Simulation of shaft vibrations due the interaction between generator-turbine train and power electronic converters at Visund platform, PCC 2002.

[9] M. A. Corbo, C. P. Cook, Torsional Vibration Analysis of Synchronous Motor-Driven Turbomachinery.

[10] M. A. Corbo, S. B. Malanosky, Practical Design against Torsional Vibration.

[11] M. Lalanne, G. Ferraris, Rotordynamics prediction in engineering, John Wiley & sons, 1990.

[12] API 671, Special-Purpose Couplings for Petroleum, Chemical, and Gas Industry Services

[13] API 684, Rotordynamic Tutorial: Lateral Critical Speeds, Unbalance Response, Stability, Train Torsionals and Rotor Balancing.

[14] H. N. Norton, Sensor and Analyzer Handbook, Prentice Hall, 1982.

[15] S. S. Gindy, Force and Torque Measurements, A Technology Overview Part Two - Torque, Wiley InterScience, Experimental Techniques, Volume 9, Issue 7.

[16] D. Walker, Torsional Vibration of Turbo-Machinery, USA, Mc Graw-Hill, 2003.

[17] API 617 Axial and Centrifugal Compressors and Expander compressors for Petroleum, Chemical and Gas Industry Services.

[18] D. N. Walker, S. L. Adams, R. J. Placek, Torsional Vibration and Fatigue of Turbine-Generator Shafts, IEEE Transactions on Power Apparatus and Systems, Vol. PAS-IOO, No. 11 November 1981.

[19] Peterson R.E. Stress Concentration Factors, published by Wiley and Sons New York.

[20] J. E. Shigley, Mechanical Engineering Design, ASME Transactions, Mc-Graw Hill Series in Mechanical Engineering.

[21] J. C. Wachel, F.R. Szenasi, Analysis of Torsional Vibrations in Rotating Machinery, Proceedings of the 22nd Turbomachinery Symposium.

[22] G. Genta, Vibration of Structures and Machines - Practical Aspects, Second Edition, Springer-Verlag.

[23] R. B. Randall, Frequency Analysis, Third Edition, Bruel & Kjaer, Naerum, Denmark.

[24] B. K. Bose, Modern Power Electronics and AC Drives, Prentice Hall (2001).

[25] P. C. Sen, Principles of Electric Machines and Power Electronics, John Wiley & Sons (1997).

[26] W. I. Rowen, Simplified Mathematical representations of heavy-duty gas turbines, ASME Journal of Engineering for Gas Turbines and Power, vol. 105 (1983).

List of Figures

List of Tables